ERRATUM

Title of ETD:

Searches for supersymmetry in the vector boson fusion topology with the ATLAS detector

Name of Author:

Aukerman, Andrew

Description of Correction(s):

I had to adjust some of the plot labels to be in agreement with the policies set forth by the larger experimental group before uploading to their repository, and would like the Pitt version to match. (Figure 32, page 75)

DAH 05/08/2020

Graduating School Approval Date Initialed

JJM 05/14/2020

Office of the Provost Approval Date Initialed

University of Pittsburgh

Searches for Supersymmetry in the Vector Boson Fusion Topology with the ATLAS Detector

by

Andrew Todd Aukerman

B.S. in Physics, B.A. in The History and Philosophy of Science

Submitted to the Graduate Faculty of

the Department of Physics in partial fulfillment

of the requirements for the degree of

Bachelor's of Philosophy

University of Pittsburgh

2020

UNIVERSITY OF PITTSBURGH

DIETRICH SCHOOL OF ARTS AND SCIENCES

This thesis was presented

by

Andrew Todd Aukerman

It was defended on

April 11 2019

and approved by

Tae Min Hong, University of Pittsburgh, Department of Physics

Michael Hance, University of California Santa Cruz, Department of Physics

Arthur Kosowsky, University of Pittsburgh, Department of Physics

Ayres Freitas, University of Pittsburgh, Department of Physics

Thesis Advisor: Tae Min Hong, University of Pittsburgh, Department of Physics

Searches for Supersymmetry in the Vector Boson Fusion Topology with the ATLAS Detector

Andrew Todd Aukerman, B.Phil

University of Pittsburgh, 2020

The Standard Model of particle physics attempts to describe the most fundamental aspects of our world. It has generated a vast number of successful predictions and offers immense explanatory power as to why and how the fundamental interactions observed in nature proceed the way they do. At the same time, there exist deep mysteries about our world and inconsistencies within the Standard Model itself that cannot be ignored. Supersymmetry is an extension to the Standard Model proposed to resolve some of these problems. A search for supersymmetric particles called *electroweakinos* within the vector boson fusion topology is presented using the full Run-2 dataset collected by the ATLAS experiment at CERN. Generation of the signal model hypothesis, modeling and estimation of backgrounds, development of powerful discriminating variables, and statistical interpretation of the results are detailed. No excess above the Standard Model prediction is found. Model independent limits on generic new physics scenarios are performed, with the most stringent limit having a visible cross-section of 0.017 fb. Model dependent limits placed on electroweakino production exclude neutralino masses below 60 GeV. This constitutes the first signature based search of its kind at ATLAS and lays the groundwork for future work, which may include searches for light scalar states, which solve the strong-CP problem and bulk gravitons, which incorporate gravity into the Standard Model.

Table of Contents

List of Tables

List of Figures

Preface

There are a great number of people who have helped me on this rather insane undergraduate journey. First and foremost, my advisor, Dr. Tae Min Hong, who had seen a spark in my eye my Freshmen year. Dr. Hong had provided me with wonderful opportunities to grow as a person and as a scientist. His view and love for physics and the kind of work, good work, that one can do shines clearly, and this has greatly inspired me throughout the years. Dr. Ben Carlson, our post-doc at Pitt, spent many hours walking through concepts with me. His excitement to see what kind of crazy (or dumb) ideas I had dreamed up next always kept me thinking and always curious.

I have sincere gratitude to extend to my fellow analysis team: Mike Hance, for essentially helping get this project off the ground and for his vision for what could become. He encouraged me in the very early days of this analysis. Joana Machado Miguens, for her support and careful scrutiny of many of the results and methods described in this document. Stefano Zambito, for his excitement and help with interpretation ideas. Jeff Shahinian who had developed the Fake Factor method described and through our chats helped me understand more how it works. Julia Gonski, who has moved literal mountains, producing the common n-tuples which serve this analysis goal.

And to my friends – you've shown me what it means to be a strong person, and someone who is dedicated to a scientific pursuit. You've shown me the beauty of this world, which has only inspired me to be even more curious about our strange universe. Close to my heart are memories of becoming a scientist along side you guys. And last but not least, to my family. You've supported me since day one, and let me run around making up all sorts of science experiments as a young kid. Now that the science experiments are a bit more involved (though likely equally mad), I want to thank you for always encouraging me, for picking me up when I fell, and loving me for who I am.

1.0 Introduction - Theoretical Motivations

The history of particle physics demonstrates a steady increase in the ability to describe the matter that makes up our known world. With each discovery, the substructure of interactions and fundamental units of matter was resolved with greater clarity and understanding. The last of such major revolutions was the discovery of the Higgs boson by the ATLAS [4] and CMS [5] experiments in 2012. This completed the Standard Model of Particle Physics, which describes all known fundamental particles (point-like entities with no further substructure) and their interactions. This model is extremely successful (providing both predictive and explanatory heuristics) in terms of experimental outcomes; though, despite this vast empirical success, there still exist deep mysteries about our world. The Standard Model itself, even, presents open questions that cannot be ignored.

It is these deep mysteries and questions that propel the vast and broad scientific programs seen today, one of which is understanding the particle nature of dark matter. The empirical evidence for a type of non-luminous, non-interacting type of matter is now well established. One of the earliest evidence for this was the measurement of galactic rotation curves, where the centripetal acceleration of massive, celestial objects (such as galaxies) didn't match the gravitational acceleration according to only visible matter within the object. The particles of the Standard-Model only account for about 5% of energy confirmed with great experimental accuracy to exist in the universe. There is a known relic abundance of this matter necessary to account for these (and future, more accurate) observations, which is usually considered to be cold or slow moving, being $\Omega h^2 = \pm 0.11860.0020$

Experiments to observe this matter exhibit a rich array of experimental modaility. Searches for dark matter particles take place in Earth's orbit, for example DAMPE experiment, whose purpose is to detect electrons and photons in order to identify possible dark matter signatures [6]. Searches for dark matter also take place deep underground, most notably the XENON1T Dark Matter Experiment, located 3.6 km under the Earth's surface, whose working principal is to detect ordinary matter recoiling off a 2 tonnes of Xenon atoms [7]. The IceCube Neutrino Observatory, located at the South Pole, houses thousands of

sensors below artic ice in order to detect neutrino initiated events with high precision and sensitivity.

These experiments search for Beyond the Standard Model (BSM) particles existing in nature. Another methodology is to create conditions in which these new particles could be created. The Large Hadron Collider (LHC), located at CERN in Geneva Switzerland, accomplishes this by colliding protons at large energies. These collision events serve a variety experimental apparatuses, which detect the subsequent decay products from these collisions. So far, this intense scientific program has revealed no conclusive evidence for additional particles, interactions, or structure beyond that described by the Standard Model.

1.1 The Standard Model

The Standard Model (SM) is a theory of fields with spin 0, $\frac{1}{2}$, and 1. The Lagrangian which ultimately describes the equations of motions from these field interactions written in its gauge invariant form contains four major components:

$$\mathcal{L}_{SM} = -\frac{1}{4}F_{\mu\nu}F^{\mu\nu} \tag{1.1a}$$

$$+ i\bar{\psi}\not{D}\psi + \text{h.c.} \tag{1.1b}$$

$$+ \bar{\psi}_i y_{ij}\psi_j\phi + \text{h.c.} \tag{1.1c}$$

$$+ |D_\mu\phi|^2 - V(\phi) \tag{1.1d}$$

The first term, (1.1), represents the kinetic energy term of the gauge field, where $F_{\mu\nu}$ represents the field strength tensor and the indices μ and ν run over the 4 space time dimensions t, x, y, z. The second term describes the kinetics of fermion interactions, where ψ represents the fermionic fields, and $\not{D}$ is the covarient derivative chosen to preserve the gauge symmetry. The third term contains the fermion yukawa terms. The fourth term contains the kinetic and potential terms corresponding to the Higgs field.

The fermionic fields have an intrinsic chirality and do not exist in the minimal form; instead, they contain three families or generations. The left-handed quarks of the Standard

Model come in doublets of weak isospin and triplets of color charge. Each quark is degenerate with respect to charge, but not mass degenerate with respect to weak isospin, giving the up and down type quarks of different masses. To preserve hypercharge, each quark must carry fractional charge in units of $\pm\frac{1}{3}$ and $\pm\frac{2}{3}$. The left-handed leptons come in doublets of weak isospin and singlets of color charge. The right-handed leptons come in singlets of weak isospin.

The spin 1 fields describe the interaction terms in the Standard Model. There are three gauge fields, with 8, 3, and 1 generator(s) each:

$$G_\mu^A,\ A = (1, 2, ...8) \text{ Gluons} \tag{1.2a}$$

$$W_\mu^I,\ I = (1, 2, 3) \text{ Weak bosons from the W field} \tag{1.2b}$$

$$B_\mu^Y,\ Y = (1) \text{ Photon from B field} \tag{1.2c}$$

$$\tag{1.2d}$$

These gauge-fields follow a gauge symmetry. This predicts forces which follow three types of charges: called the color charge (C), weak-isospin (L), and the hyper-charge (Y).

$$\mathcal{G} = SU(3)_C \otimes SU(2)_L \otimes SU(1)_Y \tag{1.3}$$

The standard model and all of the particles, fields, forces and key properties of these particles are summarized in Figure 1.

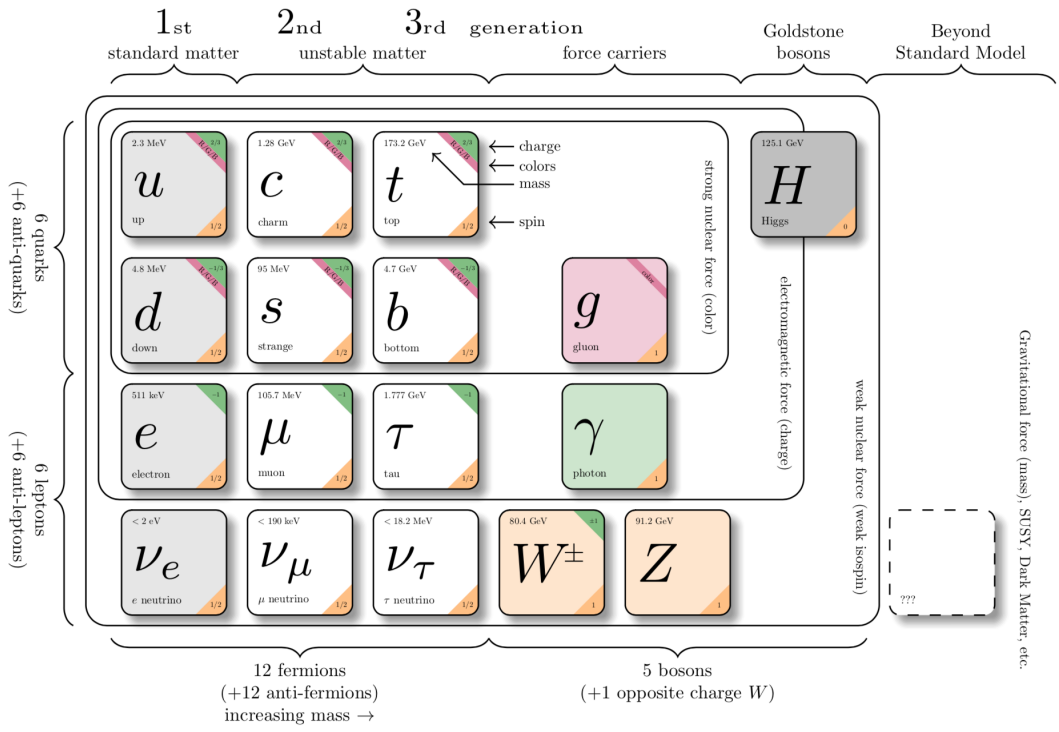

Figure 1: The particles of the Standard Model.

1.2 Gauge Theory

The SM includes spin 1 gauge fields with describe fundamental interactions and forces. The construction of these fields follows local gauge invariance or, in other words, respect a local gauge symmetry. In the classical picture, nature has informed us that the "playing-out" of physical phenomena shouldn't depend on certain quantities, one being shifts in time. Another such quantity discovered is the gauge of the interaction, e.g. for two charged objects, which have some potential difference $V(x)$, making the change $V(x) \to V(x) + c$ (a global transformation, called 'gauging') should have no impact on the calculations. Indeed, in classical electromagnetism this is this the case.

The extension to a quantum-field theory introduces the notion of local gauge transformations. Noether's theorem provides intuition for why we would want gauge fields in the first place, stating that "every differentiable symmetry of the action of a physical system has a corresponding conservation law". There is a deep interplay between conserved quantities, the fields which interact with them, and the currents which source them. The simplest of such examples is to introduce a $U(1)$ phase transformation of $\psi \to e^{i\eta(x)}\psi$, gauging the phase of the field by a local (space-time) variable. The term $\langle\psi|\psi\rangle$ with a $U(1)$ symmetry remains invariant, for both a local and global phase transformation:

$$\langle\psi|\psi\rangle \to \quad \langle\psi'|\psi'\rangle \tag{1.4a}$$

$$\langle\psi'|\psi'\rangle = \langle e^{i\eta}\psi|e^{i\eta}\psi\rangle \tag{1.4b}$$

$$= \langle\psi|e^{-i\eta}e^{i\eta}|\psi\rangle \tag{1.4c}$$

$$= \langle\psi|\psi\rangle \tag{1.4d}$$

Considering a kinetic term of the form, $\bar{\psi}\partial_\mu\psi$ introduces a gauge variance, spoiling the symmetry. In local gauge transformations, the term η depends on space-time coordinates

$\mu = (t, x, y, z)$, and thus expansion following the product rule is required:

$$\bar{\psi}\partial_\mu\psi \to \bar{\psi}'\partial_\mu\psi' \tag{1.5a}$$

$$\bar{\psi}\partial_\mu\psi' = e^{-i\eta}\psi\partial_\mu e^{i\eta}\psi \tag{1.5b}$$

$$= e^{-i\eta}\psi\partial_\mu e^{i\eta}\psi \tag{1.5c}$$

$$= e^{-i\eta}\psi[e^{i\eta}\partial_\mu\psi + \psi\partial_\mu e^{i\eta}] \tag{1.5d}$$

$$= e^{-i\eta}\psi[e^{i\eta}\partial_\mu\psi + \psi\partial_\mu e^{i\eta}] \tag{1.5e}$$

$$= e^{-i\eta}\psi[e^{i\eta}\partial_\mu\psi + i\psi e^{i\eta}\partial_\mu\eta] \tag{1.5f}$$

$$= \psi\partial_\mu\psi + \underbrace{i\psi\psi\partial_\mu\eta}_{\text{Extra Term}} \tag{1.5g}$$

Instead, a different kinetic term is required that respects the $U(1)$ symmetry. One can make the ansatz that this new operator follows the form $D_\mu = \partial_\mu - ieA_\mu$ where A_μ is the corresponding gauge field in the theory and will transform simultaneously with the phase transformation as $A_\mu \to A_\mu + c_\mu$, where c_μ can include terms proportional to $\partial_\mu, \eta, A_\mu$. Following the same calculation as with this new derivative yields:

$$\bar{\psi}D_\mu\psi = \bar{\psi}\partial_\mu\psi - i\bar{\psi}eA_\mu\psi + \underbrace{i\bar{\psi}\psi\partial_\mu\eta - iec_\mu\bar{\psi}\psi}_{\text{Extra Terms}} \tag{1.6}$$

The choice of $c_\mu = \frac{1}{e}\partial_\mu\eta$ exactly cancels the extra terms, leaving the kinetic term under a gauge transformation invariant. Unfortunately, this means that the gauge fields themselves cannot acquire a non-zero mass; the only choice of m being attached to a term like $A_\mu A^\mu$ which leaves this term invariant is 0.

$$m^2 A_\mu A^\mu \to m^2 A'_\mu A^{\mu\prime} \to m^2 A_\mu A^\mu + m^2 A_\mu \frac{1}{e}\partial_\mu\eta(x) \tag{1.7}$$

At this point, asking why one would want or care about a local gauge symmetry becomes a relevant consideration. In our example, if the ψ's are charge sources (i.e., electrons or positrons), this theory predicts a massless gauge boson, with interaction terms which automatically preserve charge. By gauging the symmetry locally, and introducing the covariant derivative, we've essentially constructed the theory of Electromagnetism in one stroke. To this Lagrangian, one can add the field strength tensor to account for energy stored in the

fields (which is also gauge invariant) and have equations of motion for massive charged particles following the full theory of electrodynamics.

This formalism, despite its apparent elegance, cannot be extended the observed nature of the electroweak force. While the photon is indeed massless, the weak force, mediated by its respective bosons, has experimentally been proven to operate at short distance scales, implying a non-zero mass which has also been measured and confirmed. This also complicates the fermion sector which have been shown to also interact with the weak field. All left-handed fermions must now come in a doublet of weak iso-spin which respects the $SU(2)_L$ symmetry. The algebra is more complicated, yet follows a similar prescription: the generators of the symmetry are the 2-dimensional Pauli matrices, τ , and the local transformation is a 2-vector that can depend on space time-coordinates:

$$\psi_L = \begin{pmatrix} e \\ \nu \end{pmatrix} \rightarrow e^{i\omega(x)\cdot\tau}\psi_L \tag{1.8}$$

There is no such transformation for right-handed fermions which come in singlets. Any mass term would mix both right and left handed states, and since the right handed states do not transform with the $SU(2)_L$ group while the left handed states do, such terms are not locally gauge invariant. Such a theory requires all particles be massless, so either the concept of gauge invariance be thrown out (and abandon the means to explain charged interactions with symmetry arguments), or a way to generate mass terms while respecting these symmetries must be attempted. Peter Higgs [8], Robert Brout, François Englert, Gerald Guralnik, C. Richard Hagen, and Tom Kibble, presented gauge theories to accomplish this task through a process known as Spontaneous Symmetry Breaking (SSB).

1.3 The Higgs Mechanism

In short, the Higgs Mechanism gives mass to the observed massive bosons, the $W^{\pm}$, and Z^0 and through its indirect interactions with the left handed fermions, generates mass for all fermions too (except the neutrinos... another motivation for BSM physics). Some mechanism

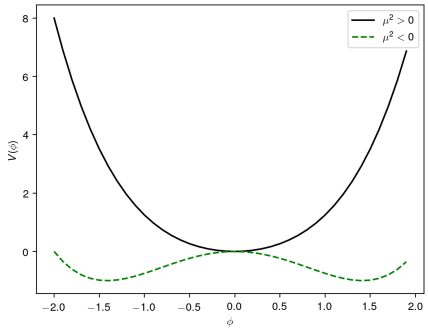

Figure 2: A non-zero minimum can appear in some cases of the Higgs scalar potential.

is required to produce three massive gauge bosons, one massless gauge boson that still looks like the photon, and mass terms for every fermion. This can be accomplished by introducing a $SU(2)$ scalar field (The Higgs field) represented by ϕ that respects both a $SU(2)_L$ and $U(1)_{EM}$ gauge symmetry. This introduces the $\mathbf{W}$ and B fields with dimensions 3 and 1 (setting a scaffold for the electroweak and EM force respectively). The minimal renormalizable, bounded potential term for this field is:

$$V(\phi) = \frac{1}{2}\mu^2\phi^2 + \frac{1}{4}\lambda\phi^4, \ \lambda > 0 \tag{1.9}$$

The minima of this potential, $\langle\phi\rangle$, is shown in Figure 2. If the Higgs field acquires a non-zero expectation value $\langle\phi\rangle \neq 0$, the gauge bosons will acquires mass directly from lost degrees of freedom, while the fermions (with the exception of the neutrino) acquire mass for being an admixture of left and right chiral states. To illustrate the intuition behind this, I'll follow the minimum example in which a scalar field breaks into a massive and massless boson, that of a $U(1) \times U(1)$ field.

A Lagrangian that describe a purely bosonic field that with a U(1) local gauge symmetry applied to both a A_μ and B_μ field is:

$$\mathcal{L}_{U(1)\times U(1)} = -\frac{1}{4}F_{\mu\nu}F^{\mu\nu} \tag{1.10a}$$

$$+ |(\partial_\mu + igQA_\mu + igQB_\mu)\phi|^2 \tag{1.10b}$$

$$- V(\phi) \tag{1.10c}$$

The field strength term will have no effect on the phenomenology of this theory since it only sees the vector field terms (not the scalar field). After reparametrizing the scalar field as $\psi' = v + \eta + i\chi$, with v being the new vacuum expectation value which minimizes the potential, new terms appear. Expanding about the new minimum, this becomes (ignoring constants and terms with χ for reasons that will become clear later):

$$V(\eta) \propto v^3\eta + v^2\eta^2 + v\eta^3 + \eta^4 \tag{1.11}$$

Each term describes import physics of this potential, which all correspond to the new field η (which in the full SM corresponds to the remnant Higgs boson). The first term describes a spontaneous interaction, which allows Higgs bosons to terminate arbitrarily from vacuum fluctuations. The second term is a mass term, now non-zero due to the *vev*. The third and fourth terms describe a cubic and quartic interaction of a Higgs boson with itself, which gives rise to di-Higgs and Higgs self-energy processes respectively.

Having ignored the χ term has allowed for an easy 'writting-off' of these terms, but must be sufficiently motivated. Analysis of the kinematic terms included in the covarient derivative tell us why. The kinematic terms, un-expanded, are

$$[(\partial_\mu + igQA_\mu + ig'Q'B_\mu)(\eta + v + i\chi)][(\partial^\mu + igQA^\mu + ig'Q'B^\mu)(\eta + v + i\chi)]^\dagger \tag{1.12}$$

In general, there are 81 total terms generated by this interaction; so we'll limit ourselves to a few that truly concern us most, namely those which involve interactions of order A_μ and B_μ, but also some of order η and $\partial_\mu\chi$. First, there are now non-zero values to the squared terms for the A_μ and B_μ field terms (a), kinematic terms for the new scalar fields (b), and strange

mixing terms between the scalar and gauge fields (c), and mixed mass terms between the two gauge field (d).

$$(gQv)^2 A_\mu A^\mu + (g'Q'v)^2 B_\mu B^\mu \tag{1.13a}$$

$$|\partial_\mu \eta|^2 + |\partial_\mu \chi|^2 + 2|\partial_\mu \eta||\partial_\mu \chi| \tag{1.13b}$$

$$\partial_\mu \eta i g Q v A_\mu + \partial_\mu \chi i g Q v A_\mu + \partial_\mu \eta i g Q v B_\mu + \partial_\mu \chi i g Q v B_\mu \tag{1.13c}$$

$$(gQv)(g'Q'v) B_\mu A^\mu + (gQv)(g'Q'v) A_\mu B^\mu \tag{1.13d}$$

At this point, some booking keeping is necessary. We started with two scalar fields, and two massless gauge fields which have two polarizations each, so a total of 6 total degrees of freedom. We now have two scalar fields, and two massive gauge bosons with three polarizations (since the transverse polarization opens up), for a total of 8 degrees of freedom. One of these extra degree's of freedom is not genuine; it can be eliminated by the choice of gauge. To see this, one can pull the $\partial_\mu \chi$ and B_μ terms from (1.13a-d), and write these terms a local gauge transformation of B_μ with a scalar field χ. This means that one of the degrees of freedom actually corresponds to a preserved U(1) symmetry that remains unbroken, and thus the apparently massive boson B_μ is indeed massless in the unitary gauge, eliminating one of the polarizations of the Higgs vacuum expansion. This also eliminates the mixed kinetic term in (1.13b).

Another way to see this is to collect all the squared gauge field terms into a mass matrix $\mathbf{M}$:

$$\mathcal{L}_{\text{mass}} = \begin{pmatrix} A^\mu & B^\mu \end{pmatrix} \begin{pmatrix} m^2 & mm' \\ mm' & m'^2 \end{pmatrix} \begin{pmatrix} A_\mu \\ B_\mu \end{pmatrix} \tag{1.14}$$

The eigenvalues for the mass matrix $\mathbf{M}$ are $\lambda = 0, m^2 + m'^2$, so there is always a way to re-write the field terms (i.e. transform into an appropriate basis) such that one field is always massless while the other has a mass of $m^2 + m'^2$. Thus, in this example, a $U(1) \times U(1)$ gauge symmetry broke into a rennet, massless boson and a massive boson. If we had followed the more complex example of a $SU(2) \times U(1)$ symmetry, we'd have 3 massive boson and 1 massless boson. These are exactly the W, Z, γ of the standard model, with the free transverse component of the Higgs field being the Higgs boson.

1.4 Motivation for Beyond the Standard Model Particles

There exists an issue with including scalar degrees of freedom in the current Standard Model of particle physics. Being a renormalizable theory, all higher order perturbations must return finite values. Virtual corrections have no upper-bound on the momentum of the interaction, and thus must also remain finite in the high-energy behavior. Regularization can be performed to return these values for certain well controlled interactions. There is no defined scale for which the Standard Model should break-down, so to speak. One has to speak of this cut-off in somewhat arbitrary terms; we will use the plank mass of $M_p \approx 10^{19}$ GeV.

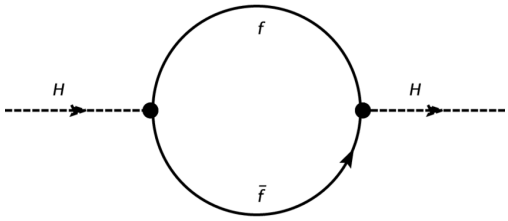

Figure 3: A radiative correction to the Higgs mass

A propagating Higgs boson at first order receives no contributions to its mass other than a bare mass term generated by the spontaneously broken $SU(2)$ symmetry. Higher-order terms contribute to its observed mass (self energy diagrams, loosely like observed mass of the proton from the energy stored in gluon field interactions). When one considers an interaction of the Higgs field with any other particle to which it couples (including itself), i.e. higher order quantum corrections, the pathology of a light Higgs boson within the Standard Model becomes more apparent. This reveals that the entire hierarchy of having $M_h \ll M_p = 10^{19}$ GeV is unstable. In the case of a Higgs pair-producing two fermions, such as that in Figure 3, which then re-annihilates (a next-to-leading process of Higgs propagation, with each increasing order introducing a factor of λ_f^2). These higher-order diagrams contribute to the observed Higgs boson mass of 125.2 GeV.

The leading-order correction to the mass can be written as an integral representing the

diagram in (diagram loop), ignoring indices of the fermion spinors:

$$\delta m_h^2 = \lambda_f^2 \cdot \int \frac{1}{p+k-m_f} \frac{1}{p-m_f} d^4p \tag{1.15}$$

The integral is evaluated over all possible phase-space in the energy-momentum basis. During evaluation of this integral, when $p \gg k$, an effective self-energy vertex can be used and is described by:

$$\delta m_h^2 = \lambda_f^2 \cdot \int \frac{1}{p^2 - m_f^2} d^4p \tag{1.16}$$

To see the high energy behavior of this integral, isolating the degree of freedom corresponding to energy, such that $p = E$, and $d^4p = \frac{\partial}{\partial E}\frac{\partial^3}{\partial p} E(1, v) = E^3 dE d^3v$

$$\delta m_h^2 = \lambda_f^2 \cdot \int \frac{E^3}{E^2 - m_f^2} dE \int d^3v = \int E dE = E^2 \tag{1.17}$$

Evaluating the integral up to some cutoff energy, Λ_{UV}, the correction to the Higgs mass is

$$\delta m_h^2 = \lambda_f^2 \Lambda_{UV}^2 \tag{1.18}$$

If Λ_{UV} is small, perhaps a order of magnitude larger than the Higgs mass, this correction is not large; it'd be of the same order or lower (depending on the coupling) to the overall bare mass term generated by the vacuum. Taking a step-back, the physical interpretation of such a small cut-off indicates that the physics described by the Standard Model are only valid up to that certain energy. This would be experimentally problematic, as the validity of the Standard Model has been tested at energy scales of 1 TeV at the LHC. It is also theoretically unfavorable, as justification would be needed for why low-energy phenomena is described by a different model than interactions just barely above the scale at which we currently understand.

Choosing a high cut-off resolves the experimental and interpretative difficulties, yet the theoretical consequences are severe. Assuming the physics of the Standard Model are valid up to the Planck-mass, $\Lambda_{UV}^2 = 10^{40}$, at which the Compton wavelength corresponds to the lower-bound on a sensible quantum length (the Planck length), the correction to the Higg mass is equally massive. In order to temper these corrections cancellations between terms necessitates an extreme fine-tuning. The mass term is order $(100\text{ GeV})^2$, while the

corrections are order $(10^{20}\ \text{GeV})^2$: a remarkable degree of cancellation must occur to recover the small mass of the Higgs from terms much, much larger than this.

There is nothing that prevents this fine-tuning, but it suggest extreme instability of the hierarchy of the Standard-Model. Not only is the Higgs mass sensitive to the quadratic divergence at high energies, the entire mass spectra of the Standard Model particles, which inherit mass through the Higgs are equally impacted. To write the full theory with this effect in mind, a precise determination of parameters to which the Higgs mass is sensitive is required across 40 orders of magnitude. This is a departure from all other physical theories to date, where the scale of interactions can be described by parameters of approximately equal scale; so-called "Natural Theories" for having this property.

One *other* interpretation of a low cut-off is that some *new physics* enters at or around the electroweak scale, which in turn alter corrections to the Higgs mass. Ideally, this would not approximately, but exactly cancel the quadratic divergences in the UV limit. The kinematic term $K(\Lambda_{UV})$, will be equivalent in the UV limit, and the model dependent parameters must be *exactly* equal. Without a mechanism to guarantee this equality, such cancellation would be equally fine-tuned; however, if one introduces a new symmetry of nature which dynamically generates couplings exactly equal to the Standard Model couplings, there could be such an exact cancellation of these divergent terms. This new symmetry, if a space-time symmetry corresponding to spin, will introduce a partner for each SM particle – this type of symmetry is called *supersymmetry*, and is one such way to resolve the heirachy and fine-tuning problems of the Standard Model, while also providing a suitable dark matter candidate.

Supersymmetry relates particles with half integer spin (fermions) and integer spin (bosons). Symmetries are useful in that, under symmetry transformations, conserved quantities appear. For example, physical phenomena are invariant under global charge transformation; if someone managed to swap every negative and positive charge, not only would physical phenomena proceed the same, but there would be no way to tell such a change occurred. It is such a invariance the guarantees the quantization of certain parameters. By relating fermions and boson by a new symmetry, the exact cancellation of coupling required constants is guaranteed. If built correctly, such a particle spectrum contributes exactly equal

and opposite contributions at the UV limit to the SM particles, essentially protecting the Higgs from high energy behaviors.

1.5 Supersymmetry in a Nutshell

The fundamental principal of SUSY is to introduce a new operator, Q, which exhibits the following property:

$$|\phi\rangle = Q\,|\psi\rangle \tag{1.19}$$

Here ϕ and ψ are fields differing by half integer spin, i.e. that Q relates a bosonic and fermionic fields. This operator would also need to respect all existing symmetries of the Standard Model, so any SU multiplet would need to transform into a multiplet that respects the same SU gauge symmetry. Considering, for example, the $SU(2)_L$ doublet for electrons, some operator would need to relate these fermions to a spin-0 doublet which also respects the $SU(2)_L$ symmetry. In the Standard Model, such a doublet already exists– the higgs doublet, so one *could* attempt to write a new symmetry like:

$$\begin{pmatrix} e \\ \nu_e \end{pmatrix} = Q \begin{pmatrix} \phi^0 \\ \phi^+ \end{pmatrix} \tag{1.20}$$

However, a symmetry generator with this property would break lepton flavor conservation (and probably cause many other awful problems), by increasing or decreasing (by $Q^\dagger$) electron flavor. Instead, one can introduce *new* fields which also respect the SU(2) symmetry and *also* have the same flavor. This introduces the super-partners to the electron and neutrino, called the selectron and sneutrino, which is extended to the 2^{nd} and 3^{rd} generations.

$$\begin{pmatrix} e \\ \nu_e \end{pmatrix} = Q \begin{pmatrix} \tilde{e} \\ \tilde{\nu_e} \end{pmatrix} \tag{1.21}$$

The quarks respect the $SU(3)$ color symmetry, and no other Standard Model multiplet also comes in SU(3) triplets (they are all color singlets and naively respect color symmetry). One must introduce a new scalar $SU(3)$ group which carries the color charge. Thus, each quark

of the SM has a partner *squark*. These new scalar fields resolve any quadratic divergences introduced by fermion interactions with the spin-0 boson in the Standard Model.

The gauge bosons of the Standard Model also contribute quadratic divergences, and a similar prescription can be followed for the spin 1, pre-SSB gauge fields of the SM. The massless W and B fields (which acquire mass terms following SSB) have spin $\frac{1}{2}$ partners which respect the same gauge symmetry: a color octet of gluon partners (gluinos), a triplet (winos) and singlet (bino). Last but not least, the SU(2) Higgs doublet needs fermionic partners to cancel its contributions. The MSSM requires that the two Higgs doublets of the SM not be written as charge conjugates of each other (that instead, the up and down type quarks receive mass from two distinct doublets). Thus, two 'higgsino' doublets are introduced. This completes the particle and field composition of the MSSM.

1.6 Soft Supersymmetry breaking

The fundamental idea of *soft* supersymmetry breaking [9] is that we would like to break supersymmetry without reintroducing the quadratic divergences. We write the Lagrangian in a form:

$$\mathcal{L}_{\text{MSSM}} = \mathcal{L}_{\text{SUSY}} + \mathcal{L}_{\text{soft}} \tag{1.22}$$

In this sense, the symmetry breaking is "soft", since we have separated out the completely symmetric terms from terms which break the symmetry in the low-energy limit, but maintain quadratic safety in the UV limit. Through a number of careful proofs (done by others [9]), the terms explicitly allowed to break the supersymmetric terms are:

- Mass terms for the scalar components of the chiral supermultiplets (Squarks)
- Mass terms for the Weyl spinor components of the gauge supermultiplets
- Trilinear couplings of scalar components of chiral supermultiplets

In particular, using the field content described above for the MSSM, the softly-broken portion of the MSSM Lagrangian can be written

$$\mathcal{L}_{\text{soft}} = M_3\tilde{g}\tilde{g} + M_2\tilde{W}\tilde{W} + M_1\tilde{B}\tilde{B} + \text{h.o.t} \tag{1.23}$$

$$- \tilde{u}a_u\tilde{Q}H_u - \tilde{d}a_d\tilde{Q}H_d - \tilde{e}a_e\tilde{L}H_d + \text{h.o.t} \tag{1.24}$$

$$- \tilde{Q}^\dagger m_Q^2\tilde{Q} - \tilde{L}^\dagger m_L^2\tilde{L} - \tilde{u}m_u^2\tilde{u}^\dagger - \tilde{d}m_d^2\tilde{d}^\dagger - \tilde{e}m_e^2\tilde{e}^\dagger \tag{1.25}$$

$$- \mu(H_u + H_d)^2 + \text{h.o.t}). \tag{1.26}$$

The introduced notation includes M_3, M_2, M_1 as the gluino, wino, and bino masses, a_u, a_d, a_e as complex 3×3 matrices in family space, $m_Q^2, m_u^2, m_d^2, m_L^2, m_e^2$ as hermitian 3×3 matrices in family space, $m_{H_u}^2, m_{H_u}^2, b$ as the SUSY-breaking contributions to the Higgs potential. The second and third rows contain flavor and parity violating terms, which are highly constrained by previous experiments. We thus only consider flavor-blind, CP-conserving interactions within the MSSM. The gaugino, higgsino, and scalar masses are not, in general, constrained – and we in particular focus on the electroweak sector formed by the wino, bino, and higgsino terms with mix to form *electroweakinos*. The electroweakino portion of the Lagrangian can be written, with ψ in the gaugino basis $= (\tilde{B}, \tilde{W}, \tilde{H}_u, \tilde{H}_d)$, as [9]:

$$\mathcal{L}_{Electroweakino} = -\frac{1}{2}\bar{\psi}\mathbf{M}_N\psi + \text{h.o.t} \tag{1.27}$$

The matrix determines the mixing of the neutral components, described by:

$$\mathbf{M}_N = \begin{pmatrix} M_1 & 0 & \frac{-g'v_d}{\sqrt{2}} & \frac{g'v_u}{\sqrt{2}} \\ 0 & M_2 & \frac{g'v_d}{\sqrt{2}} & \frac{-g'v_u}{\sqrt{2}} \\ \frac{-g'v_d}{\sqrt{2}} & \frac{g'v_u}{\sqrt{2}} & 0 & -\mu \\ \frac{g'v_d}{\sqrt{2}} & \frac{-g'v_u}{\sqrt{2}} & -\mu & 0 \end{pmatrix} \tag{1.28}$$

It's easy to see that without EWSB, where both the up- and down-like Higgs vev's are zero ($v_u = v_d = 0$), Eq. (1.28) would already be in a reduced row echelon form, and one could diagonalize the gaugino and higgsino sub-matrices separately, and instead write the mass terms like:

$$\mathcal{L}_{Electroweakino} = -\frac{1}{2}\begin{pmatrix}\tilde{B}\\ \tilde{W}\end{pmatrix}^T \mathbf{M}_N^{1,2}\begin{pmatrix}\tilde{B}\\ \tilde{W}\end{pmatrix} - \frac{1}{2}\begin{pmatrix}\tilde{H}_u\\ \tilde{H}_d\end{pmatrix}^T \mathbf{M}_N^{3,4}\begin{pmatrix}\tilde{H}_u\\ \tilde{H}_d\end{pmatrix} + \text{h.o.t.} \tag{1.29}$$

Diagonalization of the mass matrix gives the four neutralino mass eigenstates $\tilde{\chi}^0_{1,2,3,4}$, which can be transformed from the mass matrix by a mixing matrix. For example, in the fully decoupled form 1.29, the mixing matrix for the bino and wino is the identity matrix (indicating pure gaugino states), and the higgsino mixing matrix being the 2-dimensional rotation matrix with $\theta = 45$ (indicating a pure higgsino state and exact ad-mixture of the up and down higgsino fields). The neutralinos, especially the lightest neutralino (LSP) and next-to-lightest neutralino (NLSP), are important ingredients in SUSY phenomenology. The same process can be done for charged portions of the higgsino doublets along with the charged winos ($\tilde{H}_u^+, \tilde{H}_d^+, \tilde{W}^+, \tilde{W}^-$). This leads to the *charginos*, again in order of increasing mass, $\tilde{\chi}^\pm_{1,2}$.

With realistic parameters, two special cases can occur on which this thesis is predicated: either the higgsino mass parameter is much larger than the gaugino parameters, $\mu \gg M_1,\ M_2$ (The wino-bino case) or the higgsino mass parameter is much smaller than the gaugino parameters $\mu \ll M_1,\ M_2$ (higgsino case) the mass matrix takes an approximate reduced row form with decoupled gauginos and higgsinos, each providing small order corrections (and relative mixing) to each other. Formally, the eigenvalues are approximately $\lambda_1 \approx M_1$, $\lambda_2 \approx M_2$, $\lambda_3 \approx \mu$, $\lambda_4 \approx \mu$. If $\mu \gg M_1,\ M_2$, the mass difference between the lightest neutralinos is then approximately $\Delta M = M_1 - M_2$, with contributions of order $\frac{M_W(M_1+M_2)}{\mu^4}$. If $\mu \ll M_1, M_2$, the mass splitting is of the order $\frac{M_W^2(M_1+M_2)}{M_1 M_2}$. Light higgsinos are not only well motivated by the quadratic divergence arguments, but relatively *compressed* higgsinos in particular, since the gaugino masses can be of TeV scales without spoiling naturalness. For illustration, gaugino masses of 1 and 2 TeV predict about 10-15 GeV mass splitting. The mass-spectra of the two models considered are shown in Figure 4 in comparison to others.

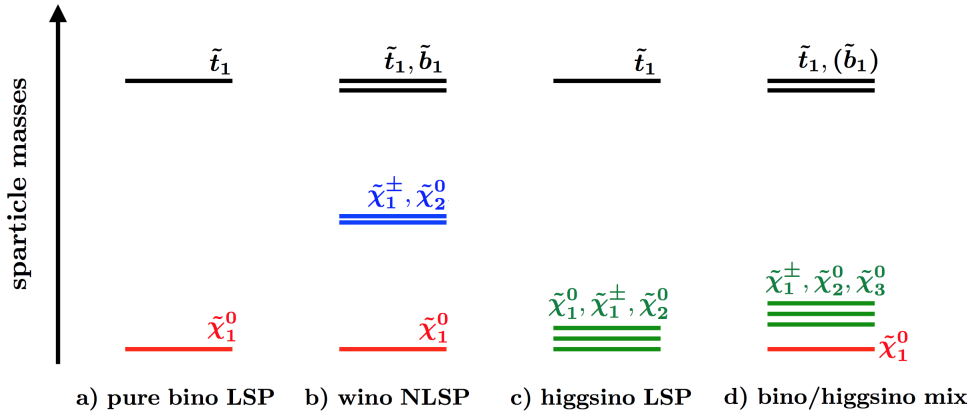

Figure 4: Sparticle mass spectrum of the 3$^{\text{rd}}$ generation squarks and electroweakinos.

2.0 The LHC and ATLAS Experiment

2.1 The LHC Accelerator Complex

The Large Hadron Collider [10] (LHC) at CERN[1] in Geneva, Switzerland is designed to deliver proton-proton (pp) collisions at an unprecedented centre-of-mass energy of $\sqrt{s} = 14$ TeV. The LHC is the last stage of a chain of accelerators which is depicted schematically in Fig. 5. The accelerator chain is as follows – initially, the protons are obtained by ionising

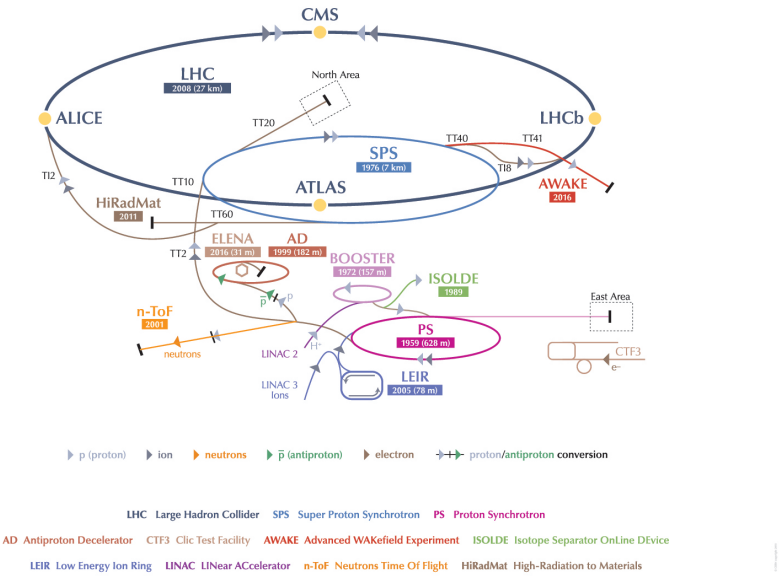

Figure 5: The CERN Accelerator Complex, from [1]

hydrogen atoms. In a linear accelerator (Linac 2) electric fields are applied to first accelerate the protons to an energy of 50 MeV. From here, the protons are injected into the Proton Synchrotron Booster (PSB), a circular accelerator which increases the energy up to 1.4 GeV. The next step is the Proton Synchrotron (PS), which accelerates the protons to energies of

[1] *Le Conseil Européen pour la Recherche Nucléaire*

25 GeV. In the PS, the protons are also separated spatially and accumulated into bunches. The last pre-acceleration step is the Super Proton Synchrotron (SPS) where the protons are accelerated to an energy of 450 GeV, before they are extracted into the LHC rings. Once inside the LHC, they are accelerated even further to their target energy of 13 TeV.

The primary goal of the LHC ring is deliver and maximize the number of collision events at the four interaction points located about the complex. The metric of interest is the instantaneous luminosity, at design capabilities being $\mathcal{L} = 10^{34} cm^{-2} s^{-1}$. This luminosity can be characterized by the following equation [11]:

$$\mathcal{L} = \frac{f_{Rev} N_{bx} N_p^{b1} N_p^{b2}}{\sigma_x \sigma_y} \cdot f(\beta^*_{x,y}, \phi) \tag{2.1}$$

Where $f_{Rev} N_{bx} N_p^{b1} N_p^{b2}$ are the frequency of rotation, number of circulating bunches, and number of protons in bunch 1 and in bunch 2, respectively. The factors $\sigma_x \sigma_y$ correspond to the beam spread at the interaction point (IP), and some geometrical function (with units cm^{-2}) relates the proton cross-section and IP optical geometry $\beta^*_{x,y}$ with some other physical factors. The LHC RF system runs on a 400 MHz clock and contains 35640 buckets, while about 2800 of these can be filled at most. In Run 2, the LHC ran primarily on a 2556 bunch scheme with 144 bunches per injection.

The optical beta function $\beta^*_{x,y}$ is determined by the accelerator magnet configuration, namely the quadrapole or triple magnets closest to the IP which focus or de-focus the proton beams into and out of the detector cavity. This is a metric of how "squeezed" the beam is, and this process is included as one of the final steps before stable beams are declared. Careful control over this quantity allows for leveling, in which a controlled increase in $\beta^*_{x,y}$ can off-set proton losses keeping the instantaneous luminosity constant for a few hours. This was achieved at the nominal Run 2 luminosity of $\mathcal{L} = 2^{34} \text{cm}^{-2} s^{-1}$, which corresponds to $2\text{pb}^{-1} s^{-1}$, writing the number of events per-second in terms of luminosity and cross-section:

$$N = \mathcal{L}\ \sigma_{pp \to X} \tag{2.2}$$

The integrated luminosity with respect to time provides a direct measure of the number of expected events for some process in a given data-set collected. Taking 1 fb^{-1} of data corresponds to producing a $\sigma = 1fb$ process once. The measure actually becomes 'smaller'

with more data (a inverse femtobarn is larger than an inverse picobarn), which can be interpreted as being able to probe smaller distance scales, in terms of event cross-section. The total delivered luminosity is shown in Figre 6, showing data collection by year and culminating throughout Run 2.

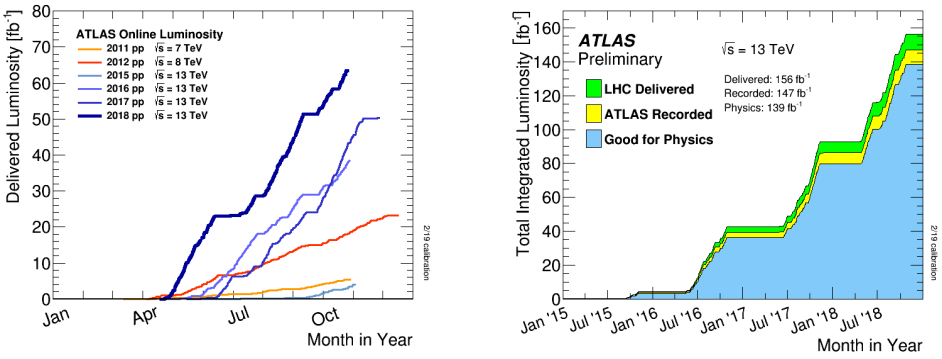

Figure 6: Delivered luminosity per year (left) and total LHC delivered, ATLAS recorded, and Good for Physics luminosity (right).

2.2 Atlas Detector

The ATLAS detector is one of the two general purpose particle detectors situated along the main LHC ring [12]. The ATLAS detector features forward-backward symmetric, cylindrical geometry providing coverage for nearly the full solid angle about the collision point, tracking charged particles close to the IP, measuring electromagentic and hardonicly interacting particle energy in a calorimeter middle layer and providing muon measurement and identification in the outermost layer. Collision data is collected using the ATLAS detector from 2015 to 2018. Only data collected during stable beams, with all detector subsystems within nominal operational parameters, and the trigger and data acquisition system functioning are considered [13].

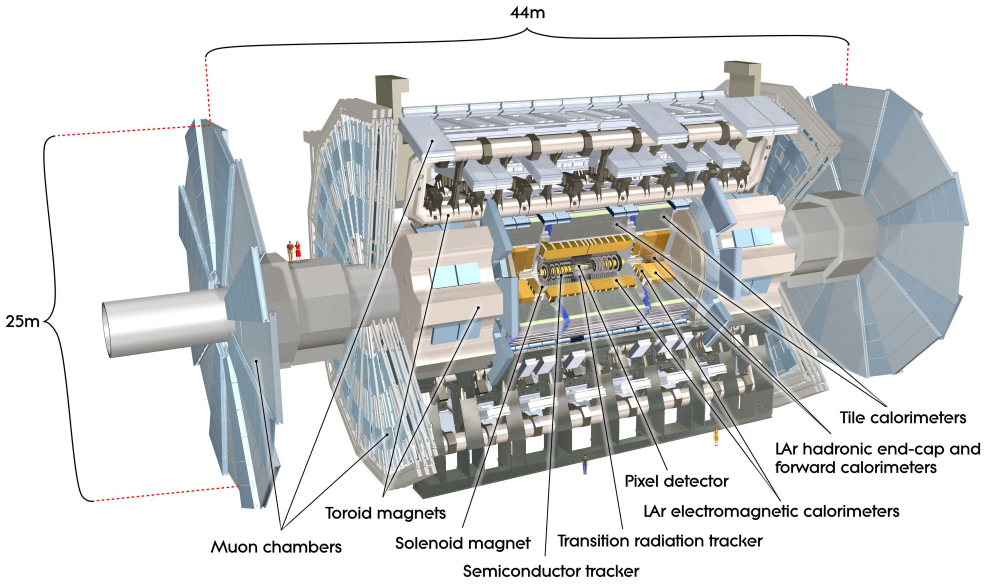

Figure 7: Cut-away view of the ATLAS detector, showing the overall design. From the inner-most to outer-most portions of the detector with respect to the collision point are the inner detector, calorimters, and muon spectrometer. The overall weight of the apparatus is approximately 7,000 tonnes.

High precision layers in the inner detector measure momenta of individual charged particles. The electromagnetic calorimeter uses a liquid argon active material and lead absorbing material to provide energy measurements for electrically charged particles. This layer is

surrounded by a Hadronic calorimeter to provide energy measurements for strongly interacting particles. A muon spectrometer provides momentum measurement and identification of muons. Protons are collided at the center of the detector at a center of mass energy of 13 TeV.

We take a cylindrical coordinate system of (r, z, ϕ), where z-axis is defined along beam pipe direction and the origin at the interaction point in the center of the detector, r-coordinate is orthogonal to that and ϕ is an azimuthal angle.[2]. The rapidity, y in terms of a particle's energy, E and momentum along the z-axis (the longitudinal momentum) is defined as:

$$y = \frac{1}{2}\ln\left(\frac{E + p_z}{E - p_z}\right) \tag{2.3}$$

In the massless, or equivalently the ultra-relativistic limit, $E^2 = p^2$:

$$y = \frac{1}{2}\ln\left(\frac{|p| + p_z}{|p| - p_z}\right) = \frac{1}{2}\ln\left(\frac{1 + {}^{p_z}/_{|p|}}{1 - {}^{p_z}/_{|p|}}\right) = \operatorname{arctanh}\frac{p_z}{|p|} \equiv \eta \tag{2.4}$$

One can rotate away one of the degrees of freedom with respect to the azimuthal angle and write $\mathbf{p} = (p_{\mathrm{T}}, p_z)$, such that $p_z = p\cos p_z$:

$$y = \frac{1}{2}\ln\left(\frac{1 + \cos\theta}{1 - \cos\theta}\right) = \frac{1}{2}\ln\left(\frac{\cos^2 {}^{\theta}/_{2}}{\sin^2 {}^{\theta}/_{2}}\right) = -\ln\tan\frac{\theta}{2} \equiv \eta \tag{2.5}$$

The definitions of pseudo-rapidity, η, in (2.5) and (2.4), demonstrates the useful property that under a Lorentz transformation parallel to the beam axis, the difference in pseudo-rapidity remains invariant. This allows for the construction of boost-invariant variables that relate the angular distributions between two particles observed in the detector. This is especially important as in hadron collisions where the initial longitudinal momenta of the center of mass frame is unknown.

[2] ATLAS uses a right-handed coordinate system: x-axis points to the ring center, y-axis points upward, and $\phi = 0$ is along x-axis so that the upper half of the detector is described by $0 < \phi < \pi$ and the lower half by $\pi < \phi < 2\pi$

2.3 The Inner Detector

The inner detector combines high granularity pattern recognition with precise momentum and energy resolution for effective charged track reconstruction and primary and secondary vertex measurements [12]. The full fiducial volume of the inner detectors is immersed in a 2 Tesla magnetic field, generated by a super conducing solenoidal coil. The full inner detector consists of three independent sub-dectetors, whose principle mode of operation vary. Figure 8 shows the technical layout of the inner detector for one quadrant, with the operational envelopes for the Pixel, semiconductor tracker (SCT), and transition radiation tracker (TRT) detectors overlaid.

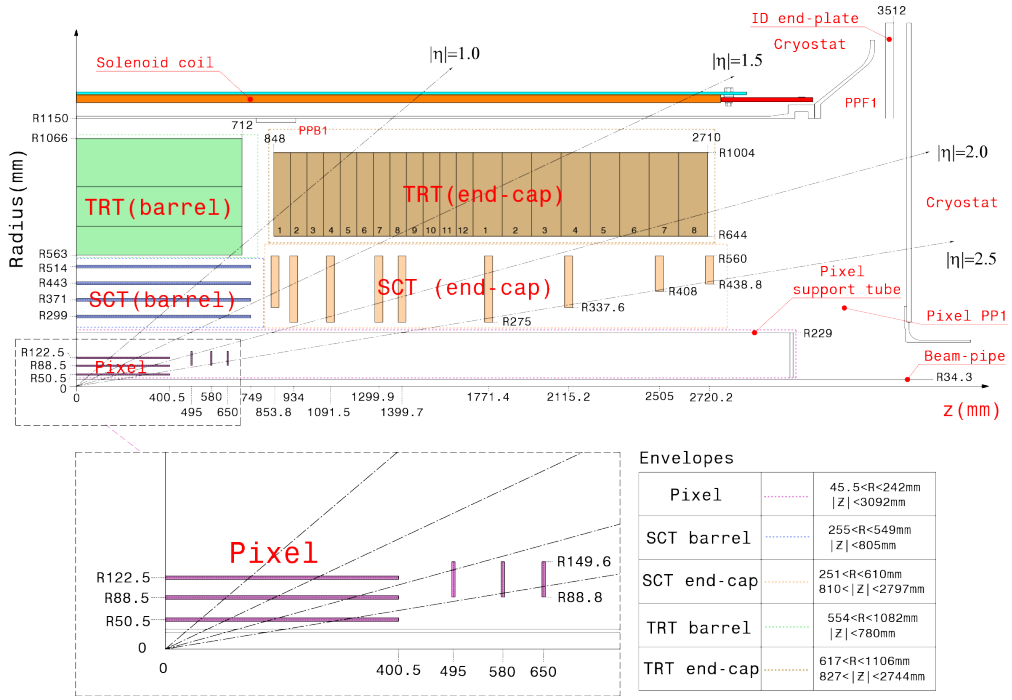

Figure 8: The $r - z$ plan view of a quarter section of the ATLAS inner detectors.

In the barrel region, a track will transverse three silicon-pixel layers with individual sensor elements, four layers of the SCT, and approximately 36 axial units contained in the TRT modules. At higher η, additional structures and different geometry is required to ensure pattern recognition of tracks. For example, a track with $\eta = 1.5$ will pass through three of the barrel pixel detector layers, however will not pass through any of the barrel SCT layers.

Instead, the end-cap SCT disks provide coverage in this forward region, and a track at this η range will pass through 3 to 4 the the double layers. At higher η, the a track will pass through only the first of the cylindrical layers in the pixel detector, then the last 2 disk layers in the end-cap. In total, this barrel and end-cap regions maintain a minimum of 6 total ID layers through which a particle in the full ID region, $|\eta| < 2.5$, will pass. The structure of the ID is summarized in Figure 9.

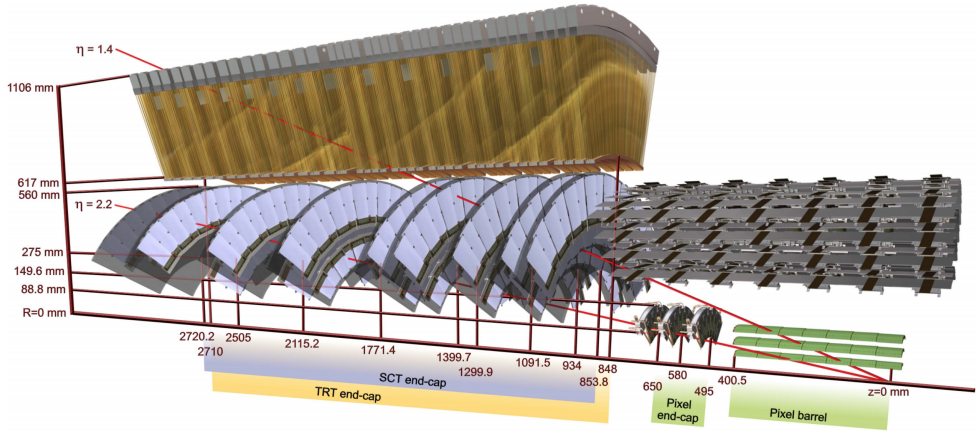

Figure 9: Drawing of the barrel and end-cap regions of the inner-detector.

The design of the SCT detector consisting of double layers with one rotated by a stereo angle of 40mrad is important for spatial reconstruction of a SCT hit. While the pixel detectors provide high granularity localization in 3D space, the precision provided by the SCT module is only known orthogonal to the module surface [14]. The TRT, in having an axial structure, only provides information in $r - \phi$ coordinates, but the large number of hits greatly improves p_{T} resolution. Additionally, the material makeup of the TRT provides greater discrimination between pions and electrons with the same momentum, which further reduces the electron mis-identification rate, as show in Figure 10.

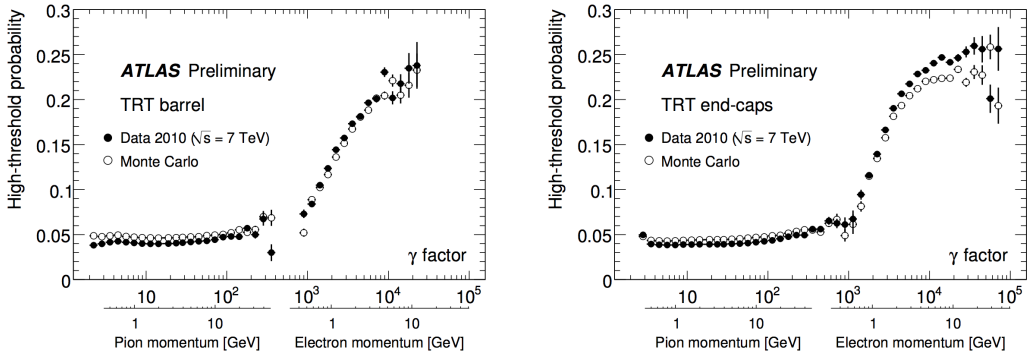

Figure 10: Threshold absorption probabilities for the TRT detector for charged pions and electrons of comparable momentum. This property of the TRT improves electron identification selectivity within the fidicual volume.

2.4 The Calorimeters

The ATLAS detector features a barrel, end-cap, and forward calorimeter to provide energy measurement, photon and electron identification, and jet measurements within nearly the full solid angle. The electromagnetic calorimeter uses a liquid argon active material and lead absorbing material to provide energy measurements for electrically charged particles. It features an accordion style structure, which optimizes the sampling and energy collection with an energy resolution of about $\frac{10\%}{\sqrt{E}}$. This layer is surrounded by a hadronic calorimeter to provide energy measurements for strongly interacting particles using iron and steel absorbing material and a scintillating active layer. It features a tile style structure, which optimizes hermicity along the ϕ direction.

The forward calorimeter (FCAL) provides geometric coverage from $3.1 < |\eta| < 4.9$, which corresponds to an angle of approximately 1 to 5 degrees from the beam-line. It is comprised of three active modules, FCAL1, FCAL2 and FCAL3 and a dense shielding layer to prevent jet punch-through. FCAL1 measures energy of electrically charged particles using a copper absorbing material. This module is closest to the interaction point and thus absorbs the

largest amount of radiation. Behind it are FCAL2 and FCAL3 respectively, which are made of a tungsten active material in order to optimize both longitudinal and transverse hadronic shower containment in the available space.

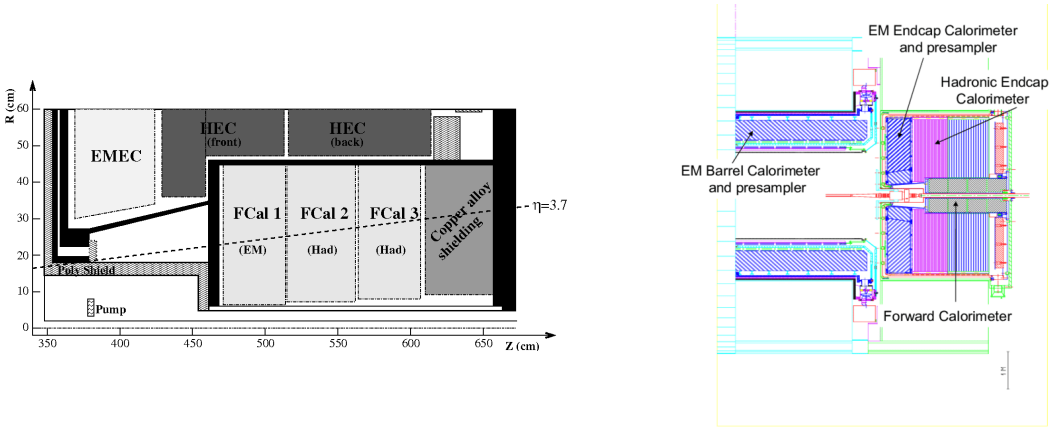

Figure 11: A cross-sectional view of the forward calorimeter (left, from [2]) in the cryostat support tube which houses it. Calorimetry material is shown in various grey gradients and the cryostat walls are shown in black. Non calorimetric material is located between the forwarded calorimeters and the interaction point, due to unavoidable construction constraints. The Poly Shield which shields the cryostat bulkhead is designed to reduce albedo from the calorimeter back into the inner detector. The cyrostat assembly fits within the end-cap calorimeters (right, from [3])

Tungsten is comprised of heavily nucleons, which increases the strong interaction rate, leading to a decrease in the radiation length of strongly interacting particles in this material. The hadronic componet of jets is comprised mostly of light mesons (such as pions) and some hadrons. These interact with the tungsten nucleons, and lose their energy quickly via subsequent hadron interactions or ionization. Typically neutrons or protons will undergo a series of elastic scatterings, where the average energy transfer per scattering is very low. This processes will continue until they are eventually captured by some nucleus. The most extreme case is neutron decay with a half-life time of about 15 minutes [15]. These considerations are taken into account, in-order to provide the highest possible energy resolution in this forward region.

The FCAL has the important advantage of optimizing hermeticity within the liquid argon

volume; however, it brings the FCAL very close to the circulating beams and exposes it to a high radiation flux. In order to survive in this region, the FCAL is constructed in as simple a fashion as possible, using only radiation hard materials [3]. In order for the FCal to operate in this high-flux environment, the liquid argon (LAr) gaps must be much smaller than the 1–2 mm that is traditional in a LAr calorimeter [2]. This constraint is accommodated by using thin, annular LAr gaps oriented parallel to the beamline. Electrodes are formed by inserting an absorber rod, which serves as the anode, into a copper tube which acts as the cathode. The rod is positioned concentrically using a helically-wound radiation hard plastic fiber that maintains the exceptionally thin gap between the anode and cathode (269μm in FCAL1). In order to reduce the amount of neutron albedo in the inner detector cavity, the front face of the FCAL is away from EM calorimeter front face by about 1.2 m.

Read-out from the calorimeter is reconstructed first as energy or "topo"-clusters. These clusters are then used in electron and photon identification (EM layers), and jet reconstruction (Hadronic and EM layers).

2.5 Muon Spectrometer

The Muon Spectrometer (MS) is the outer-most layer of the ATLAS detector. The MS consists of jointly eight super-conducting coils arranged in an open-air toroid configuration. Various muon detecting subsystems arranged in three cylindrical layers or stations [16] are immersed in the 4 Tesla magnetic field provided by the toroid. Muon measurement by the MS begins about 5m from the interaction point, prior to which muon tracks can be identified in the inner-detector. Little energy is lost in the lead and iron active materials in the calorimeters due to the long radiation length (and correspondingly low stopping power) of GeV scale muons [17] in moderate Z-materials. The "Bethe" equation well accounts for losses in the 1-1000 GeV regime, above which bremmstralung effects dominate. Muon measurement extends to 10m in the radial direction and up to 20m in the axial direction. Sagitta measurement is performed over three stations to satisfy the second-coordinate and high momentum resolution design and physics goals of the MS [16], while point-angle measurements

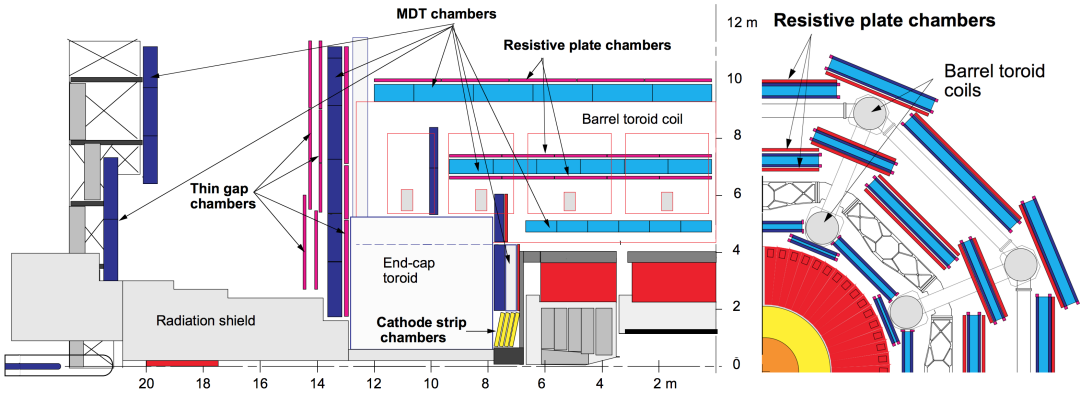

Figure 12: Side and cross-section view of the ATLAS muon spectrometer.

is possible for 2 station interactions in the forward regions. Muon identification is possible with 1 station interactions. The physical design of the sub-detector is shown in Fig. 12. The toroid operates at a design amperage of 20 kA, with a nominal field strength of 2 Tesla. The field runs radially about the interaction points, such that charge particles will bend with respect to the polar angle, or in rapidity.

Four types of instrumentation is employed, two high precision momentum resolution types and two fast types for triggering and time resolution. The high precision instrumentation relies mostly on monitored drift tube technology (MDT). These tubes are positioned laterally along η to provide a bending view of the MS. Stations composed of two poly-layers comprised of 2-3 mono-layers of drift tubes increases redundancy and provides spatial resolution of about 80 μm [16]. The Resistive Plate Chamber (RPC) is a gaseous detector providing space–time resolution of 1 cm 1 ns and digital readout, which enables bunch-cross identification. A trigger chamber is made from two rectangular detector layers, placed orthogonal where the ϕ strips provide the second-coordinate measurement required for the offline pattern recognition. The muon reconstruction efficiency as a function of p_{T} and η is shown for $J/\psi \to \mu\mu$ decays in Fig. 13, demonstrating muon identification and measurement for $|\eta| < 2.5$ and resolution [18].

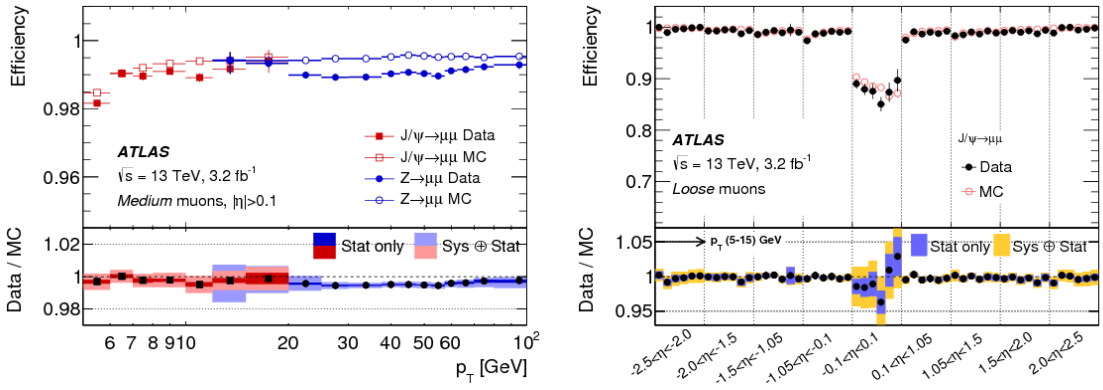

Figure 13: Muon reconstruction efficiency.

2.6 Trigger

The ATLAS experiment includes an online Trigger and Data Acquisition (TDAQ) system that selects events that will be saved to offline storage for later physics analysis [19]. This system is comprised of two levels, the first being a hardware based, low-granularity level-1 (L1) system with a design latency of 2.5 s. This system constructs Regions-of-Interest seeding the software based algorithms used in the subsequent high level trigger (HLT) system, reconstructing the event with full detector read-out granularity. The L1 system is further divided into three sub components, the Calorimeter Trigger (L1Calo), the Muon Trigger (L1Muon) and the Central Trigger Processor (CTP). The L1 system reduces the 40 MHz collision rate to 100 MHz, and the HLT trigger reduces the rate further to 3-4 kHz [3].

2.7 Computation Framework

The ATLAS collaboration uses an extensive software framework called Athena. This is a centralized code base shared across the entire ATLAS experiment, and serve detector operation and monitoring, event reconstruction, data derivation, Monte Carlo and detector

simulation, downstream data production, and physics analysis purposes. Athena is built on an underlying architecture called Gaudi, which was originally developed by LHCb. One of the primary features of the Gaudi architecture was the idea of a common tool, which could be shared across many algorithm instances. This design pattern needed some updates to accommodate multi-threaded environments, but the central structure remains the same. The algorithm is the essential building block of nearly all ATLAS analysis and operation, with an `initialize`, `execute`, and `finalize` methods. Considering the event as the basic unit around which almost all data is manipulated, this codifies the methodology across the collaboration. Globally available services expand this, like the `THistSvc` and `EvtStore` which manage persistence across instances for data access and collection.

Additionally, the ATLAS experiment needed to have peta-byte scale operations for the expected Run 2 data-set. To achieve this, a data derivation model [20] was implemented, and proceeds as following: The overall analysis model begins with event reconstruction using the Athena framework. This includes tracking and vertex reconstruction, electron and photon identification, muon reconstruction,jet reconstruction using FastJet, and missing transverse momentum which includes all visible physics objects as well as a soft term based on calorimeter and track-based objects not associated to any physics object [21].

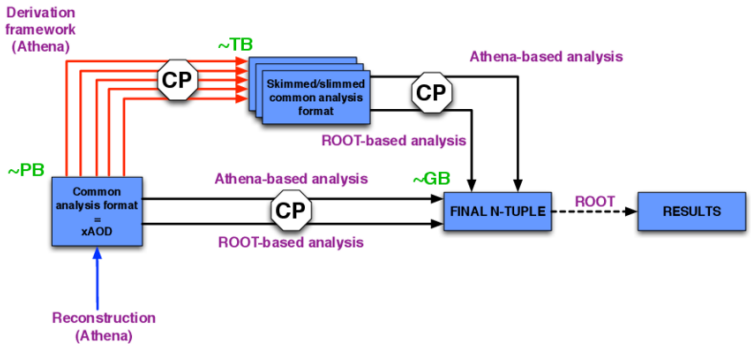

Figure 14: Overview of the ATLAS Run 2 analysis model.

To accommodate the variety of data-types and structures encountered, but keep these files ROOT readable, an auxiliary data store methodology, called the xAOD (Analysis object data) was introduced [22]. This has the advantage of being polymorphic across abstract data-structures, but without needing to rely on virtual C++ inheritance, which made the

old model impossible to read using the ROOT framework, on which most end-user analysis takes place. The central principle of the xAOD is the Container and AuxContainer. In particular, the AuxContainer can be decorated with nearly any data-type to describe and modify base-line data stored in the primary Container. For example, the associated track and calorimeter deposits for an electron can be written as decorating elements in this auxiliary container. The xAOD is the first common format in which both data and MC are produced.

From data, xAOD files are produced following reconstruction on a per-run basis and trigger the downstream production of DAODs which use basic skimming and slimming methods to reduce both events and data within events that are irrelevant for certain analysis types. For example, this analysis uses the `SUSY16` derivation, which requires two leptons in the AOD (skimming), and only keeps tracks associated with physics objects (slimming). This computational model is shown in Fig. 14. xAODs are also produced following reconstruction of simulated detector read-out (which is formatted the same as the real detector read-out) – the last-stage of the Monte Carlo production chain in ATLAS. Overall, physics analysis must span multiple stages of this data model, from read-out to final event selections.

3.0 Signal Model

There are a variety of ways in which beyond the Standard Model particles can be produced at the LHC. Being a hadron collider, a large flux of gluons and light quarks (the up, down, charm and strange) are present at the collision point, each carrying the momentum according to the parton distribution function. Ultimately, these particles collide or interact, and the center of mass energy between them can give rise to massive new particles.

3.1 Survey of Sparticle Production Modes

Given the large flux of gluons in conjunction with the strength of the strong force, strongly interacting particles of the MSSM are produced with the highest cross-section. The annihilation of two gluons into an off-shell, massive gluon (through the triliear gluon vertex) can readily produce gluinos and squarks with TeV scale masses through its open decay channels. The exclusions for these particles are strong, reaching about 2 TeV in [23].

The production of electro-weak particles (such as gauginos, higgsinos) most readily proceeds through the production of an off-shell Z/W boson, which can also readily decay to these particles through its now open decay channels. Off-shell Z/W production can be achieved through quark-quark annihilation, and also occurs with high, albeit lower, cross-sections. Common in both of these leading order processes is that the s-channel mediator has zero transverse momentum. Since it is the decay products of these particles which are ultimately detected, the energy released in these decay processes is relied upon to produce high p_{T} jets, leptons, and missing energy signals. Limitations of the trigger require high thresholds on these objects, and in the case of energetic decay processes, these thresholds are easily achieved.

There are scenarios which exhibit "compressed-spectra" between the mother and daughter particles. In these scenarios, little energy is released in the decays to standard model particles, and as such, only low p_{T} SM particles are produced, alongside heavy BSM parti-

cles. These objects either cannot be reconstructed, are lost down the beam-pipe (for having large longitudinal momentum with respect to their transverse momentum), involve large irreducible backgrounds, or fail the necessary criteria for online selection. All of these factors make such searches difficult.

One innovation to circumvent these pitfalls is to require initial state-radiation in the hard-process, which can occur from both radiated gluons or a quark in the gluon-quark initial state. During the scattering process, emission of an e.g. high p_{T} gluon from one of the colliding quark lines occurs with a probability roughly proportional to the strong coupling evaluated at the electroweak scale, about $\alpha_s = 0.12$. Combinatoric considerations make the overall emission probability approximately $\frac{1}{4}$. Since momentum is always conserved in the transverse plane, the corresponding sparticles carry transverse momentum equal and opposite to this gluon emission. Physically, a high p_{T} can undergo real QCD radiation, though this is usually highly collinear with the initial momentum vector. During hadronization, many final state particles are produced in a so-called collimated jet. This type of signal is generally characterized by some high energy decay products balanced by, or recoiling off, a high energy jet at central rapidity.

If producing LSPs, these escape detection and give rise to a strong missing-energy signal, which can be triggered upon online and selected against standard model backgrounds offline. If producing particles with compressed-spectra, the decay products have a transverse momentum that scales linearly with the jet p_{T} and with the ratio of the mass-splitting and mother particle mass, $p_{\mathrm{T}}^{\mathrm{vis}} = p_{\mathrm{T}}^{\mathrm{Jet}} \frac{\Delta M}{M_{\mathrm{NLSP}}}$. This kind of search was first performed for Higgsino-like neutralinos in [24] which exhibit natural compress-spectra with decoupled soft-masses for the wino and bino terms.

There exists another way to produce electroweakinos. Since quarks are also weakly interacting, there is also a flux of weak bosons with high center of mass energy. In the MSSM, there are three-point vertices between the electroweakinos and weak bosons, and so t-channel exchange of a electroweakino between these radiated weak bosons can pair-produce electroweakinos. While fundamentally a scattering process (somewhat distinct, but similar to a fusion process as with Higgs boson production), we refer to this as *VBF induced electroweakinos production*. This gives rise to a new type of striking signature, upon which

this analysis is based.

3.2 Motivation for Vector Boson fusion

The VBF production mode is not only interesting as a kinematic signature, but this specific analysis which targets the VBF+$E_{\mathrm{T}}^{\mathrm{miss}}$ + 2ℓ final state relates to a variety of beyond the Standard Model theories. One such theory is the MSSM, which is the simplified model we'll use in this analysis.

Other theories which predict a VBF signature include light (order GeV) sterile neutrinos produced through the Neutrino-Higgs vertex, or heavy neutrinos produced directly through weak boson fusion. In non-minimal version of the MSSM, some predict a light (also order GeV) pseudo-scalar produced through a supersymmetric exotic Higgs decay which, in certain regions of phase-space, decays to a resonant muon-pair [25]. Higgs production through VBF is well studied and becoming a competitive probe for Higgs-portal scenarios. Additionally, production of a doubly-charged Higgs like particle in the Type-II See-Saw model is possible through VBF, specifically W^+W^+ fusion (also enhanced as the flux of positive W^+ is larger than W^-). In certain regions of phase-space, the decay proceeds through W boson cascade decay with a same-sign, soft di-lepton final state with $E_{\mathrm{T}}^{\mathrm{miss}}$ with a compressed spectrum [26]. Within the family of non-minimal supersymmetric models, additional neutralino or charginos (or any spin $\frac{1}{2}$ particles) can play a non-trivial role in the vector boson scattering process. An EFT approach can also be taken to the $pp \to \chi\chi jj$ processes. A recent specific example (inspired heavily by recent VBF searches carried out at ATLAS/CMS), propose probing multipole moments in the context of dark-matter using the vector boson fusion (VBF) topology [27]. Bulk gravitons, in some regions of phase-space are readily produced through VBF and decay via weak bosons.

In general, this production mode is novel, unexplored at ATLAS, and exhibits unique properties. A search of this type, in effect, constitutes a search on the tails of the m_{jj} spectrum, with two hard-jets, and compressed topology.

3.3 Vector Boson Fusion (VBF)

A baseline feature of the vector boson fusion production mode is the existence of two energetic jets. These jets occur in the leading-order process, corresponding to the first expansion of a $pp \to X$ process in increasing orders of the electro-weak and strong vertices. The $W^{\pm}$ bosons carry only electric charge and isospin whereas the Z^0 boson carries no electric charge or weak isospin (an entirely neutral current), and neither carry the strong charge. This underpins the most important consideration for explaining the phenomenology of VBF events. Gluons are doublets of color charge, meaning that the primary gluon-quark interaction leads to a change in the quark color charge. This is similar to $W^{\pm}$-quark interactions where the electric charge of the quark is changed since the boson carries electric charge. In Z^0 interactions none of the quantum numbers of the interacting particles are changed since the Z^0 boson isn't charged under of the gauge fields.

Unlike charges under the electroweak symmetry group, the color charge displays the property of *confinement*. This arises due the characteristics of the strong potential, being monotonically (and at moderate distant scales, linearly) increasing with spatial separation of two quarks. In nature, only color-less states are observed, most commonly as hadrons and mesons. If one tries to create an isolated color state by ripping a valance quark from one of these colorless states, the energy required will eventually excite the vacuum and pair-produce two quarks which restore the local color neutral state of the system. As the distance further increases, dynamical screening occurs and the potential levels off.

Since the weak bosons are color singlets, they do not carry color charge quark lines. Since gluons are a doublet of color charge, they can carry the color charge across the quark lines and swap the colors of the interacting partons. Alternatively, gluon emission will also carry a color charge away from a quark line, producing tension within the gluon field. This consequently correlates the color-neutral states between the initial and final state particles with respect to the parent proton remnants. Examples of colorful and colorless exchange are shown in Fig. 15

During hadronization (which restores all color neutral states and occurs at distance scales of approximately 1 fm) energetic exchange of gluons initiates hadronic radiation into

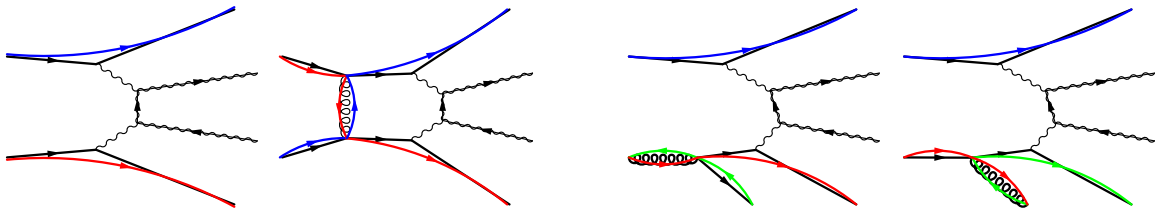

Figure 15: Tree-level VBF process with example color-lines included. From left to right is the tree-level process (LO), a loop diagram with color-exchange (NLO), a gluon initiated (NLO), and a gluon emission (NLO) diagram. In all cases depicted, the blue and red valance charges interact.

the region between the two outgoing jets. In the leading-order case, hadronic radiation is confined to high rapidities between the outgoing parton and net-valence charge of the proton remnants lost down the beam pipe. This means that the net-colorless states required by color confinement have collinear momenta near the beam-axis, and will hadronize as such within these regions. If the outgoing partons are color correlated, hadronic radiation occurs in between the two jets due to Sudakov radiation, in which the mere existence of gluon interactions may result in a central jet at low rapidity. This is the principal of the so-called "suppressed central hadronic radiation" as found characteristic in events with singlet color exchange. A schematic of this process is depicted in Fig. 16.

Figure 16: Parton level schematic of color correlation in a VBF event. Left involves no color exchange in the t-channel for the hard process while the right shows some color exchange. Time is implied and the horizontal direction corresponds to the beam axis, and the vertical direction corresponds to transverse momentum. The grey blobs represent hadronization, with some example gluon interactions depicted.

3.4 Model

VBF-induced electroweakino pair-production are investigated for both the compressed Wino-Bino and Higgsino cases. The decay of the NLSP via a highly off-shell Z* provides a strong signature to suppress Standard Model backgrounds. The invariant mass of two leptons, $m_{\ell\ell}$, from this decay has a kinematic cut-off at the mass-splitting, and thus this appears as a spectrum (since no Z resonance is possible) of values low values $m_{\ell\ell}$.

There are a number of actual diagrams which contribute to the total cross-section of the target final state, shown in Figure 17. These signal processes serve as the essential hypothesis of this analysis, that in the data collected by the ATLAS detector is an excess of events which fit this signal process. Since we can't know *a priori* what the exact parameters of this signal model would be, multiple points are generated. The mass differences,ΔM between the NSLP and LSP is varied between 1 and 40 GeV. These benchmark points served primarily as optimization points, and for analysis of the model independent limits after unblinding.

3.5 Simulation of VBF Induced Electroweakino Production

MadGraph5 [28] is an efficient and fast general purpose matrix-element based event generator. This program handles diagram generation, matrix element integration, and hard-process simulation for general $2 \to n$ processes. The first step of the algorithm execution is to specify the target processes within a certain model. Any model with a Lagrangian density can be implemented. The MSSM-SHLA2 model is a SHLA2 compliant version of the MSSM, and includes the 6 electroweakinos of the MSSM using the particle labels $n1, n2, n3, n4, x1, x2$. From a given process definition, diagrams which respect the given Feynman rules of the model are generated, and the heliicy amplitude of these diagrams is constructed using successive calls to a helicity amplitude function library HELAS.

In the VBF topology, two protons scatter, producing two parton jets and two electroweakinos in the tree level scattering process. Jets in general are represented using the

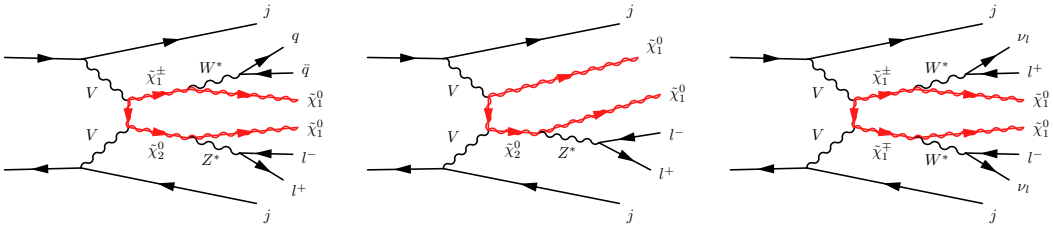

Figure 17: Feynam diagrams for the three signal processes which contribute to the overall visible cross-section. From left to right is neutralino-chargino pair production which is present for both the Wino-Bino and Higgsino case, neutralino pair production, which vanishes in the pure Wino-Bino limit, and opposite-sign chargino pair-production, with the same-sign process vanishing in the pure limit. All Z decays proceed via leptons, while the W is allowed to decay to hadrons or leptons in the chargino pair case. Each gives rise, then, to two jets, missing energy, and two opposite-sign leptons.

multiparticle label j. One can then specify orders of the strong and electroweak vertices in the process definition. To eliminate Drell-Yann production through $q\bar{q} \to Z$, which is an $\mathcal{O}(\alpha_s) = 2$ process, setting $\mathcal{O}(\alpha_s) = 0$ is sufficient. Additionally, exclusion of diagrams involving scalar squarks (included as $\mathcal{O}(\alpha)$ processes) is useful to decreased integration time. Since the scalar squark sector is assumed to be decoupled in our simplified model, this has negligible effects on the resultant cross-section and distributions. An example of a process command is:

```
generate p p > n2 n1 j j QCD=0 \ susystrong
```

Diagrams at $\mathcal{O}(\alpha) = 4$ with two parton jets in the matrix element include both the target diagram (VBF induced production) and associated production diagram, in which a Z or W boson decays to quarks. Inclusion of these diagrams is not desired, as it does not give rise to the high m_{jj} signature since $m_{jj} \sim m_{qq} \sim m_Z$. To ensure removal of these diagrams, a cut on the parton level invariant mass between the two partons is used. We have determined that this cut must be about 200 GeV lower than the nominal analysis cut on m_{jj} due to unphysical

effects introduced following the parton shower step. This cut must also be sufficiently higher than the Z mass to ensure removal of the associated production processes. The value of 200 GeV is chosen to satisfy both of these criteria, and is shown to significantly enhance purity of the simulated process. Additionally, a cut on the jet merging and energy scale of 15 and 12 GeV improves generation speed by removing infrared gluon or quark processes. No other VBF-style cuts are implemented, such hard cuts on the hard-process only further introduce unphysical effects that skew and distort the distributions following showering; in general it is best to minimize kinematic cuts at the generator level. The most relevant kinematic parameters are as follows:

```
mmjj = 200   ! Minimum invariant mass between two partons
xqcut = 15   ! Minimum jet momentum measure between partons
ptj = 12    ! Minimum jet transverse momentum
ebeam1 = 6500  ! Beam 1 total energy in GeV
ebeam2 = 6500  ! Beam 2 total energy in GeV
```

Closure of the configuration with and without the m_{jj} cut is achieved at and around 400 GeV, showing that efficient removal of unwanted events is achieved without spoiling the target distributions. The CKKW-L merging scheme is used to match jets from the hard process during with a scale of 15 GeV to match the jet momentum cut. The parton distribution function (PDF) used is NNPDF230LO.

3.6 Validation

The two leading-order jets which characterize the VBF process should be highly energetic and exhibit unique angular relationships. Looking at base-line, truth-level quantities would ensure that the tree-level process dominates over associated production. Fig. 18 shows key validation plots demonstrating the expect VBF-topology being reproduced for VBF induced electroweakino production.

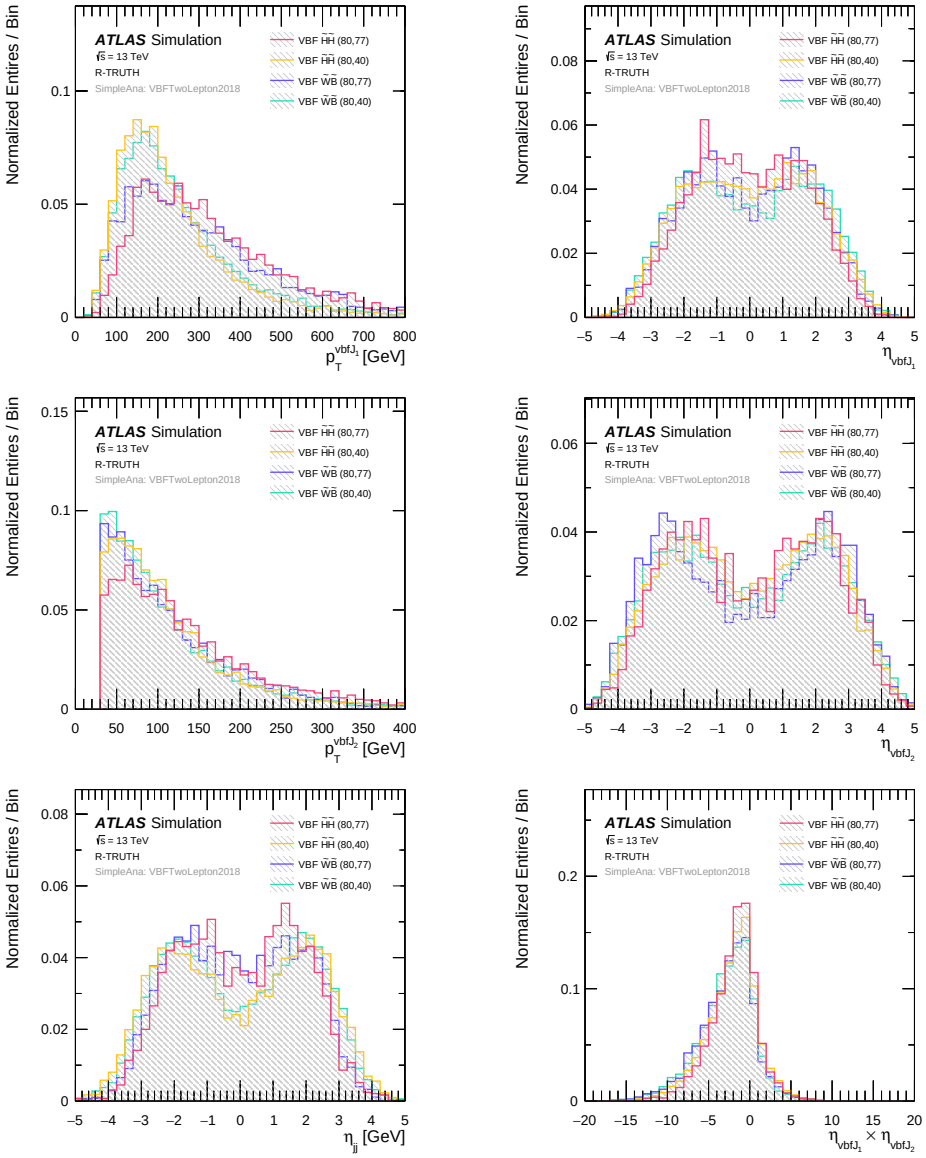

Figure 18: Truth-level reconstructed quantities for the leading and sub-leading VBF tag jets for a few example signal models. The two jets are highly energetic (top, middle left) and lay at moderate-to-high rapidity (top middle right). Since the two jets originate from partons with opposite longitudinal momentum, it is expected that the rapidity gap between them is large (bottom left) and that the product of their rapidity is negative or that the jets are "back-to-back" (bottom right).

4.0 Data Reconstruction and Kinematic Variables

Physics object candidates are first reconstructed from signal collected and saved from the ATLAS sub-detectors. Electrons reconstruction is first seeded by calorimeter deposits in the form of clusters identified by a sliding window algorithm. This window scans the calorimeter read-out in steps of $\Delta\eta, \Delta\phi = 0.025$ with a fixed window size of $\eta \times \phi = 3 \times 5$. Clusters identified by this algorithm are then matched to tracks in the inner-detector. Energy information in the surrounding region, including the transition layers, are combined to calculate the four-momentum of these electron candidates. Muon candidates begin with hits form one of the four sub-detectors of the muon spectrometer. Muons which interact with three or more stations in the MS can be fully reconstructed, with their track extrapolated to the interaction point and associated with the primary vertex. Muons which have MS tracks matched to an inner detector track are called combined muons, and have the greatest purity. Muons without an associated ID track but a complete MS track are called standalone muons, and are not used in this analysis. Segment-tagged muons leave two hits in the MS, but have an ID track, and are also considered in this analysis. Jets are reconstructed using electromagnetic clusters using the anti-k_{T} algorithm, tempered by a size parameter, R, defining the radius of the jet. This algorithm iteratively considers individual energy deposits, and either adds them to a kind of "jet-in-progress" object or removes them, recalculating the jet axis each time. This is continued until no objects are left for assignment. This results in conical jets, and is IR-safe and boost-invariant. This allows for the easiest interpretation of these objects as emanating from parton emissions in the matrix element.

Data is collected from 140.5 fb^{-1} worth of collisions at $\sqrt{s} = 13$ TeV. The derivation used requires at least two candidate leptons and one jet or missing energy. Data is cleaned according to the below criteria; only data events which pass these selections are considered.

1. The ATLAS detector was running with no intolerable defects during stable beams.
2. The event contains a primary vertex. This is defined as a single vertex matched to at-least 4 tracks with $p_{\mathrm{T}} > 400$ MeV.
3. The event data is complete and not corrupted. Trigger and data flow problems can

corrupt some events, and these are removed.

4. The event does not contain cosmic muons. Muons can pass through the detector during collision events, and manifest as MS tracks matched on both sides of the detector apparatus. Sometimes these can imitate a real muon from the interaction point, and so a cut on the transverse and longitudinal impact parameters is applied.
5. The event doesn't contain non-collision background or bad-jets. Hardware noise bursts, cosmic showers, or beam effects can introduce detector-level effects which namely impact jet-shape. Events with jets identified as not matching genuine jets are removed.

4.1 Data and Simulation Samples

Several background processes are studied and modelled using Monte Carlo simulation. Single boson production with associated jets involving leptonically decaying Z and W bosons are modelled using Sherpa with the NNPDF30NNLO PDF set. The matrix element is generated with up to four partons at leading order. Merging with the parton shower is handled in-situ by the ME+PS@NLO prescription. The samples are sliced in max$H_T p_{\mathrm{T}} V$ and quark flavor content. The Z+jets samples are further separated by lepton kinematics:

- The on-shell Z+jets samples require $m_{\ell\ell} > 40$ GeV.
- The "low-mass" Z+jets samples have a generator-level requirement of $10 < m(\ell\ell)/\mathrm{GeV} < 40$ GeV and lepton p_{T} requirements of 5 GeV on the leading and subleading leptons.
- The "very-low-mass" Z+jets samples complete the coverage down to $2 * m(\ell) < m(\ell\ell) < 10$ GeV and lepton $p_{\mathrm{T}} > 2$ GeV. These samples are inclusive in quark flavor and only available for the $140 <$ max$H_T p_{\mathrm{T}} V < 280$ GeV and max$H_T p_{\mathrm{T}} V > 280$ GeV slices.
- Additional "very-low-mass" Z+jets samples were requested for the $70 <$ max$H_T p_{\mathrm{T}} V < 140$ GeV slice, to cover the phase-space explored in the new low-$E_{\mathrm{T}}^{\mathrm{miss}}$ channel.

Modeling of diboson production (WW, ZZ, WZ) and leptonic triboson processes (VVV) uses Sherpa The NNPDF30NNLO PDF set is used, and these samples are similarly separated by lepton kinematics:

- The primary samples have a generator level cut on the leptons of $p_{\mathrm{T}} > 5$ GeV, and require $m(\ell\ell) > 4$ GeV for events with two same-flavor opposite-sign leptons.
- A second set of samples complement the primary samples down to $p_{\mathrm{T}} > 2$ GeV and $2 * m(\ell) < m(\ell\ell) < 10$ GeV.

Single Higgs production via gluon–gluon fusion (ggF) and vector boson fusion (VBF) processes decaying via fully leptonic WW or directly into two leptons are modelled using Powheg interfaced with Pythia 8 for parton showering and hadronization, using the NLOCTEQ6L1 PDF set. Processes involving single Higgs in association with a Z or W are simulated using just Pythia 8 using the NNPDF23LO set. Top quark par production is modelled using aMC@NLO interfaced with Pythia 8, while Powheg interfaced with Pythia 8 for showering is used for single top production (t- and s-channel), tW and $t\bar{t}$ processes. These samples are then interfaced with ATLAS detector simulation and reconstruction software and stored in the same format as real collected data.

4.2 Object Definitions

4.2.1 Leptons, Jets, and Missing Transverse Energy

The ATLAS experiment recommends certain criteria to define the physics objects accessed as reconstructed objects from the ATLAS detector. In general, tighter criteria (referring to isolation, quality, likelihood, sub-object use, or energy level) result in greater background rejection with enhance signal purity. For this consideration, this analysis considers objects divided into two categories: *signal* objects, being a subset of *baseline*, where the former satisfy more stringent quality and isolation requirements. Baseline objects undergo the default overlap removal procedure to prevent double counting signal objects. Baseline objects undergo overlap removal, which uses a collections of electrons, muons, jets, taus, and photons. Overlapping objects are identified with ΔR matching between the object location or between shared tracks in the inner detector. Large-R jets, photons, and taus are not used in the OR procedure. Boosted electrons and b-tagging are used. The order of overlapping objects removed is as follows:

1. Electrons matched to electrons
2. Electrons matched to muons
3. Electrons matched to any jet
4. Muons matched to any jet

This prevents double counting of objects. One such way this can occur when two different algorithms reconstruct a baseline object using the same seed-track, or leptons tracked within a jet. Matching of these tracks (or objects) ensures removal of one of these objects.

Electrons Baseline electrons are reconstructed using inner detector tracks matched to energy clusters in the electromagnetic calorimeter. These satisfy kinematic requirements of $p_{\mathrm{T}} > 4.5$ GeV and $|\eta| < 2.47$. A likelihood based identification function is built, using information such as hadronic leakage, shower-shape information, inner-detector hits, radiation in the TRT, and cluster-track matching. We use the *VeryLoose* working point described in [29].

The longitudinal impact parameter of baseline electron tracks is required to satisfy $|z_0 \sin\theta| < 0.5$ mm. Signal electrons must in addition pass *Gradient* isolation, likelihood-based *Medium* identification criteria, together with impact parameter satisfying the transverse $|d_0/\sigma(d_0)| < 5$ requirement. Electrons seeded by photon conversion reconstruction algorithms are rejected.

Muons Baseline muons are reconstructed by combining tracks from the inner detector and the muon spectrometer subsystems. The *LowPt* identification criteria are applied. Baseline muons are required to have $p_{\mathrm{T}} > 3$ GeV and $|\eta| < 2.5$, with tracks satisfying the $|z_0 \sin\theta| < 0.5$ mm requirement on the longitudinal impact parameter. Signal muons must in addition pass the *FixedCutTightTrackOnly* isolation requirement on the track isolation, together with satisfying a $|d_0/\sigma(d_0)| < 3$ requirement on the transverse impact parameter.

Jets Jets are reconstructed from topological clusters in the calorimeters using the anti-k_t algorithm with radius parameter $R = 0.4$. Baseline jets are required to have $p_{\mathrm{T}} > 20$ GeV and $|\eta| < 4.5$. Pileup mitigation using the jet vertex tagger (JVT) employing the *Medium* working point is applied for jets satisfying $p_{\mathrm{T}} < 120$ GeV and $|\eta| < 2.4$. Pileup mitigation for forward jets using the forward jet vertex tagger (fJVT) employing the *Loose* working point is applied for jets satisfying $p_{\mathrm{T}} < 50$ GeV and $|\eta| > 2.8$. Signal jets satisfy $p_{\mathrm{T}} > 30$ GeV and $|\eta| < 2.8$. Forward signal jets satisfy $p_{\mathrm{T}} > 30$ GeV and $|\eta| < 4.5$ and $|\eta| > 2.8$. Baseline jets within $|\eta| < 2.5$ originating from b-hadrons are identified with the *MV2c10* algorithm, using the 85% working point.

Photons EM clusters that are reconstructed and identified as photons are calibrated as photons when computing $E_{\mathrm{T}}^{\mathrm{miss}}$. Photons are required to have p_{T} ¿25 GeV and pass the *Tight* identification criteria.

Missing transverse momentum The missing transverse momentum $\mathbf{p}_{\mathrm{T}}^{\mathrm{miss}}$ with magnitude $E_{\mathrm{T}}^{\mathrm{miss}}$ is constructed using `SUSYTools`. The *Tight* working point is used. It is defined as the negative vector sum of the transverse momenta of all identified physics objects (electrons, photons, muons, jets) and an additional soft term. The soft term is constructed from all tracks that are not associated with any physics object, and that are associated to the primary vertex. In this way, the missing transverse momentum is adjusted for the best calibration of the jets and the other identified physics objects above, while maintaining pileup

independence in the soft term.

Property	Signal	Baseline
Electrons		
Kinematic	$p_{\mathrm{T}} > 4.5$ GeV, $\lvert\eta\rvert < 2.47$ (include crack)	$p_{\mathrm{T}} > 4.5$ GeV
Identification	MediumLLH	VeryLooseLLH
Isolation	Gradient	–
Impact parameter	$\lvert d_0/\sigma(d_0)\rvert < 5$, $\lvert z_0 \sin\theta\rvert < 0.5$ mm	$\lvert z_0 \sin\theta\rvert < 0.5$ mm
Reco algorithm	Veto `author==16`	Veto `author==16`
Muons		
Kinematic	$p_{\mathrm{T}} > 3$ GeV, $\lvert\eta\rvert < 2.5$	$p_{\mathrm{T}} > 3$ GeV
Identification	LowPt	LowPt
Isolation	FCTightTrackOnly	–
Impact parameter	$\lvert d_0/\sigma(d_0)\rvert < 3$ & $\lvert z_0 \sin\theta\rvert < 0.5$ mm	$\lvert z_0 \sin\theta\rvert < 0.5$ mm
Jets (Anti-k_t $R = 0.4$ EMTopo)		
Kinematic	$p_{\mathrm{T}} > 30$ GeV, $\lvert\eta\rvert < 2.8$	$p_{\mathrm{T}} > 20$ GeV, $\lvert\eta\rvert < 4.5$
Pileup mitigation	JVT Medium for $p_{\mathrm{T}} < 120$ GeV, $\lvert\eta\rvert < 2.4$	–
b-Jets (Anti-k_t $R = 0.4$ EMTopo)		
Kinematic	$p_{\mathrm{T}} > 20$ GeV, $\lvert\eta\rvert < 2.5$	$p_{\mathrm{T}} > 20$ GeV, $\lvert\eta\rvert < 4.5$
Pileup mitigation	JVT Medium for $p_{\mathrm{T}} < 120$ GeV, $\lvert\eta\rvert < 2.4$	–
b-tagging	MV2c10 FixedCutBeff 85%	–
Forward jets (Anti-k_t $R = 0.4$ EMTopo)		
Kinematic	$p_{\mathrm{T}} > 30$ GeV, $\lvert\eta\rvert < 4.5$, $\lvert\eta\rvert > 2.8$	$p_{\mathrm{T}} > 20$ GeV, $\lvert\eta\rvert < 4.5$, $\lvert\eta\rvert > 2.8$
Pileup mitigation	fJVT Loose for $p_{\mathrm{T}} < 50$ GeV, $\lvert\eta\rvert > 2.5$	–

Table 1: Summary of object definitions.

4.2.2 Isolation for nearby leptons

The use of isolation cones was designed to distinguish high-energy electrons and muons from jets mimicking such objects, as genuine leptons are expected to have limited hadronic radiation near-by, and rejection of such events with radiation is ideal. However, a high p_{T} lepton within another isolation cone, treated generically, greatly increases the p_{T} fraction within the cone. This is not ideal, as in some analyzes, these events are signal-like and should be kept.

This effect is corrected using a dedicated `NearbyLepIsoCorrection` tool. The tool checks baseline leptons that fail the isolation criteria for other nearby baseline leptons that lie within its isolation cone. Tracks associated with the nearby lepton are then removed from the track isolation sum. If the nearby lepton is an electron, the topo-cluster E_{T} of the nearby electron is additionally removed from the calorimeter isolation sum. The corrected track and/or calorimeter isolation criteria are then re-calculated using the original isolation working point. While this tool demonstrated correction for these objects, more studies are needed to understand the effect this correction has on the fake-factor estimation. Since the fake-factors are correlated with acceptance rates based on isolation criteria, a tool which effects these rates can have a non-trivial effect on these estimations. For this iteration of the analysis, events which would instantiate the use of this tool are removed from all final selections.

4.3 Discriminating Variables

There are a variety of variables constructed from the kinematic properties of the calibrated physics objects accessed within the event loop algorithm. This is the formal description of the variables as implemented in C++ code. Calibration and derivation of these variables is done within the same algorithm. The structure of the framework utilized in this analysis is roughly sketched as follows:

1. A list of DAOD files to be processed is loaded. Based upon the number of files and user parameters, submissions to the local cluster system (at the Brookhaven National Laboratory Tier 3 facility) are prepared.
2. Each node picks up a configuration file will steers another framework, SUSYTools, setting object definition and working points as described in Section 4.2.
3. The n-tuple output is defined and all calibration tools are called and initialized.
4. For each event, objects are accessed in the DAOD, calibrated, then stored as a vector of AnalaysisObject classes.
5. These AnalysisObjects are accessed in the eventloop and intermediate variables are computed.
6. A flat n-tuple containing variable outputs for each event is saved for each node worker.
7. All n-tuples produced for a common DAOD production are merged.

The types of intermediate variables described fall under four major categories: Non-leptonic, Lepton Sensitive, VBF specific, and Recursive.

4.3.1 Non-leptonic

The following kinematic variables make no explicit reference to lepton information, only leverage information about the jet and missing transverse momenta.

The vector $E_{\mathbf{T}}^{\mathbf{miss}}$ is defined as (E_x^{miss}, E_y^{miss}), where :

$$E_{x,y}^{miss} = -[\Sigma p_{x,y}^{a} + \Sigma p_{x,y}^{b}] \tag{4.1}$$

Thus, this vector provides the amount of missing transverses momentum ($E_{\mathrm{T}}^{\mathrm{miss}}$) and its direction in the transverse plane.

Missing transverse momentum due to jet mis-measurements is often aligned with a specific jet axis since the jet axis defines the direction of this mis-mreasurement. The variable $\min\left|\Delta\phi(\text{all jets}, \mathbf{p}_{\mathrm{T}}^{\mathrm{miss}})\right|$computes the minimum angular separation between all jets and $E_{\mathrm{T}}^{\mathrm{miss}}$. This will reduce contributions such as QCD and Z+jets.

The number of jets is a proxy to quantify the hadronic activity in events. The number of jets N_{jets} counts how many jets satisfy the criteria outline for signal jets. This metric considers the VBF signal jets, which covers the full η range of the detector. From a sub-set of these jets, the number of b-tagged jets $N_{\mathrm{b-jets}}$ is computed. The electroweakino signal is not enhanced in heavy flavour quarks, and only produce identified b-tagged jet as a result of jet mis-ID. Therefore, rejecting jets tagged as arising from a b-quark, the predominate decay product of the top quark significantly reduces these backgrounds. Using b-tagging down to $p_{\mathrm{T}} > 20$ GeV jets at the 85% working point has been studied to improve $t\bar{t}$ rejection while retaining good signal acceptance. These are the loosest cuts supported.

4.3.2 Lepton sensitive

The following variables explicitly refer to leptonic information in an event. The kinematic relationships between these variables allows for partial uncovering of the electroweak structure of the event. The reasons for which some of the standard model backgrounds enter the signal region can be exploited to further reject these events.

First, the number of both baseline and signal electrons is considered. This provides specificity to processes with exactly two genuine leptons in the final state: the looser baseline selection is more likely to pick-up a third lepton, while the tighter signal selections reject fake and non-prompt leptons from one lepton processes. Additionally, the flavor correlation of these leptons can be exploited. The expected decay channel is through an off-shell Z decay, which would produce leptons of the same flavor (such as to not be flavor violating). Thus, a same flavor requirement is placed on signal region leptons to reject processes that give rise to different flavor final states (such as diboson and top quark pair production).

These two leptons will also exhibit certain angular characteristics. The $\Delta R_{\ell\ell}$, i.e the dilepton distance, is defined as :

$$\Delta R_{\ell\ell} = \sqrt{(\eta_{\ell_1} - \eta_{\ell_2})^2 + (\phi_{\ell_1} - \phi_{\ell_2})^2}. \tag{4.2}$$

This is a powerful variable for two reasons. As already hinted at in previous sections, subtle track-mismeasurement can give rise to two reconstructed leptons off the same track. These will be extremely close together, and is a large instrumental effect that can be nearly fully reduced. It was found that this effect falls off around $\Delta R_{\ell\ell} = 0.05$, which motivates this cut as a generic cleaning. Additional cuts on the lepton distance is motivated by the the NearbyLepIsoCorrection tool. This tool was only calibrated for high p_{T} objects, and as a result, the following requirements are needed for final states with 2 leptons: $\Delta R_{ee} > 0.3$ and $\Delta R_{e\mu} > 0.2$. This remove the chance any unexpected behavior with low p_{T} electrons in particular.

The dilepton invariant mass $m_{\ell\ell}$ is used both to suppress backgrounds in addition to exploiting a signal shape. An upper bound on the invariant mass of the two reconstructed leptons is placed at 60 GeV. This conservatively vetos the same flavour Z+jets in addition to $ZZ \to \ell\ell\nu\nu$ processes. The upper bound also helps in suppressing harder leptons from SM processes such as WW and $t\bar{t}$. The transverse mass, $m_{\mathrm{T}}^{\ell_1}$, is defined as the $m_{\mathrm{T}} = \sqrt{E_{\mathrm{T}}^{\mathrm{miss}} p_T}\cos(\Delta\phi)$. This variable can partially reconstruct the $W(\to \ell\nu)$ in order to veto this process.

The ratio of the total $E_{\mathrm{T}}^{\mathrm{miss}}$ and lepton p_{T} sum, $E_{\mathrm{T}}^{\mathrm{miss}}/H_{\mathrm{T}}^{\mathrm{leptons}}$, discriminates between events with soft and hard leptonic activity. The $H_{\mathrm{T}}^{\mathrm{leptons}}$ is defined as the scalar sum the lepton momenta

$$H_{\mathrm{T}}^{\mathrm{leptons}} = \sum_{i}^{\mathrm{leptons}} p_{\mathrm{T}}^{\ell_i}. \tag{4.3}$$

For a given value of $E_{\mathrm{T}}^{\mathrm{miss}}$, background processes from diboson and $t\bar{t}$ tend to have harder leptons, hence reducing the values of $E_{\mathrm{T}}^{\mathrm{miss}}/H_{\mathrm{T}}^{\mathrm{leptons}}$. In compressed signal events, the $E_{\mathrm{T}}^{\mathrm{miss}}$ is largely due to balancing against the hadronic recoil momentum with little contribution from the soft leptons, favouring larger values of $E_{\mathrm{T}}^{\mathrm{miss}}/H_{\mathrm{T}}^{\mathrm{leptons}}$. Selecting events with larger

$E_{\mathrm{T}}^{\mathrm{miss}}/H_{\mathrm{T}}^{\mathrm{leptons}}$ improves background rejection while maintaining a high signal acceptance for smaller mass splittings.

The di-tau invariant mass $m_{\tau\tau}\left(p_{\ell_1}, p_{\ell_2}, \mathbf{p}_{\mathrm{T}}^{\mathrm{miss}}\right)$ used in this analysis is defined by Equation (4.9), which is a function of the measured leptonic p_{ℓ_1}, p_{ℓ_2} and transverse missing momenta $\mathbf{p}_{\mathrm{T}}^{\mathrm{miss}}$ related by Equations (4.6) and (4.7). This variable aims to reconstruct the fully leptonic $Z \to \tau\tau$ processes to provide leverage on this background. Figure 19 illustrates this system schematically. By reconstructing the tau 4-momenta p_{τ_i}, the invariant mass squared $m_{\tau\tau}^2 = (p_{\tau_1} + p_{\tau_2})^2$ of the Z can be calculated and appropriately vetoed. Various definitions of $m_{\tau\tau}$ exist in the literature to resolve the kinematic ambiguities due to immeasurable neutrino momenta by imposing assumptions on the underlying process. This analysis primarily follows Refs. [30, 31, 32].

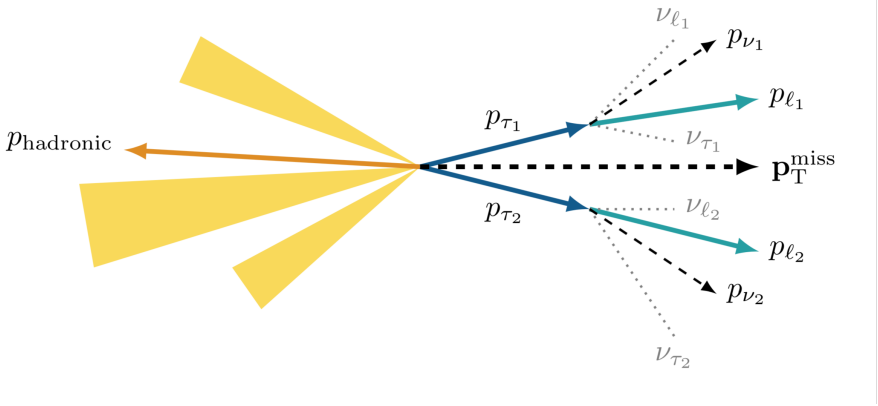

Figure 19: Schematic illustrating the fully leptonic $(Z \to \tau\tau)$ + jets system motivating the construction of $m_{\tau\tau}$.

In the $Z \to \tau\tau$ process where both taus undergo leptonic decays $\tau \to \ell\nu_\ell\nu_\tau$, only the missing transverse momentum $\mathbf{p}_{\mathrm{T}}^{\mathrm{miss}}$ and 4-momenta of the two leptons p_{ℓ_i} from the i-th tau are observable, where $i = \{1, 2\}$ label the tau decay chains. The reconstruction relies on the large boost of the taus, decaying from the Z recoiling off hadronic activity. This boost ensures the daughter leptons and neutrinos are nearly collinear, so the 4-momentum of the neutrino system p_{ν_i} from the i-th tau defined by $p_{\nu_i} = p_{\nu_{\ell_i}} + p_{\nu_{\tau_i}}$, is well approximated as a rescaling of the visible lepton momenta $p_{\nu_i} \simeq \xi_i p_{\ell_i}$, where ξ_i is a scalar to be determined. The

i-th tau 4-momentum is the sum of the daughter lepton and neutrino system $p_{\tau_i} = p_{\ell_i} + p_{\nu_i}$. Then the τ momentum is a rescaling of the observable lepton momenta p_{ℓ_i}

$$p_{\tau_i} = (1 + \xi_i) p_{\ell_i} \equiv f_i p_{\ell_i}, \tag{4.4}$$

where $f_i \equiv 1 + \xi_i$. To solve for the two unknown scalars ξ_i, one constrains the neutrino momenta using the missing transverse momentum [1] as Ref. [32] prescribes

$$\mathbf{p}_{\mathrm{T}}^{\mathrm{miss}} = \xi_1 \mathbf{p}_{\mathrm{T}}^{\ell_1} + \xi_2 \mathbf{p}_{\mathrm{T}}^{\ell_2}. \tag{4.5}$$

Equation (4.5) assumes the lepton–invisible colinearity limit $p_{\nu_i} \simeq \xi_i p_{\ell_i}$ and comprises two independent constraints in the transverse plane for the two unknown scalars ξ_i. This is solved by performing 2×2 matrix inversion in for example the x-y transverse plane

$$\begin{pmatrix} \xi_1 \\ \xi_2 \end{pmatrix} = \frac{1}{p_x^{\ell_1} p_y^{\ell_2} - p_x^{\ell_2} p_y^{\ell_1}} \begin{pmatrix} p_x^{\mathrm{miss}} p_y^{\ell_2} - p_x^{\ell_2} p_y^{\mathrm{miss}} \\ p_y^{\mathrm{miss}} p_x^{\ell_1} - p_x^{\mathrm{miss}} p_y^{\ell_1} \end{pmatrix}. \tag{4.6}$$

Assuming highly boosted taus such that $m_{\tau_i}^2 \simeq 0$, the di-tau invariant mass squared is then given by

$$m_{\tau\tau}^2 = (p_{\tau_1} + p_{\tau_2})^2 \simeq 2 p_{\ell_1} \cdot p_{\ell_2} (1 + \xi_1)(1 + \xi_2). \tag{4.7}$$

An important feature of $m_{\tau\tau}^2$ in Equation (4.7) is not only that it can go negative, but also in an asymmetric way such that the absolute value of the negative range of values $(m_{\tau\tau}^2)^-$ are qualitatively distinct from those of the positive range $(m_{\tau\tau}^2)^+$

$$\left(m_{\tau\tau}^2\right)^+ \neq \left| \left(m_{\tau\tau}^2\right)^- \right|. \tag{4.8}$$

A naïve square root does not capture this feature. Negative values of $m_{\tau\tau}^2$ arise when the assumption of lepton–invisible colinearity fails for the underlying process. Mathematically, this happens when either (but not both) $f_i \equiv 1 + \xi_i < 0$ with $E_{\mathrm{T}}^{\mathrm{miss}} > \left|\mathbf{p}_{\mathrm{T}}^{\ell_i}\right|$. allowing them to direct probe the electroweak structure of the underlying process, facilitating signal and background discrimination. Physically, this occurs when one of the lepton momenta

[1] An alternative way to constrain $f_i \equiv 1 + \xi_i$ is by assuming the tau momenta balance the hadronic recoil as CMS [33] do: $-\mathbf{p}_{\mathrm{T}}^{\mathrm{hadronic}} = f_1 \mathbf{p}_{\mathrm{T}}^{\ell_1} + f_2 \mathbf{p}_{\mathrm{T}}^{\ell_2}$, where $\mathbf{p}_{\mathrm{T}}^{\mathrm{hadronic}}$ is the transverse projection of the vectorial sum of the jet momenta.

is smaller in magnitude and points in the opposite hemisphere to the missing transverse momentum $\mathbf{p}_{\mathrm{T}}^{\mathrm{miss}}$ (or equivalently, the same hemisphere as the hadronic activity $\mathbf{p}_{\mathrm{hadronic}}$). Therefore, this lepton's momentum must be inverted in direction when rescaling to obtain an estimate of the tau momentum that balances the hadronic recoil. This happens rarely for highly boosted leptonic $Z \to \tau\tau$ decays when lepton–invisible colinearity largely holds. By contrast, this occurs with greater frequency when the leptons and missing transverse momenta originate from less boosted heavy parent particles, such as the WW background or $\tilde{\ell}\tilde{\ell}$ signal where the leptons can decay nearly back-to-back. In these cases, $m_{\tau\tau}^2$ is merely interpreted as a variable that can discriminate against leptons originating from $Z \to \tau\tau$.

To construct a variable with mass dimension 1 while properly capturing the information encoded across the full range of $m_{\tau\tau}^2 \in [-\infty, \infty]$, the signed square root is a natural operation

$$m_{\tau\tau}\left(p_{\ell_1}, p_{\ell_2}, \mathbf{p}_{\mathrm{T}}^{\mathrm{miss}}\right) = \begin{cases} \sqrt{m_{\tau\tau}^2} & m_{\tau\tau}^2 \geq 0, \\ -\sqrt{|m_{\tau\tau}^2|} & m_{\tau\tau}^2 < 0. \end{cases} \tag{4.9}$$

This prescription maintains a one-to-one map to $m_{\tau\tau}^2$ and its distinct behaviour at negative values, despite introducing a discontinuity at $m_{\tau\tau} = 0$ GeV. Equation (4.9) defines the $m_{\tau\tau}$ variable used in this analysis.

4.3.3 VBF Specific

The following variables refer explicitly to candidate VBF events. These variables probe both the electroweak structure of the underlying event as well as the production mechanism, further facilitating signal and background discrimination and enhancing the VBF signal above the direct production. The invariant mass reconstructed between two jets, the m_{jj}, is a key discriminating feature of VBF events. This is formed by these jets which share a large rapidity difference, and thus have a large observed mass. We calculate m_{jj} by considering all signal jets (central and forward) in the event with $\eta < 4.5$ and $p_{\mathrm{T}} > 30$ GeV, and selecting the pair which form the highest invariant mass.

Writing the four-vector for the i-th jet as:

$$p_i^{\mu} = (p_{\mathrm{T}i}, \eta_i, \phi_i, m_i) \tag{4.10}$$

In the limit of massless jets, $E_T = p_{\mathrm{T}}$, and m_{jj} is taken as the maximum invariant mass between any two jets, indexed by i and k:

$$m_{jj}^2 = \max(2E_{T_i}E_{T_k}(\cosh(\eta_i - \eta_k) - \cos(\phi_i - \phi_k))) \tag{4.11}$$

This algorithmic approach generalizes to VBF topologies with energetic decay jets, and reduces to the leading and sub-leading p_{T} method commonly deployed in analyses with exactly two jets in the event.

The leading VBF-tag jet, j_1, is defined as the higher p_{T} jet of the two that form the highest m_{jj}, while the sub-leading VBF-tag jet j_2, is defined as the lower p_{T} jet of the two that form the highest m_{jj}.

The third jet, j_3, in events with greater than two jets, is called a *spectator jet*. This must satisfy $p_{\mathrm{T}} > 20$ GeV, $|\eta| < 2.8$, $\Delta R_{j_1} > 2.0$, and $\Delta R_{j_2} > 1.0$. One benefit of the VBF process is the cleaner hadronic signature, with a rapidity gap between the two tag jets. Not only should this help suppress the rate at which hadronic activity (jets or soft pions) are reconstructed as leptons, but it can also open a window to isolate a jet from $W \to qq$ process. Shown in Figure 21 is the truth-level counts of a 3$^{\mathrm{rd}}$ jet in the event.

These cuts are designed to isolate these candidate decay jets from the $\widetilde{\chi}_1^{\pm}$ in the case that the highly off-shell W resolves into a single $R = 0.4$ jet. Analysis of the location of leptons in signal events reveal a tendency to concentrate far from either of the two tag jets. Final state radiation (FSR) from outgoing partons is concentrated near the tag jet's momentum axis. These results, and the motivation for this criteria, is summarized in Fig. 20.

4.3.4 Recursive Jigsaw Variables with VBF-assisted signals

The search for compressed signals is experimentally difficult because of the soft final state decay products and little missing energy. At the same time, the $\widetilde{\chi}_1^0$ (the undetectable part of the overall three body decay process) also has soft momentum in the mother rest frame. In VBF induced events, the di-$\widetilde{\chi}_1^0$ system gains nearly all its p_T by recoiling against the di-jet system. In a zeroth order approximation, the correlation between $E_{\mathrm{T}}^{\mathrm{miss}}$ and hadronic thrust is proportional to the ratio of the $\widetilde{\chi}_1^0$ and $\widetilde{\chi}_1^{\pm}$masses. As a general consideration, the

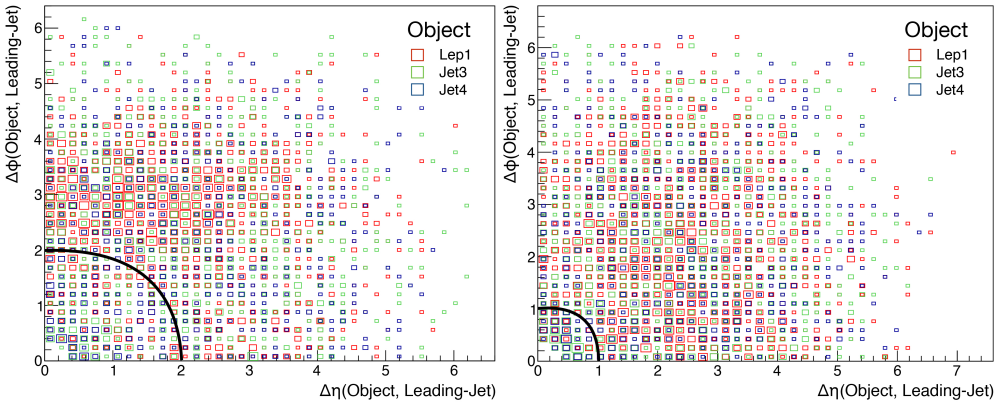

Figure 20: 2D histogram showing the distribution of the leading lepton ℓ_1, and the leading two auxiliary jets, j_3 and j_4, in $(\Delta\eta, \Delta\phi)$ space with respect to the leading tag jet (left) and the sub-leading tag jet (right). The black line represent a cone about the leading and sub-leading tag-jets, outside of which candidate 3$^{\text{rd}}$ jet candidates are considered.

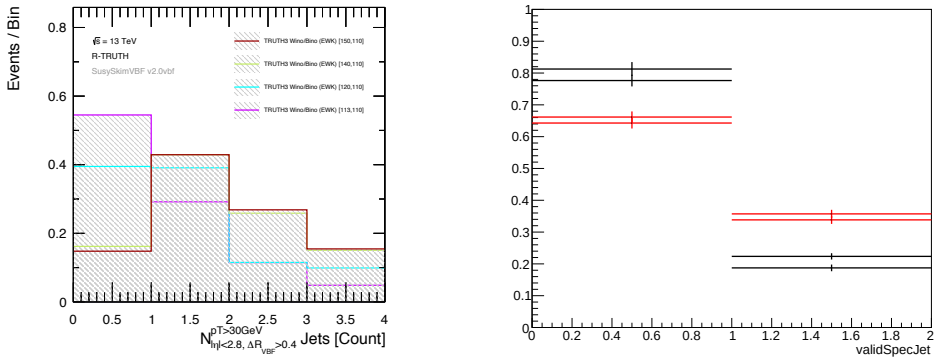

Figure 21: Counts of a 3-rd jet (left) at truth-level for processes with different mass-splittings. As the mass-splitting increases, so does the propensity for more jets to appear in the event. Count of an identified spectator jet according to the jet criteria in fully reconstructed data for the Higgsino model with $\Delta M = 40$ GeV. In black are final-states with no $W^* \to qq$ process, while in red are the final states with a $W^* \to qq$ decay. The criteria isolate this 3-rd jet as a decay-jet with about 50% purity.

transverse thrust axis in VBF-assisted events imposes great momentum flow into the SUSY system, providing a strong compressed signal by way of discriminating variables derived from this VBF-like RJR scheme.

This feature can be further exploited using the Recursive Jigsaw Reconstruction (RJR) developed by and described in Ref. [34]. The principle of this algorithm is to derive the best guess for unknown degrees of freedom using information from visible objects in an event. The globally unknown degrees of freedom are the initial longitudinal momentum and the rapidity of the $E_{\mathrm{T}}^{\mathrm{miss}}$. We assume that combinatoric ambiguities are not present, i.e. that the tag-jets recoil off the parent SUSY system and any other jets or leptons in the event come from the decay processes or are part of initial state radiation. Two hemispheres are

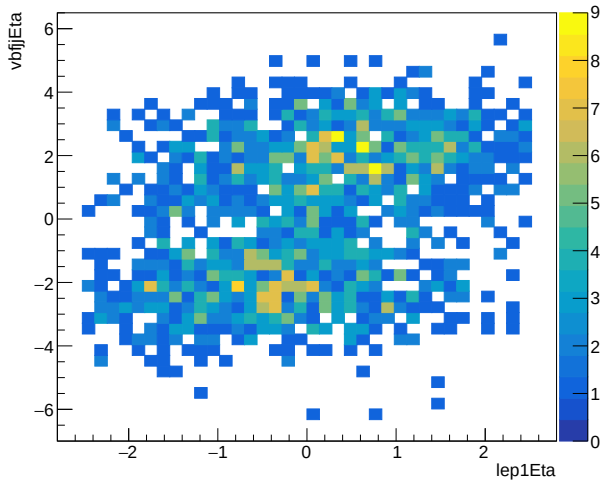

Figure 22: Subtle correlations between the di-jet axis and SUSY axis in η space.

defined: a VBF hemisphere with the two tag-jets and a SUSY hemisphere with the decay products.

Shown in Fig. 22 is the correlation between the leading lepton rapidity and the rapidity of the di-jet system. The slight positive correlation indicates that the longitudinal boost of the tag-jets indicates some equivalent boost to the lepton. Considering the leading decay lepton as a proxy for the mother particle's longitudinal momentum, one can also infer that in signal events the rapidity of the $E_{\mathrm{T}}^{\mathrm{miss}}$ is also loosely correlated with the di-jet rapidity. We

implement this finding using the RJR framework by setting the $E_{\mathrm{T}}^{\mathrm{miss}}$ rapidity to the visible decay particles' rapidity in the lab frame. This initial guess will not change the minimization procedure to determine the lab boost, β_z^{lab} In the RJR framework, the definition of the lab frame is longitudinally boost invariant, in that we will always arrive at the same lab, z irrespective of the visible particle's momentum along the beam axis. This guarentees that any observable associated with reference frames attached to the lab frame in the decay tree inherit this invariance property [34].

The VBF specific decay tree is shown in Fig. 23. With the decay tree kinematics fully

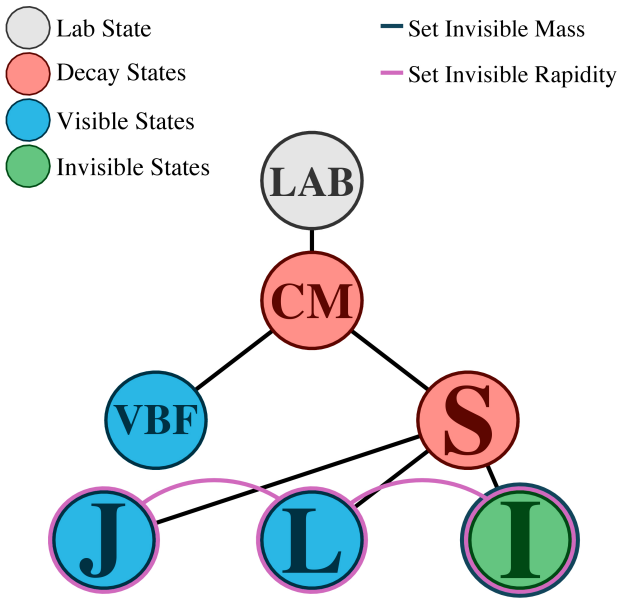

Figure 23: Decay tree corresponding to the VBF-assisted $E_{\mathrm{T}}^{\mathrm{miss}}$ strategy.

specified and all objects combinatorically assigned to a single group, we can then extract useful information and observables for use in event analysis. A principle of these VBF-assisted signals is that in the limit of $m_{\tilde{\chi}_1^\pm} - m_{\tilde{\chi}_1^0} \approx 0$, we expect the ratio of the $E_{\mathrm{T}}^{\mathrm{miss}}$ to p_T^{ISR} to be equal to the ratio of LSP and NLSP masses.

Using information from the VBF-assisted RJR decay tree, this variable relates the VBF thrust axis and the reconstructed invisible axis. The characteristic compressed distribution is obtained and is robust with increasing m_{jj}, as shown in Fig. 24. The major irreducible backgrounds, however, tend towards low R_{VBF} at high m_{jj}, as shown in Fig. 25. This

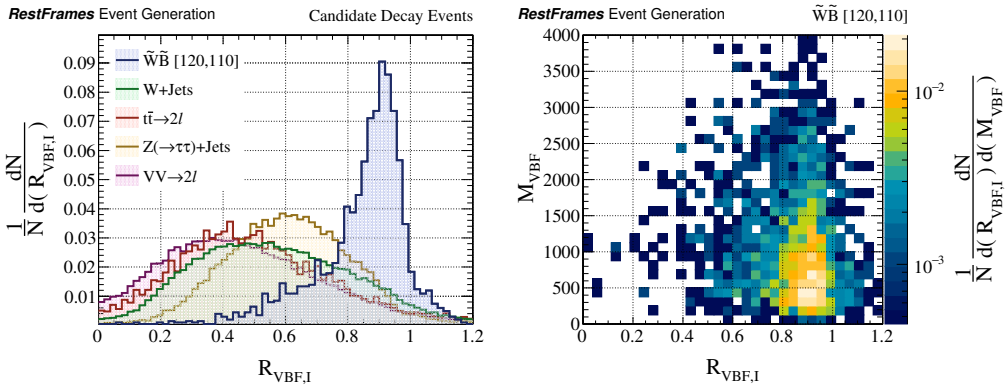

Figure 24: Distribution of R_{VBF} for signal and background processes (left) and the shape of R_{VBF} with respect to m_{jj} for the signal process (right)

inspires binning in $|\Delta\eta(j_1, j_2)|$, as m_{jj} as highly correlated to this variable. There is also a relationship between R_{VBF} and $m_{\ell\ell}$, also shown in Fig. 28.

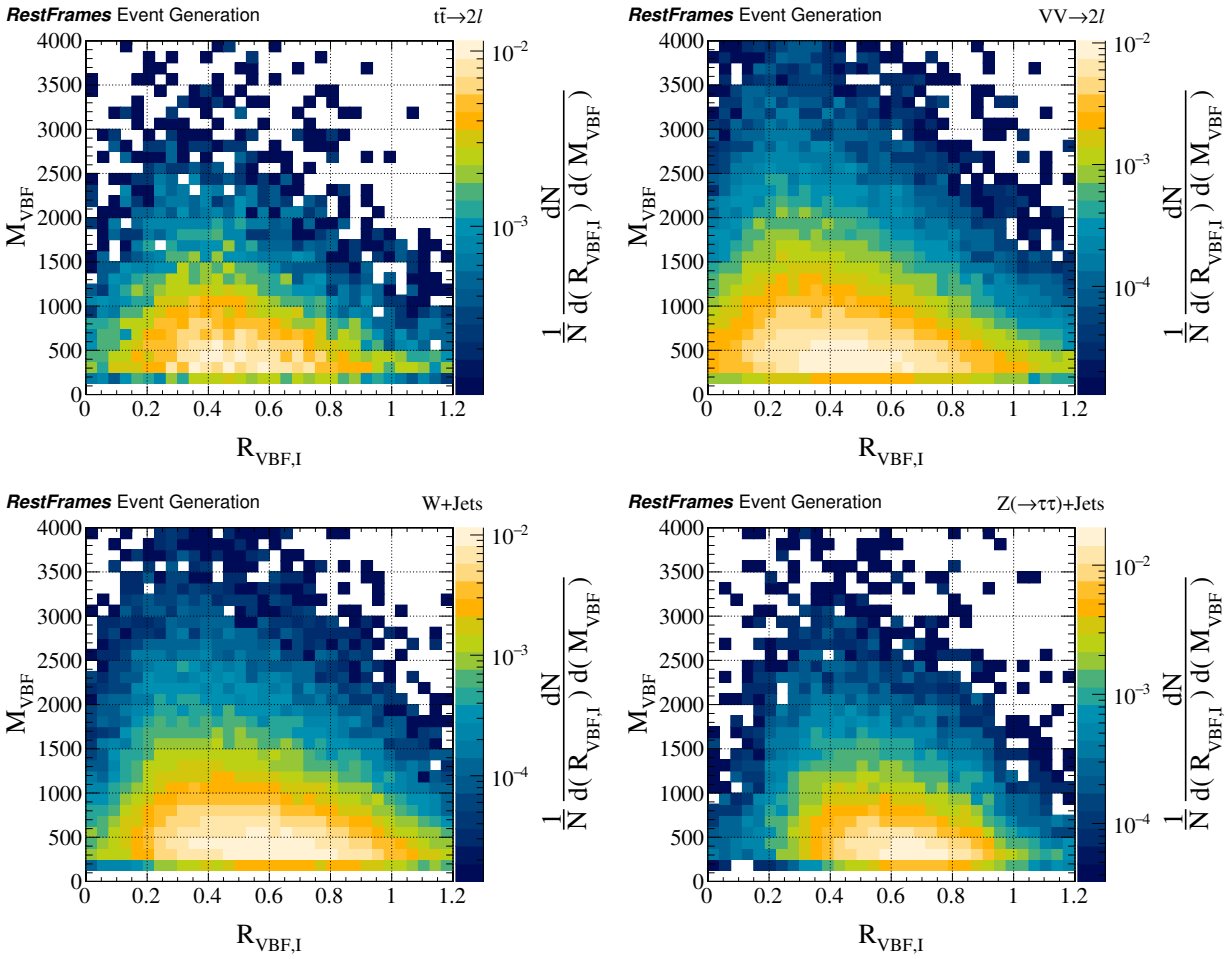

Figure 25: Distribution of R_{VBF} for major background processes.

5.0 Analysis

5.1 Event Selection and Signal Regions

Defining selections for VBF regions in this region of phase space had proven different than existing analyses which use the VBF topology. For large number of expected signal and background events, attempting to minimize the ratio S/B is most important, as in the limit of large numbers of events, the systematic errors dominate over the statistical error.

In this topology, the base-line number of signal events is already rather limited. Background suppression and eventual estimation is accomplished by consideration of a number of key discriminating variables. The goals of these selections are to isolate the *Top* and *Tau* backgrounds, which is primarily accomplished though the number of ID b-Jets and the $m_{\tau\tau}$. Additional cuts on $m_{\mathrm{T}}^{\ell_1}$ and the R_{VBF} helps to remove backgrounds with W boson production in association with jets and those with W boson pair production. Pre-selection plots showing the discriminating power of these variables as well as proper modeling is shown in Fig. 29.

Optimization was in-part carried out using a test of significance which returns the expected p-value for zero signal yield in a ratio of Poisson means. This, in essence, performs an measurement based on two expectations, a main measurement that might have signal and an auxiliary measurement for the background that is signal free. The use of the incomplete beta function to find the prior probability, whereas the ratio provides an effective CL_s value, representing the confidence in accepting the null hypothesis.

In some instances, multivariate techniques were used. This technique has the useful advantage of optimizing a set of cuts, especially when it isn't clear what cut scheme is optimal. The TMVA toolkit, which organizes the simultaneous training, testing, and performance evaluation of multivariate algorithms [35]. Specifically, rectangular cut optimization was deployed to extra low-MET events using the RJR variables.

Coarse binning in $|\Delta\eta(j_1, j_2)|$ into a low and high region allow for greater yield extraction while maintaining specificity to the particular VBF signature. The complete SR definitions, containing 14 regions, is described in Table 2. Additionally, a sliding cut was implemented

in terms of $m_{\ell\ell}$ and RVBF, motivated by the contents of Fig. 28.

An aggressive $E_{\mathrm{T}}^{\mathrm{miss}}$ cut extracts SUSY signals in general, due to the expected energy carried away by the massive invisible particles predicted by the theory. However, the R_{VBF} cut described in section 4.3 creates the opportunity to extract lower $E_{\mathrm{T}}^{\mathrm{miss}}$ signals while maintaining good background rejection. The genetic algorithm outperforms both the basic minimization and simulated annealing methods. The outcome of the multivariate optimization technique returned cuts approximately those determined by the $N-1$ technique.

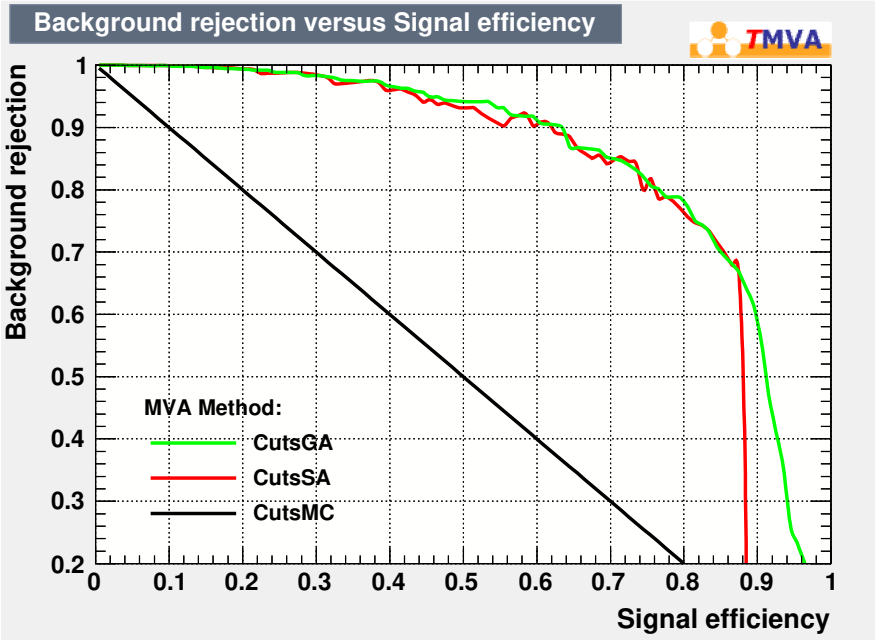

Figure 26: Receiver operating characteristic (ROC) curve for the major VBF specific variables, showing good signal and background separation.

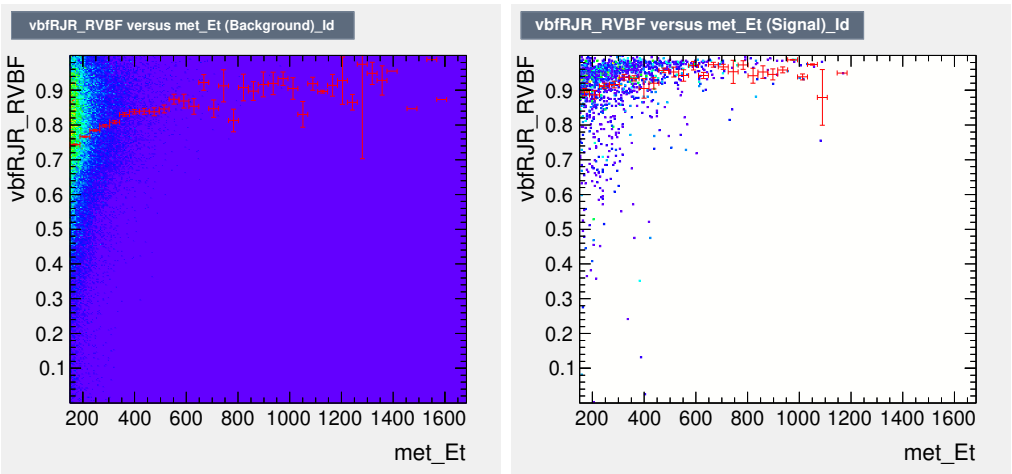

Figure 27: Correlation plots for background (left) and signal (right).

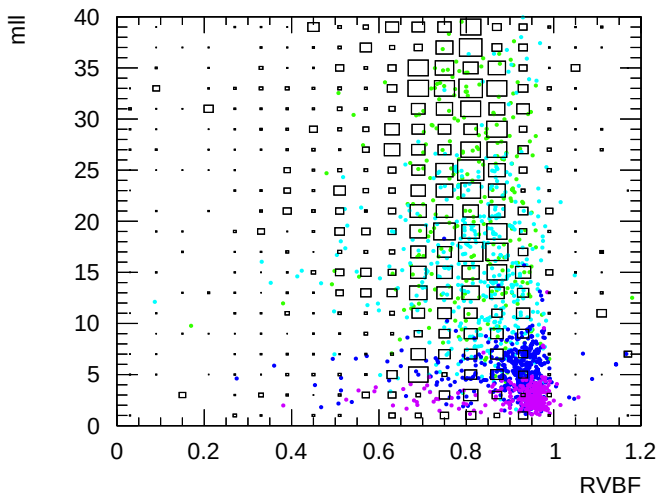

Figure 28: Distribution of R_{VBF} and $m_{\ell\ell}$ for background (black boxes) and various signal processes (colored dots).

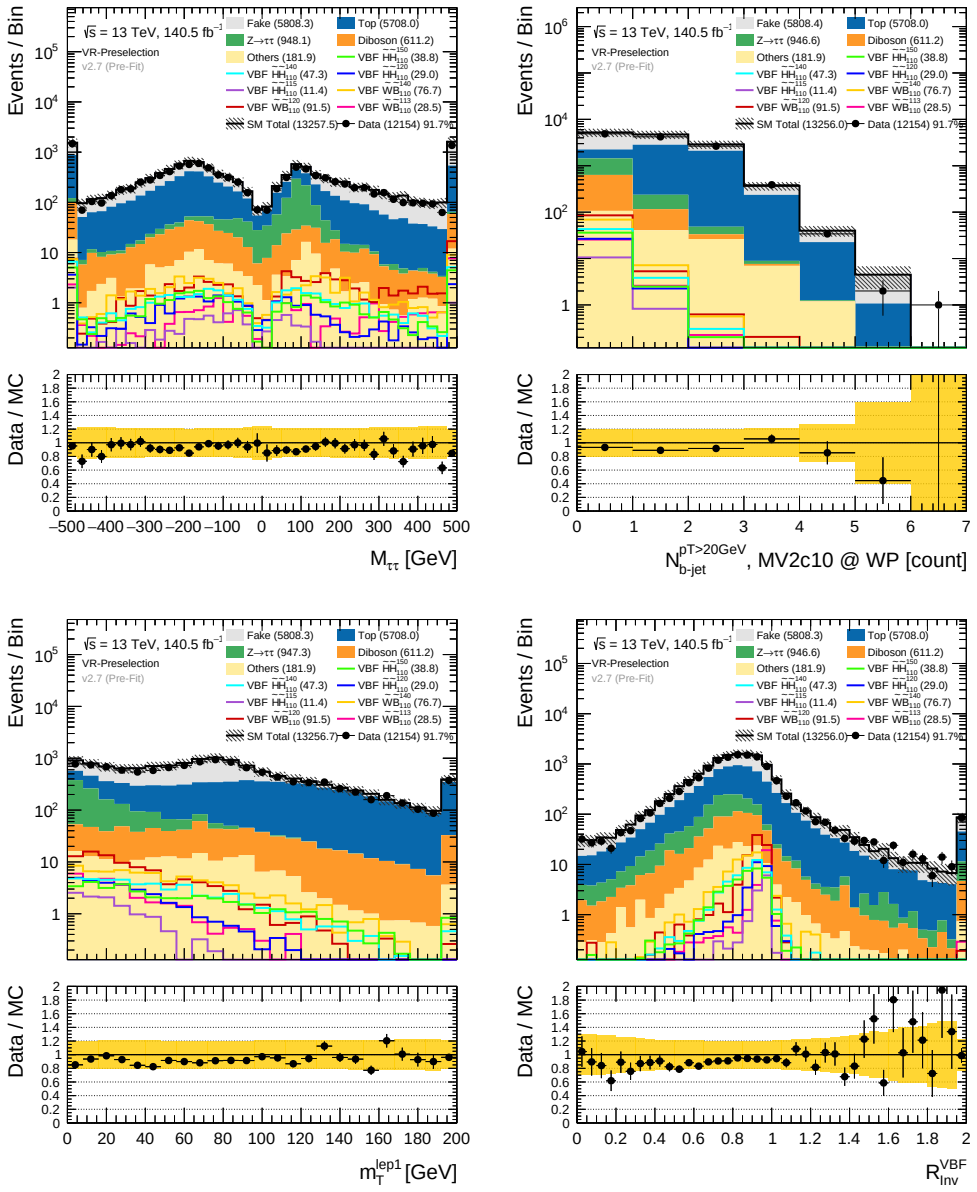

Figure 29: Preselection distributions comparing data (black points) and Monte Carlo simulation (colored histograms) for a couple of key discriminating variables.

Variable	Selection criteria defining the VBF SR (Electroweakino)						
$\lvert\Delta\phi(j_1, \mathbf{p}_{\mathrm{T}}^{\mathrm{miss}})\rvert$	$--$						
Leading jet $p_{\mathrm{T}}(j_1)$	> 100 GeV						
Sub-leading jet $p_{\mathrm{T}}(j_2)$	> 40 GeV						
$\eta_{j1}\eta_{j2}$	< 0						
$E_{\mathrm{T}}^{\mathrm{miss}}$	> 150 GeV						
m_{jj}	> 400 GeV						
$\min\lvert\Delta\phi(\text{all jets}, \mathbf{p}_{\mathrm{T}}^{\mathrm{miss}})\rvert$	> 0.4						
$N_{\mathrm{b-jet}}^{20}$, 85% WP	Exactly zero						
N_{leptons}	Exactly two baseline and two signal						
$R_{\ell\ell}$	> 0.05						
R_{ee}	> 0.3						
Lepton charge and flavour	$e^{\pm}e^{\mp}$ or $\mu^{\pm}\mu^{\mp}$						
Electron (muon) $p_{\mathrm{T}}(\ell_1)$	$> 4.5(3.0)$ GeV						
Electron (muon) $p_{\mathrm{T}}(\ell_2)$	$> f(m_{\ell\ell}) = \min(10, 2 + m_{\ell\ell}/3)$ GeV						
$m_{\tau\tau}$	Veto [0, 160] GeV						
R_{VBF}	$> f(m_{\ell\ell}) = \max(0.6, 0.92 - m_{\ell\ell}/60)$						
$m_{\mathrm{T}}^{\ell_1}$	< 60 GeV						
$E_{\mathrm{T}}^{\mathrm{miss}}/H_{\mathrm{T}}^{\mathrm{lep}}$	> 2						
SRSF- Bins	eMLLa	eMLLb	eMLLc	eMLLd	eMLLe	eMLLf	eMLLg
$m_{\ell\ell}$ [GeV]	$[1, 2]$	$[2, 3]$	$[3, 5]$	$[5, 10]$	$[10, 20]$	$[20, 30]$	$[30, 40]$
Inclusive SR Bins	iMLLa	iMLLb	iMLLc	iMLLd	iMLLe	iMLLf	iMLLg
$m_{\ell\ell}$ [GeV]	< 2	< 3	< 5	< 10	< 20	< 30	< 40
VBF SR Bins	VBFa	VBFb	VBFi				
$\lvert\Delta\eta(j_1, j_2)\rvert$	$[2, 4]$	$[4, 9]$	$[2, 9]$				

Table 2: Signal region selections optimized for the VBF-like topology. Binning is implemented in $m_{\ell\ell}$ as well as $|\Delta\eta(j_1, j_2)|$. It was found that the composition and shape of the signal regions depended on $|\Delta\eta(j_1, j_2)|$, and this fact is exploited to set a more stringent upper limit.

5.2 Background Estimation

There are a number of Standard Model processes with general hadronic activity (jets), leptons, and missing transverse momentum. While we impose strict signal regions cuts, these background processes can still enter the signal region. A table of these backgrounds, and the instrumental or irreducible reasons for which they enter the signal region, is shown in Table 3. The 'irreducible' backgrounds (called such because at a certain limit the gain from

Process	Comment	Major Irreducible Reason for entering SR
$t\bar{t} \to 2\ell$	Fully Leptonic	Both b-Jets fail identification
$tW \to 2\ell$	Fully Leptonic	b-Jet fails identification
$Z \to \tau\tau$	Leptonic tau decay	$E_{\mathrm{T}}^{\mathrm{miss}}$ from neutrinos, jets from QCD radiation
$VV \to 4\ell$	The ZZ process	Miss two leptons (fail, out of acceptance)
$VV \to 3\ell$	The WZ process	Miss one lepton (fail, out of acceptance)
$VV \to 2\ell$	Dominated by WW	$E_{\mathrm{T}}^{\mathrm{miss}}$ from neutrinos, boosted W's
$h \to WW$	ggF and VBF	VBF-jets topology
VVV	Rare process	$E_{\mathrm{T}}^{\mathrm{miss}}$, jets, and genuine leptons
$Z^*/\gamma^* \to 2\ell$	Low-mass DY	Low $m_{\ell\ell}$ due to off-shell effects
$J\psi \to 2\ell$	Resonance	Low $m_{\ell\ell}$ resonance, jets from QCD
Process	Comment	Instrumental reason for entering SR
$t\bar{t} \to 1\ell$	Semi Leptonic	Both b-Jets fail identification, one fake lepton
$Z \to 2\ell$	Z-mass peak	$E_{\mathrm{T}}^{\mathrm{miss}}$ from mis-measured jet
$VV \to 1\ell$	Semi-leptonic	One fake lepton
$VV \to 0\ell$	Fully hadronic	Two fake leptons
$W \to 1\ell$	One isolated lepton	One fake lepton

Table 3: Major backgrounds to be considered for the VBF regions.

further reducing these backgrounds is offset by lose of signal) are reduced using kinematic variables and estimated in a semi-data driven way, with the simulation extrapolated from a set of control and validation regions. An overall normalization for the processes corresponding to top quark production ($t\bar{t}$, tW, and more rare top processes) are measured in a dedicated region enhanced with events of this type as compared to data. A normalization is also attached to the $Z \to \tau\tau$ process and measured is a different dedicated region. These are implemented automatically in the fit since regions rich in these processes would provide the best constraint on the normalization parameter.

Together, these two backgrounds account for 50% of the total background contribution. Both stellar modeling and overall unit normalization factors provide important confirmation that the estimates as a result of the modeling in the signal region is valid. The remaining major irreducible background is the diboson and higgs processes. No normalization of these is attempted; instead, modeling and robustness of the simulation is checked in validation regions which very closely mirror the signal region.

5.2.1 Description of the Fake Factor Method

The fake factor described a data-driven method to estimate backgrounds which enter the signal region due to one of the lepton passing lepton identification and isolation when it is either not a genuine lepton or not prompt. While the reconstruction and sophisticated detector instrumentation, such as described in section (trt section) is designed to reject, the high flux of hadronic activity, with charged particles that can mimic electrons or produce somewhat energetic calorimeter deposits which don't pass jet identification constitute a large base rate. For example, the W+jet cross-section is approximately 200 pb [36]. So while the "fake-rate" is small (target rejection of 10^5, [37]) the observed number of fake events can still be large.

It is important to measure this type of background from data as the rate of mis-identification may not be accurately modeled in the simulation. Jet and non-prompt leptons being identified as genuine leptons is a complex process dependent on physical details and interactions outside the current scope of simulation. One source of fake leptons is a low p_{T} jet, of which the effect of the p_{T} spectrum of gluons and quarks, which then hadronize into charged particles, can only be understood through data and analysis of detector performance [38]. Additionally, real muons can radiate a photon through interactions with the calorimeter material. This photon would show up as a near-by energy deposit in the EM calorimeter, with a track in the MS which cannot be matched to the mother track in the ID – this is a fascinating case of physical interactions with all three detector subsystems by one lepton gives rise to a fake lepton. In this case, fake rates are highly sensitive to low p_{T} behavior and to the emission spectra and probability of photons by muons. Nearly all 'fake' muon

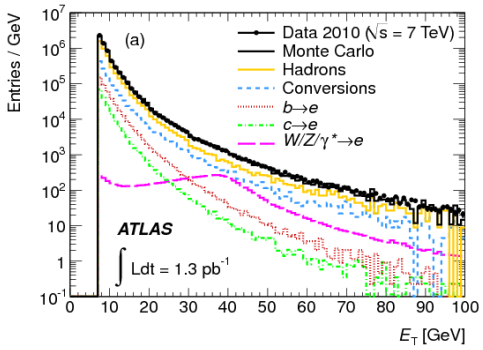

Figure 30: Composition of Electron fakes

candidates come from non-prompt processes [39], arises predominately from heavy flavor decays which do produce real muons and in-flight decays of mesons, namely the pion.

In the fake factor method, two sets of lepton identification criteria are used. These include the standard signal lepton identification used by the analysis (referred to as *tight* or "ID"), as well as an orthogonal criteria (referred to as *loose* or "anti-ID"). The anti-ID criteria is designed to be enriched in fake leptons, by relaxing or inverting the various lepton identification and isolation variables. The fake factor (F) is defined as the ratio between the number of ID leptons and the number of anti-ID leptons as measured in a kinematic region primarily consisting of fake leptons with a similar composition as the reducible background in the signal region. This fake factor is typically binned in p_{T}, though can be binned in terms of any kinematic variable, and can be expressed formally s:

$$F(i) = \frac{N_{\mathrm{ID}}(i)}{N_{\text{anti-ID}}(i)}, \tag{5.1}$$

where N is the number of events, and i refers to the i^{th} p_{T} bin.

Once the fake factor has been measured in this fake lepton-enriched region, it can then be used to obtain the reducible background estimate in the signal region. To do so, an anti-ID control region is used which is identical to the signal region except that one of the ID leptons is replaced with an anti-ID lepton. This control region is then multiplied by the fake factor on an event-by-event basis, and thus to first order, the total reducible background in the

signal region is

$$N_{\text{red}}^{\text{SR}} = \sum_i N_{\text{anti-ID CR}}^i \cdot F(i), \tag{5.2}$$

where i again refers to the i^{th} p_{T} bin.

As the reducible background which the fake factor is attempting to measure is not the only process which might contain an anti-ID lepton, contributions from these other processes must be removed from Equations 5.1 and 5.2. These primarily come from prompt leptons which failed one of the signal lepton criteria, and thus can be removed by using the MC.

So far, we've only discussed the simplified case, where there is at most one anti-ID lepton in a given event. In general, however, processes with multiple fake leptons can enter the signal region, and thus events with multiple anti-ID leptons also play a role. For our two lepton final state, if events with two fake leptons are entering the signal region (which has two signal leptons in it), then that means the events with one ID lepton and one anti-ID lepton will also have some contribution from processes with two fake leptons. Ultimately, the estimate of the reducible background due to fake leptons is:

$$N_{TT} - N_{TT}^{RR} = \left[N_{LT} - N_{LT}^{RR}\right] F_1 + \left[N_{TL} - N_{TL}^{RR}\right] F_2 - \left[N_{LL} - N_{LL}^{RR}\right] F_1 F_2 \tag{5.3}$$

where F_1 and F_2 refer to the fake factor associated to the leading or subleading lepton, respectively, and the superscript "RR" refers to the events with two real leptons, which can be subtracted off using the MC.

Note that the term for events with two anti-ID leptons has a negative sign in Equation 5.3, while the terms for events with one anti-ID lepton have positive signs. This is because fake leptons can satisfy the ID criteria, which means both N_{LT} and N_{TL} can contain events with two fake leptons. Thus, the term containing N_{LL} for events with two anti-ID leptons must be used to subtract off the double counting of events with two fake leptons.

More information including the mathematical formalism used to derive Equation 5.3 and further information on the fake factor method in general can be found in [40].

Figure 31 shows a schematic of the fake factor method.

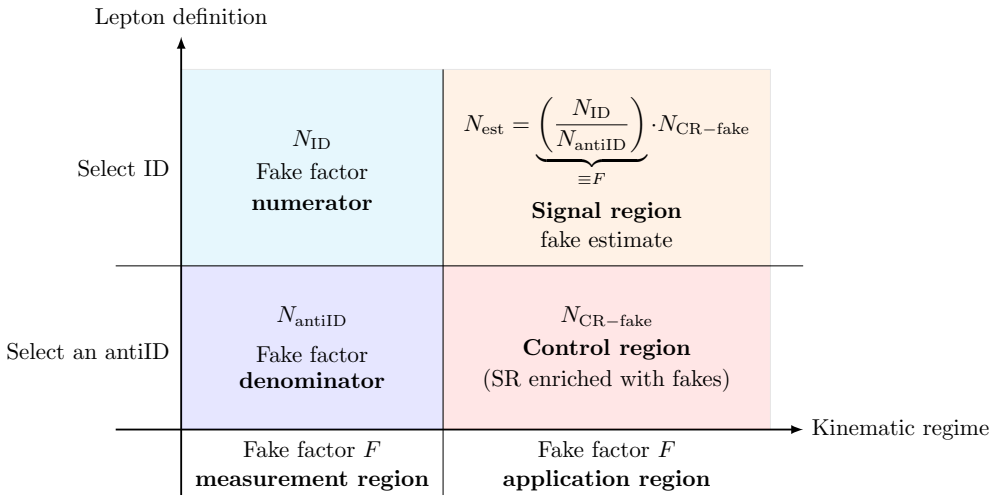

Figure 31: Schematic illustrating the fake factor method to estimate the fake lepton contribution in the signal region.

5.2.2 Implementation and Derivation of the Fake Factors

The primary reducible background which must be addressed in this analysis is the $(W \to \ell\nu)$ + jets process, which has one real, prompt lepton, while a jet fakes the second lepton.

Since a fake factor measurement region targeting the $(W \to \ell\nu)$ + jets process would not be very pure in $(W \to \ell\nu)$ + jets due to the similar topology of backgrounds such as $t\bar{t}$, a dijet selection is instead used for measuring the fake factors. There may be composition differences between the dijet process in the fake factor measurement region and the $(W \to \ell\nu)$ + jets in the signal region, in which case these differences should be used as part of the systematic uncertainty. Studies of the composition are shown ahead.

Due to the large dijet cross-section, the majority of events which fire the low p_{T} electron and muon single lepton supporting triggers tend to be from dijet events. These events are thus used to construct the fake factor measurement region. The list of single lepton supporting triggers used for each year of data taking are shown in Table 4.

The anti-ID definitions used for electrons and muons in this search are summarized in Table 5. In addition to the object-level requirements used for ID and anti-ID leptons, the

2015 and 2016	2017	2018
HLT_e5_lhvloose	HLT_e5_lhvloose_nod0	HLT_e5_lhvloose_nod0
HLT_e10_lhvloose_L1EM7	HLT_e12_lhvloose_nod0_L1EM10VH	HLT_e10_lhvloose_nod0_L1EM7
HLT_e15_lhvloose_L1EM13VH	HLT_e17_lhvloose_nod0	HLT_e15_lhvloose_nod0_L1EM7
HLT_e20_lhvloose	HLT_e20_lhvloose_nod0	HLT_e20_lhvloose_nod0
HLT_mu4	HLT_mu4	HLT_mu4
HLT_mu10	HLT_mu10_idperf	HLT_mu10_idperf
HLT_mu14	HLT_mu14	HLT_mu14
HLT_mu18		

Table 4: Prescaled single-lepton triggers used to compute the lepton fake factors.

leading jet in events used to compute the fake factors is required to have $p_{\mathrm{T}} > 100$ GeV, to make the fake factor measurement region more similar to the signal region.

Finally, fake factors for both electron and muons are binned in both p_{T} and the number of b-tagged jets in the event. For the latter, the binning is based on the event containing zero or ≥ 1 b-tagged jets. The bin with exactly zero b-tagged jets is used to estimate the fake contribution in the signal region, and the bin with one or more b-tagged jets is used to estimate the fake contribution in the $t\bar{t}$ control region.

Anti-ID Electrons	Anti-ID Muons
$p_{\mathrm{T}} > 4.5$ GeV $\lvert\eta\rvert < 2.47$ $\lvert z_0 \sin\theta\rvert < 0.5$ mm Pass LooseAndBLayer ID	$p_{\mathrm{T}} > 3$ GeV $\lvert\eta\rvert < 2.5$ $\lvert z_0 \sin\theta\rvert < 0.5$ mm Pass LowPt ID
(!Medium ID || $\lvert d_0/\sigma(d_0)\rvert > 5$ || !Gradient Iso) && (Medium ID || Gradient Iso)	($\lvert d_0/\sigma(d_0)\rvert > 3$ || !FCTightTrackOnly Iso) && ($\lvert d_0/\sigma(d_0)\rvert < 3$ || FCTightTrackOnly Iso)

Table 5: Summary of anti-ID lepton definitions. Anti-ID electrons are not allowed to fail the isolation and ID requirements simultaneously. Anti-ID muons are not allowed to fail the d_0 significance and isolation requirements simultaneously.

5.2.3 Control Regions

Variable	Selection criteria for the Control Regions	
$\left\lvert\Delta\phi(j_1, \mathbf{p}_{\mathrm{T}}^{\mathrm{miss}})\right\rvert$	$--$	
Leading jet $p_{\mathrm{T}}(j_1)$	> 100 GeV	
Sub-leading jet $p_{\mathrm{T}}(j_2)$	> 40 GeV	
$\eta_{j1}\eta_{j2}$	< 0	
$E_{\mathrm{T}}^{\mathrm{miss}}$	> 150 GeV	
m_{jj}	> 400 GeV	
$\lvert\Delta\eta(j_1, j_2)\rvert$	> 2.0	
$\min\left\lvert\Delta\phi(\text{all jets}, \mathbf{p}_{\mathrm{T}}^{\mathrm{miss}})\right\rvert$	> 0.4	
N_{leptons}	Exactly two baseline and two signal	
$R_{\ell\ell}$	> 0.05	
$R_{\mu e}$	> 0.2	
R_{ee}	> 0.3	
Electron (muon) $p_{\mathrm{T}}(\ell_1)$	$> 4.5(3.0)$ GeV	
R_{VBF}	> 0.6	
$E_{\mathrm{T}}^{\mathrm{miss}}/H_{\mathrm{T}}^{\mathrm{lep}}$	> 2	
Region	CR-Tau	CR-Top
$N_{\mathrm{b-jet}}^{20}$, 85% WP	$= 0$	> 1
$m_{\tau\tau}$	$[0, 120]$	Veto $[0, 160]$
$m_{\mathrm{T}}^{\ell_1}$	$-$	$-$
$E_{\mathrm{T}}^{\mathrm{miss}}/H_{\mathrm{T}}^{\mathrm{lep}}$	< 10	$-$
Sub-leading electron (muon) $p_{\mathrm{T}}(\ell_2)$	$f(m_{\ell\ell})$	$f(m_{\ell\ell})$
Lepton Pair	AFOS	AFOS

Table 6: Optimized Control and Validation Regions, for both region purity and minimal signal contamination

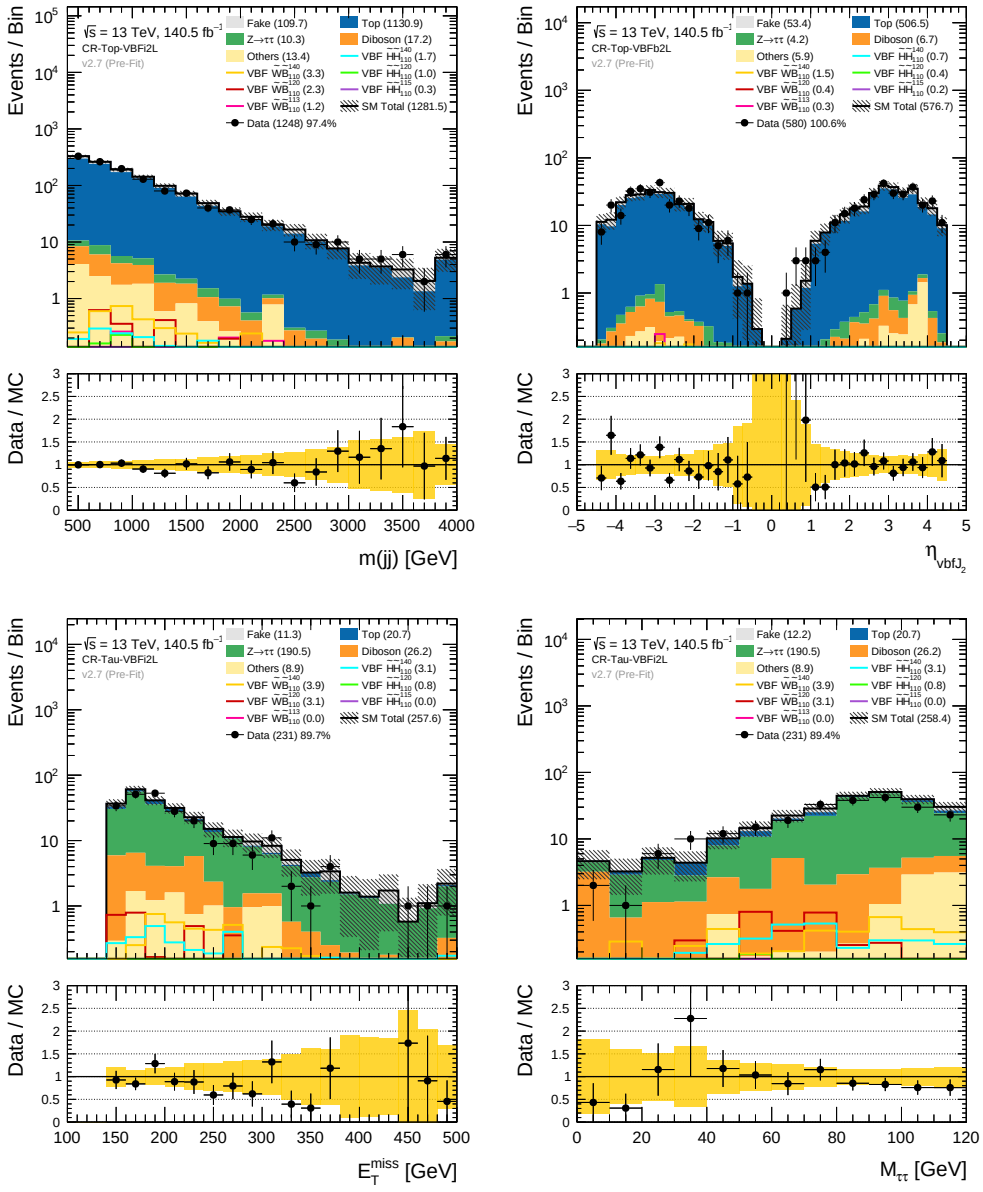

Figure 32: Agreement in the control regions. The Top background provides a pure source of forward jets, and allows for a good check of general detector simulation in the forward region. The Z background provides a pure source of boosted objects, which help check modeling of generic high $E_{\mathrm{T}}^{\mathrm{miss}}$ signals.

5.2.4 Validation Regions

The Validation regions provide a check of the data-driven method and a general check of the modeling for unnormalized backgrounds. These are shown in Table 7, and the results of the validation are shown in Figure 33.

Variable	Selection criteria for the Control Regions	
$\left\lvert\Delta\phi(j_1, \mathbf{p}_{\mathrm{T}}^{\mathrm{miss}})\right\rvert$	$--$	
Leading jet $p_{\mathrm{T}}(j_1)$	> 100 GeV	
Sub-leading jet $p_{\mathrm{T}}(j_2)$	> 40 GeV	
$\eta_{j1}\eta_{j2}$	< 0	
$E_{\mathrm{T}}^{\mathrm{miss}}$	> 150 GeV	
m_{jj}	> 400 GeV	
$\lvert\Delta\eta(j_1, j_2)\rvert$	> 2.0	
$\min\left\lvert\Delta\phi(\text{all jets}, \mathbf{p}_{\mathrm{T}}^{\mathrm{miss}})\right\rvert$	> 0.4	
N_{leptons}	Exactly two baseline and two signal	
$R_{\ell\ell}$	> 0.05	
$R_{\mu e}$	> 0.2	
R_{ee}	> 0.3	
Electron (muon) $p_{\mathrm{T}}(\ell_1)$	$> 4.5(3.0)$ GeV	
R_{VBF}	> 0.6	
$E_{\mathrm{T}}^{\mathrm{miss}}/H_{\mathrm{T}}^{\mathrm{lep}}$	> 2	
Region	VR-DF	VR-SS
$N_{\mathrm{b-jet}}^{20}$, 85% WP	$= 0$	$= 0$
$m_{\tau\tau}$	Veto $[0, 160]$	$-$
$m_{\mathrm{T}}^{\ell_1}$	< 60	$-$
$E_{\mathrm{T}}^{\mathrm{miss}}/H_{\mathrm{T}}^{\mathrm{lep}}$	> 2	> 2
Sub-leading electron (muon) $p_{\mathrm{T}}(\ell_2)$	$-$	$f(m_{\ell\ell})$
Lepton Pair	DFOS	AFSS

Table 7: Optimized Control and Validation Regions, for both region purity and minimal signal contamination

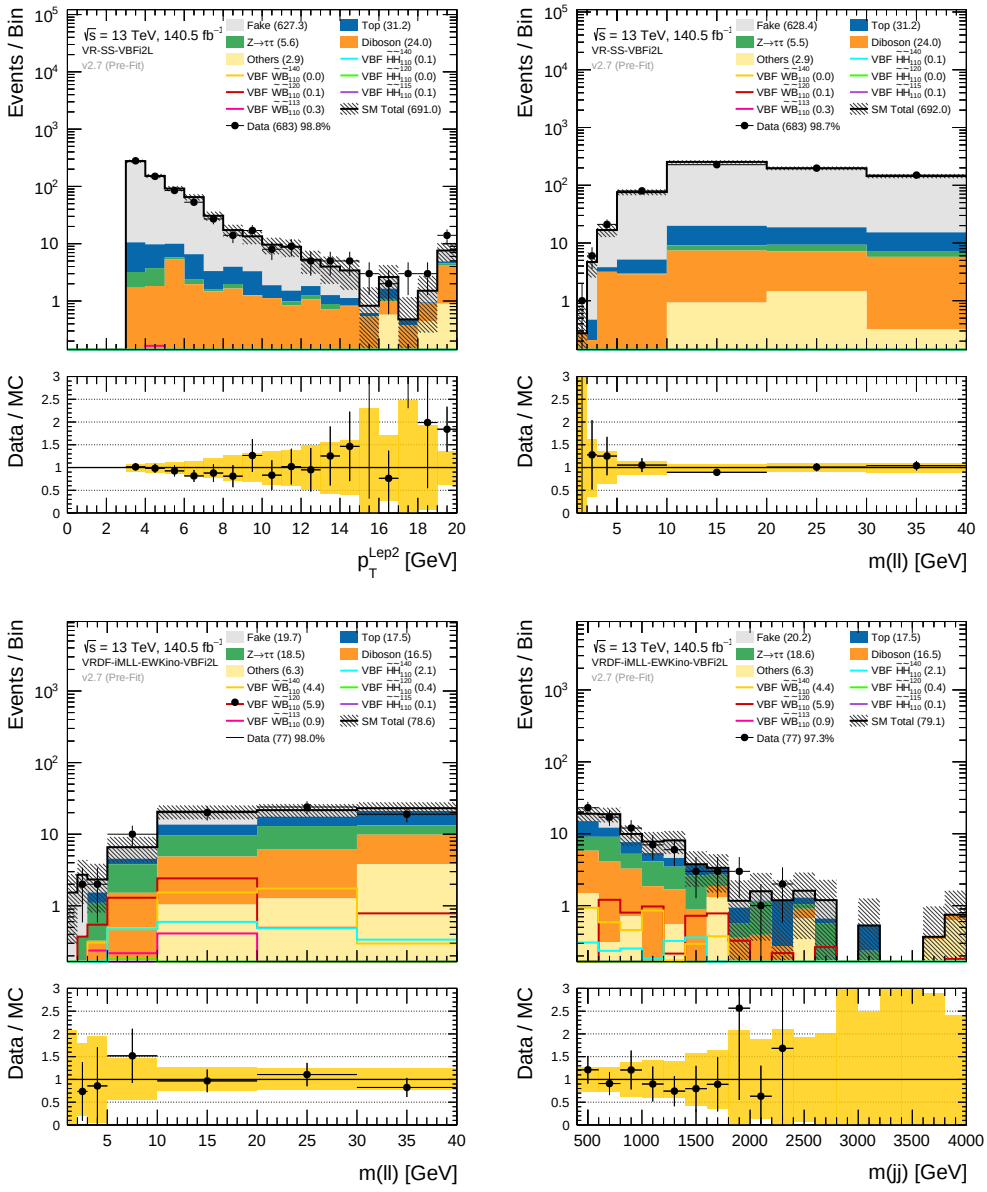

Figure 33: Validation of the fake-factor method and checking modeling of the $m_{\ell\ell}$ and m_{jj} distributions in the different flavor (DF) regions.

5.2.5 Data-driven b-Jet cross-check

The m_{jj} algorithm is inherently sensitive to jet combinatorics, and relates to b-Jet identification, as only jets which fail are considered in the m_{jj} calculation. For most of the major backgrounds, the definitions across which the transfer factors carry would introduce no clear systematic effect on the m_{jj} distribution, as the definitions mostly rely on differences in the lepton and $E_{\mathrm{T}}^{\mathrm{miss}}$ kinematics. The case of the Top background is different: for example, requiring one b-Jet requires that three total jets are in the event, two of which fail b-Jet identification. In a subset of the Top control region with two b-Jets, four total jets are required in the event, two of which fail b-Jet identification. This fact, in the high m_{jj} regime, could impact the Top extrapolation into the signal region. The way this can happen is show in Fig. 34.

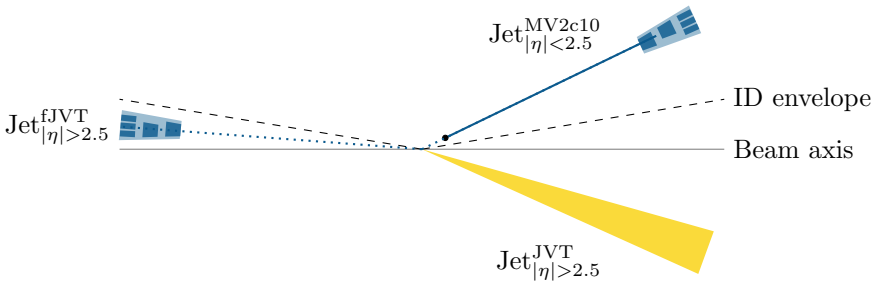

Figure 34: Schematic of how a true bottom quark jet could fail identification and thus be introduced into the m_{jj} calculation. In this case, the jet is outside the inner detector envelope, and thus manifests only as energy deposits in the forward and end-cap calorimeters. Since this jet is also forward, it would form a higher m_{jj} with another identified jet in the event.

A simple data-driven study can demonstrate the amount of correlation that the m_{jj} shape distribution has in terms of slices of $N_{\mathrm{b-jets}}$. The Top control region is sliced into bins, $N_{\mathrm{b-jets}} = 1$ and $N_{\mathrm{b-jets}} = 2$. The efficiency of these cuts with respect to the total Top region is:

$$\alpha_{\mathrm{b-jets=1}} = \frac{\text{Total Events}}{\text{Events with N}_{\mathrm{b-jets=1}}},\ \alpha_{\mathrm{b-jets=2}} = \frac{\text{Total Events}}{\text{Events with N}_{\mathrm{b-jets=2}}} \tag{5.4}$$

Data in the $N_{\text{b-jets}} = 1$ binned by variable x can then be estimated using data in the $N_{\text{b-jets}} = 2$ region by the relation:

$$N^{\text{b-jets=1}}_{\text{Estimated Events}}(x) = \frac{\alpha_{\text{b-jets=1}}}{\alpha_{\text{b-jets=2}}} \cdot N^{\text{b-jets=2}}_{\text{Data Events}}(x) \tag{5.5}$$

Equivalent forms of this check would to divide the two regions bin-wise and check for deviations from the factor $\frac{\alpha_{\text{b-jets=1}}}{\alpha_{\text{b-jets=2}}}$. Following this method shows more clearly how the shapes of the distributions change when moving a higher numbers of jets to a lower number, and thus towards the signal region into which we extrapolate. The plots in Fig. 35 demonstrate that these correlations are either marginal or non-existent. The conclusion reached is a reaffirmation that the use of a Monte Carlo simulation and a data normalized control region to estimate yields in a $N_{\text{b-jets}} = 0$ region maintains validity even at high values of m_{jj}.

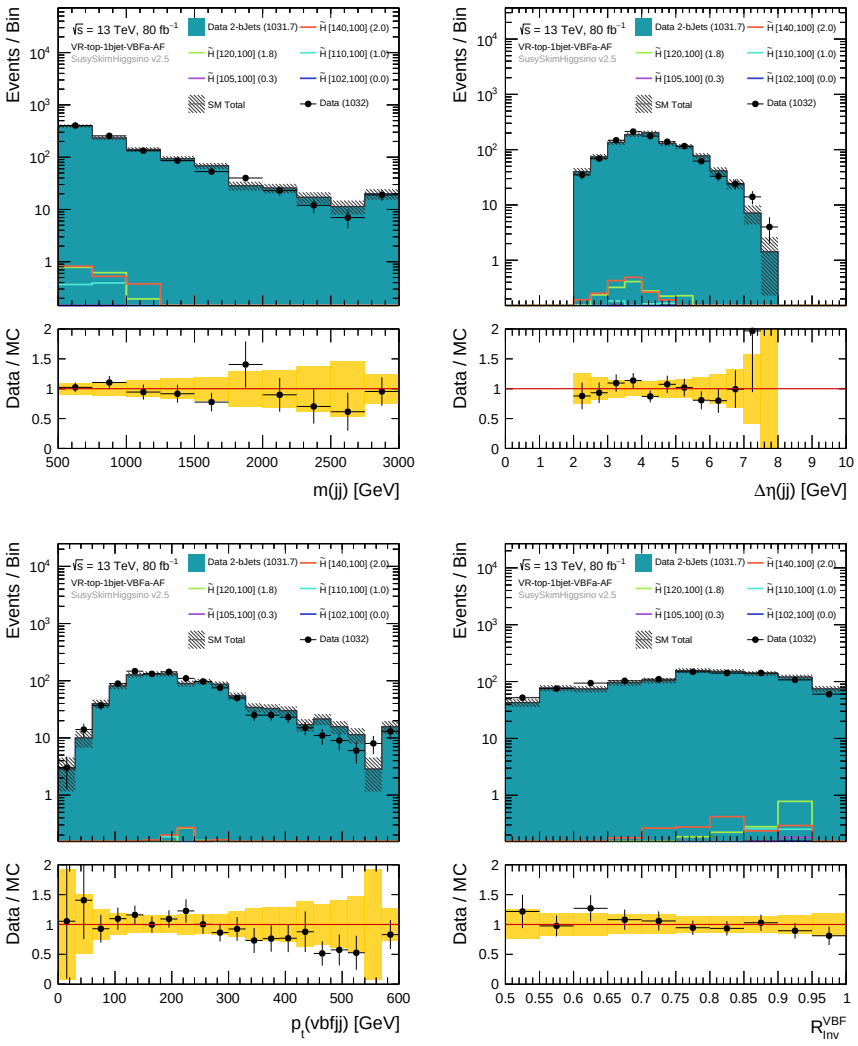

Figure 35: Observed closure of this data driven check. Closure in this context indicates the lack of correlation across $N_{\mathrm{b-jets}}$

5.3 Statistical Implementation

To move towards the goal of putting either putting an upper-limit (exclusion case) or lower-limit (discovery case) on new physics, a statistical interpretation of these limits is pursued. In a perfect world, we would know the background and signal expectations with only statistical uncertainties (a perfect experiment). The total expectation is $N = \mu_{\text{sig}} \cdot s + b$, where we introduce a new parameter, μ_{sig}, which is a measure of the signal strength. If this parameter is 0, this represents a background only hypothesis, while if it equals 1, this is the nominal signal hypothesis. Say we expect 8 background events (perfectly measured), and 4 signal events, or in total 12 events, and perform some measurement of the actual number of events. We can then represent the likelihood of making that specific measurement as a likelihood function:

$$L(N|\mu, s, b) = \text{Poisson}(N|\mu_{\text{sig}} \cdot s + b) \tag{5.6}$$

Equation 5.6 tells us a posterior probability of measuring N events given three parameters. Two of these are known, while one is floating, and is precisely the measurement we are interested in (the *parameter of interest* or POI). Maximizing this likelihood provides us with a way to measure this POI, since given some observed outcome, we'd want to provide a statistical model which has that outcome as it's maximum likelihood. In the Gaussian regime for Poisson functions, maximizing the likelihood corresponds to centering the Gaussian about the number of observed events.

An illustration of these Poisson functions for different values of μ_{sig} is shown in Fig. 36. The nominal signal hypothesis is shown in black, while the back-ground only hypothesis is shown in red, with an excess signal hypothesis in blue. Say we observe 12 events – it seems appropriate to set $\mu_{\text{sig}} = 1$ and claim new physics, since that maximizes the likelihood of observing 12 events. Someone under the (pessimistic) Bayesian influence, however, might consider the prior for new physics existing to be extremely low, and thus more willing to attribute the observed data to a statistical fluctuation (which would happen 10% of the time).

On the other hand, say 7 events were observed: this approximately maximizes the background-only likelihood, and the probability of seeing a downward fluctuation of the

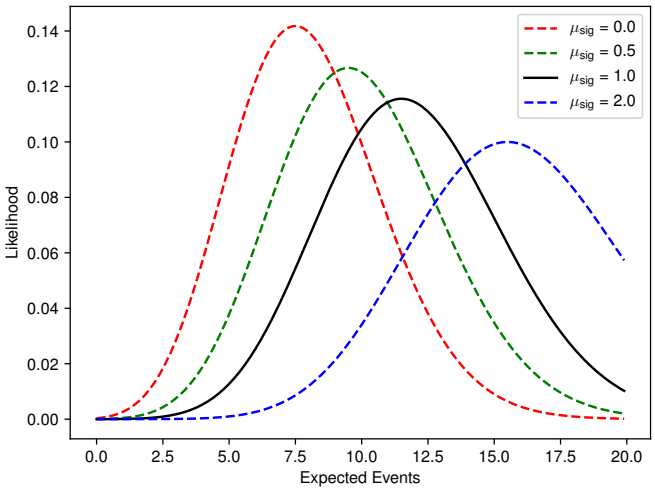

Figure 36: Various Poisson distributions given an expectation of 4 and 8 signal and background events, respectively.

signal hypothesis is about 10%, or a p-value of 0.10. Alternatively, say 4 events were observed, with a background-only p-value of 0.8 and a signal hypothesis of 0.05. What do we make of this effect? If we want to exclude new physics with 95% confidence, it seems that expected and normal fluctuations given a background-only hypothesis affects our exclusion power. This is normal, but in the limit of zero signal expectation, a 95% exclusion will be expected to happen exactly 5% of the time. This motivates the CL_s test statistic, defined to essentially penalize exclusion of the signal model by any perceived exclusion without it.

$$CL_s = \frac{CL_{s+b}}{CL_b} \tag{5.7}$$

In essence, we want to differentiate between $\mu_{\text{sig}} = 1$ as *the best way* to describe the given data verses $\mu_{\text{sig}} = 0$ as *a way* to describe the given data. Another form is the log-likelihood ratio, considered the most powerful statistic to test between two hypothesis [41]. This becomes complicated as we cannot perform perfect experiments, and don't live in the idealized statistical world where only the Poisson likelihood exists. Instead, there are a number of

other parameters (nuisance parameters) attached to our background estimation, and these must be 'fit' in the appropriate way simultaneously with the POI [1]

5.3.1 Definition of important parameters

The simplest experiment that takes into consideration of a systematic and a counting error is represented by the likelihood function. By introducing a new measurement of α, which is a unit renormalized parameter describing the one sigma variation of some systematic uncertainty, Δ, with an additional statistical uncertainty represented by γ. By reformulating the effect of this systematic as a unit gaussian with a new degree of freedom, we've "profiled" our likelihood. Ideally, the PDF which represents this uncertainty would be given *a priori*, however a Gaussian shape is a good approximation.

$$L(s, b, \mu, \alpha, \gamma) = Poisson(N|\mu s + \gamma b + \alpha\Delta) \cdot Poisson(N|\gamma b) \cdot Gaussian(0|\alpha, 1). \quad (5.8)$$

The log-likelihood is the constructed by finding the best fit values to maximize this likelihood for the signal and background hypothesis. This maximization procedures amounts to finding a way to account for differences between observed and expected data which has both statistical and systematic uncertainties in terms of these parameters attached to them. As an illustrating example, if there is an approximate 1% excess in a number of bins, and the JES has a 5% correlated uncertainty. During an Asimov fit, the α term should be pulled up to 0.2 to relieve this tension in the likelihood. Alternatively, multiple γ terms could be pulled, however this is more costly to the likelihood.

It's expected that some of these nuisance parameters can be measured and constrained by the fit: with large amount of statistics, the γ terms diminish. Additionally, introduction of new μ terms to describe the background normalization will constrain this uncertainty in the signal regions, and is measured in dedicated control-regions. It is expected that the α terms are to not measured to a large degree. Correlations between these terms can lead to a

[1] This kind of fit is called an Asimov fit. According to physics folklore called following after Isaac Asimov's 1981 short story *A Perfect Fit*. The relevant excerpt might be (though I'm not sure) "I can't get information – I can't be fed – I can't amuse myself – I can't pay for anything, or check on anything, or just plain do anything — without using a computer. And I have been adjusted, as you surely know, so that I am incapable of looking at a computer without hurting my eyes, or touching one without blistering my fingers." [42]

"profiling" of some of these systemics, such is hard to interpret; somehow our fit configuration allowed a better measurement of that systematic than the one produced by the dedicated combined performance group.

In the case of multiple bins, the overall likelihood is the product of each likelihood, $L = L_1 L_2 L_3 ....$ Working with the log-likelihood turns each multiplication into simple addition, so that the minimized quantity is the sum of all Poisson and Gaussian profiles for each parameter separately. The ratio of these (the test-statistic) then turns into subtraction of the best-fit terms.

$$\ln(L) = P_1(\mu, \alpha, \gamma) + P_1(\gamma) + G_1(\alpha) + P_2(\mu, \alpha, \gamma) + P_2(\gamma) + G_2(\alpha) + ... \tag{5.9}$$

This then allows minimization of the heuristic L as a linear superposition of non-linear functions. The `Migrad` strategy is used.

6.0 Results

There are two major formats to show results, one being kinematic plots comparing the MC expectation and the observed data. These results show modeling within these regions with respect to observed data, and provide valuable information as to any excesses or fluctuations as a function of variables sensitive to new physics. Additionally, the use of the HistFitter package [43] is used to perform simultaneous fits to all of the control and signal regions defined in the analysis. HistFitter configures and builds parametric models to describe the observed data, and provides tools to interpret the data in terms of these models. The language and structure of the package is centered on the analysis strategy, and treats the use of control and signal regions in a statistically rigorous way [43]. Specifically, it allows for the automatic construction of a likelihood function that follows the form described in 5.3, but includes all detector, theory, and statistical errors and fits this likelihood function to a set of observed data.

6.1 Distribution of Data in Signal Enhance Regions

The data collected as described in (data collection section) are plotted as a function of various key variables in the signal regions. The error bars on the Monte Carlo simulation and Fake/Non-prompt backgrounds correspond to only the statistical error. Distributions specifically sensitive to the lepton topology of the signal model are sown in Fig. 37, while distributions specifically sensitive to the jet topology of the signal model are shown in Fig. 38.

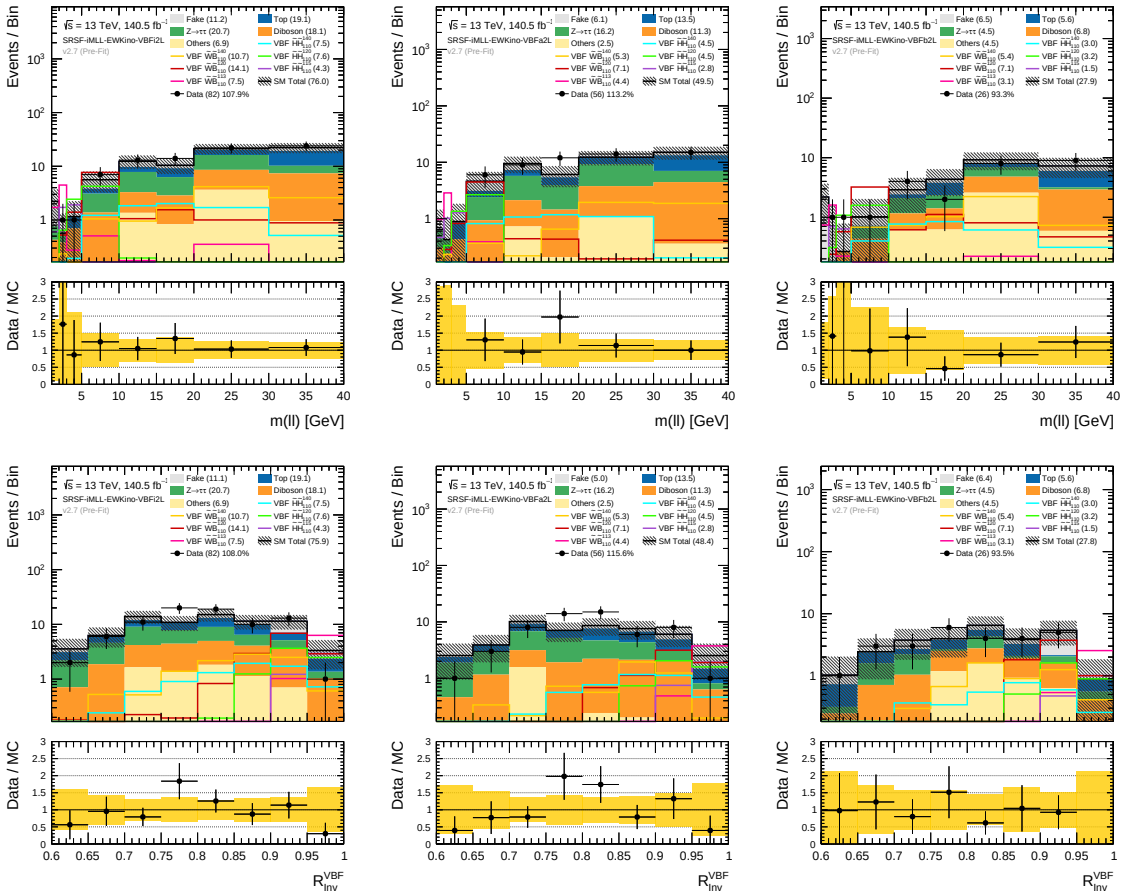

Figure 37: The $m_{\ell\ell}$ and R_{VBF} distribution between data and MC in the inclusive, low, and high bins. Some representative signal models are shown, with $\mu_{sig} = 10$

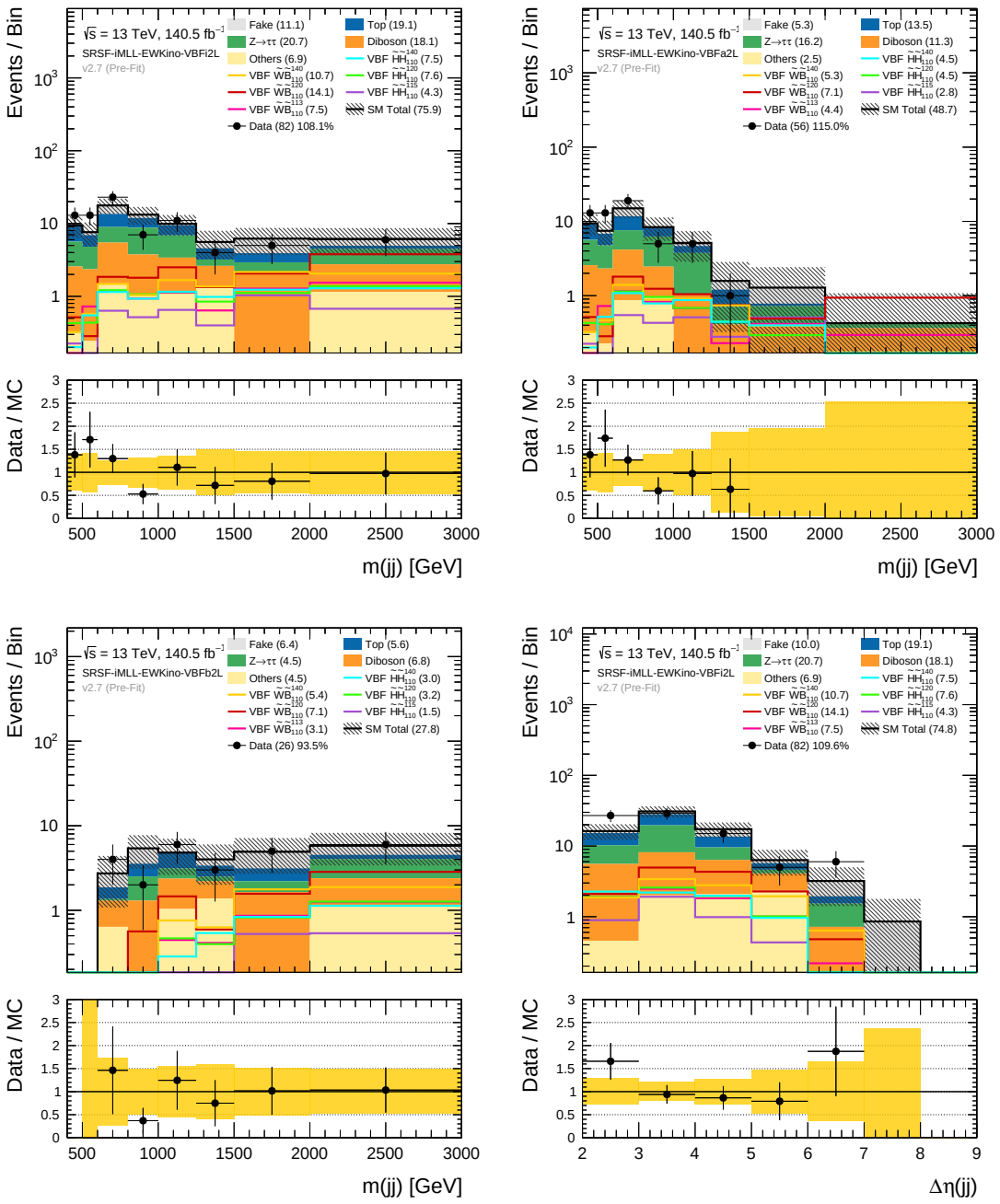

Figure 38: The m_{jj} distribution between data and MC in the inclusive, low, and high bins and for the inclusive bin for $|\Delta\eta(j_1, j_2)|$. Some representative signal models are shown, with $\mu_{sig} = 10$

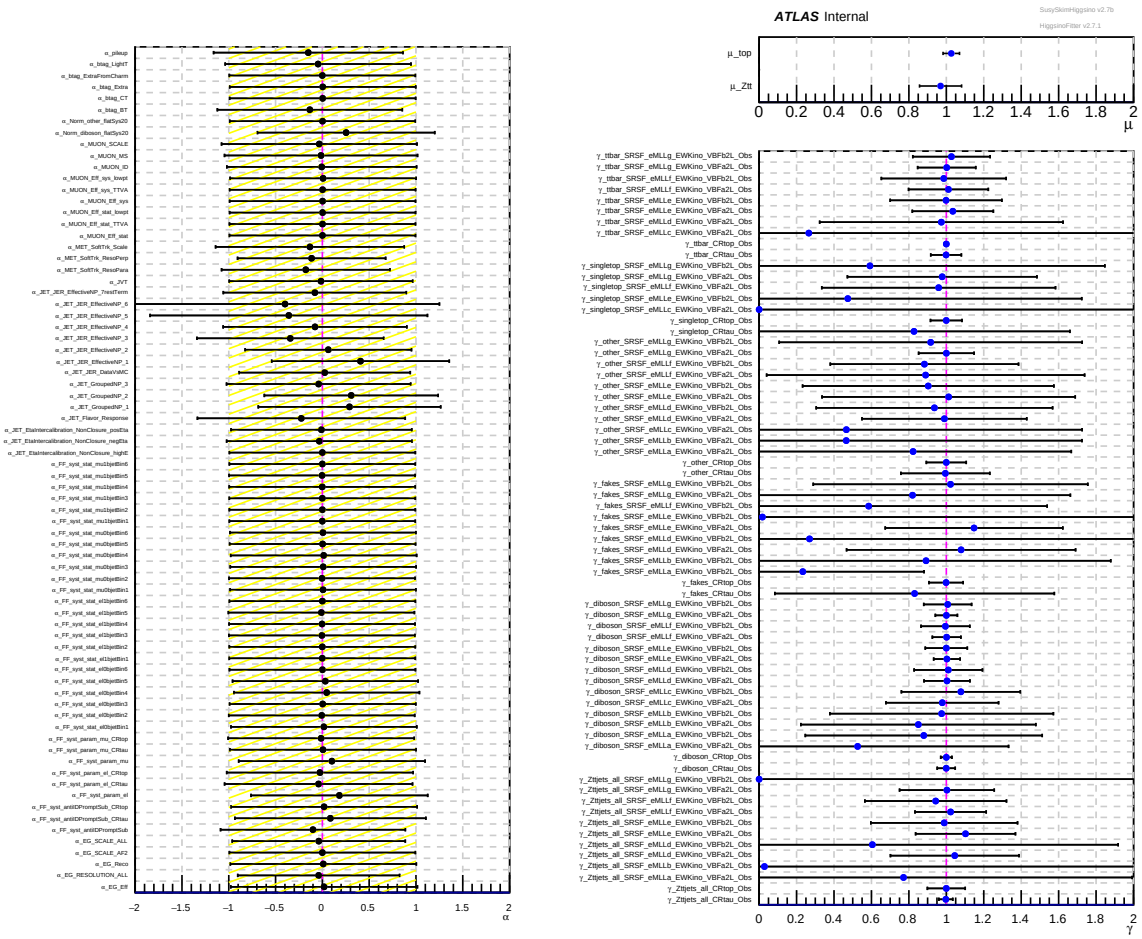

Figure 39: Fit result for all floating parameters in the fit.

6.2 Systematics

There are a large number of uncertainties associated with the background estimation. These variations are included in the profile likelihood fit, and allowed to float about their central or nominal value. The impact of these systematics for each signal region is shown in Tables 8 and 9. These uncertainties fall into three major categories, experimental, fake-factor related, and theoretical. At this point in the analysis, theory uncertainties are not considered. Experimental uncertainties are prescribed by the relevant Combined Performance Groups, which access the impact of modeling detector performance, calibration, and closure of Monte Carlo simulation for each object type. These are listed as follows:

- **Pile-up Reweighting.** An assumption is made on the $\langle\mu\rangle$ profile (distribution of the average number of interactions per bunch crossing) to simulate multiple pile-up interactions in the MC samples used the analysis. This means that the $\langle\mu\rangle$ distribution in MC does not necessarily agree with the one observed in data. Better pile-up description is achieved by re-weighting the MC $\langle\mu\rangle$ distribution to the distribution in data. An uncertainty on this reweighting procedure is considered.
- **Jets.** Uncertainties on the jet energy scale and resolution are considered by means of a strongly reduced configuration defining 6 JES uncertainty components and 8 JER uncertainty components. An additional uncertainty is considered to account for the differences in the efficiency of the JVT selection between data and MC. Similarly, an uncertainty is applied to cover for the differences in the efficiency of the b-tagging identification algorithm between data and simulation.
- **Electrons and Muons.** Uncertainties on the electron energy and muon momentum scale and resolution are considered, as well as uncertainties on the scale factors applied to simulation in order to reproduce the deficiencies measured in data for lepton reconstruction, identification, isolation, and track-to-vertex association.
- **Missing transverse energy.** Uncertainties on the missing transverse energy arise from propagating the uncertainties on the transverse momentum of hard physics objects. Additional uncertainties on the scale and resolution of the track-based soft term are also considered.

- **Luminosity.** An uncertainty of 5% is considered on the the luminosity for 2015+2016+2017+2018 combined datasets.

These sources of systematics from arising from the use of the fake factor method are listed as follows:

- **Statistical uncertainties on the measured fake factors.** These uncertainties arise from the limited sample sizes available from the prescaled single-lepton triggers used to measure the fake-factors. To be conservative, we set the statistical uncertainties on the extrapolated fake factors to be the same as the statistical uncertainties on the fake factors in the lowest p_{T} bin that can be directly measured using the available prescaled single lepton triggers. These statistical uncertainties are then added in quadrature.
- **Prompt subtraction.** The fake factors are measured in a region that is depleted in contributions from true leptons, and are applied in a similarly background-enriched region. When measuring the fake factors, contributions from prompt leptons are subtracted using Monte Carlo. In the signal regions, the impact of these variations is at most on the order of a few percent.
- **Kinematic dependencies.** Measurements of the fake factors as functions of additional variables can indicate the degree to which the measured fake factors are dependent on other kinematic features. The largest variation observed arises from the R_{VBF} dependence. The resulting uncertainty is estimated to be 20% for muons and 40% for electrons, and is applied as a flat systematic across all bins.
- **Non-closure** The tension between the fake lepton estimate and the data in the same-sign validation regions is used as an additional systematic uncertainty. To derive this, the envelope containing the systematic variations is compared with the data in the validation regions. The p_{T} of the subleading lepton is used as the distribution most sensitive to the fake composition.
- **Anti-ID CR Statistics.** The fake contribution is extrapolated from a fake-rich region that includes leptons which fail the signal criteria. The effect of the associated statistical uncertainty of the number of event sin this region is scaled by the average fake-factor and propagated to the SR.

Uncertainty of channel	CR-top-VBF	CR-tau-VBF	SRa [1,2]	SRa [2,3]	SRa [3,5]	SRa [5,10]	SRa [10,20]	SRa [20,30]	SRa [30,40]
Total background expectation	1249.57	233.51	0.40	0.20	0.26	4.88	17.34	12.75	14.94
Total statistical ($\sqrt{N_{\text{exp}}}$)	±35.35	±15.28	±0.63	±0.44	±0.51	±2.21	±4.16	±3.57	±3.87
Total background systematic	±35.34	±15.35	±0.63	±0.61	±0.81	±1.24	±2.70	±2.00	±2.73
Total background systematic (%)	2.83%	6.57%	156.10%	306.98%	313.34%	25.43%	15.57%	15.65%	18.30%
Top Normalisation	±47.77	±0.85	±0.00	±0.00	±0.00	±0.02	±0.15	±0.13	±0.26
Fake factor	±8.85	±0.40	±0.00	±0.00	±0.00	±0.36	±1.26	±0.00	±2.31
Jets	±5.46	±3.56	±0.57	±0.04	±0.14	±0.80	±2.17	±1.55	±1.17
Flavor Tagging	±1.61	±1.55	±0.01	±0.01	±0.00	±0.09	±0.24	±0.23	±0.49
Ztt Normalisation	±1.32	±21.35	±0.01	±0.00	±0.00	±0.20	±0.77	±0.71	±0.32
ETmiss	±0.84	±0.60	±0.13	±0.00	±0.29	±0.01	±0.19	±0.36	±0.32
Electrons	±0.83	±0.84	±0.00	±0.00	±0.01	±0.05	±0.09	±0.01	±0.02
Muons	±0.36	±0.35	±0.01	±0.01	±0.00	±0.04	±0.05	±0.10	±0.16
Pileup	±0.14	±0.19	±0.07	±0.05	±0.01	±0.03	±0.04	±0.02	±0.19
Anti-ID CR Stats	±0.00	±0.00	±0.00	±0.00	±0.00	±0.93	±1.50	±0.00	±1.80
MC Stats	±0.00	±0.00	±0.38	±0.14	±0.73	±0.12	±0.70	±0.96	±0.67

Table 8: Breakdown of systematic uncertainties grouped by type for the VBFa regions after a background-only, CR+SR fit.

Uncertainty of channel	CR-top-VBF	CR-tau-VBF	SRb [1,2]	SRb [2,3]	SRb [3,5]	SRb [5,10]	SRb [10,20]	SRb [20,30]	SRb [30,40]
Total background expectation	1249.57	233.51	0.61	0.69	0.24	0.60	6.06	9.15	7.67
Total statistical ($\sqrt{N_{\text{exp}}}$)	±35.35	±15.28	±0.78	±0.83	±0.49	±0.78	±2.46	±3.02	±2.77
Total background systematic	±35.34	±15.35	±0.93	±0.54	±0.26	±1.06	±3.53	±2.54	±2.94
Total background systematic (%)	2.83%	6.57%	153.21%	77.90%	111.21%	175.61%	[58.23%]	[27.76%]	[38.32%
Top Normalisation	±47.77	±0.85	±0.00	±0.00	±0.00	±0.00	±0.06	±0.04	±0.15
Fake factor	±8.85	±0.40	±0.09	±0.11	±0.00	±0.04	±0.01	±0.87	±0.97
Jets	±5.46	±3.56	±0.14	±0.11	±0.22	±0.09	±0.74	±2.40	±1.01
Flavor Tagging	±1.61	±1.55	±0.00	±0.00	±0.00	±0.01	±0.06	±0.06	±0.27
Ztt Normalisation	±1.32	±21.35	±0.00	±0.00	±0.00	±0.01	±0.27	±0.32	±0.00
ETmiss	±0.84	±0.60	±0.00	±0.01	±0.08	±0.00	±0.21	±0.58	±0.06
Electrons	±0.83	±0.84	±0.00	±0.01	±0.00	±0.02	±0.11	±0.10	±0.04
Muons	±0.36	±0.35	±0.00	±0.00	±0.00	±0.01	±0.17	±0.27	±0.04
Pileup	±0.14	±0.19	±0.00	±0.00	±0.01	±0.01	±0.16	±0.04	±0.01
Anti-ID CR Stats	±0.00	±0.00	±0.94	±0.54	±0.00	±1.09	±3.72	±1.19	±1.07
MC Stats	±0.00	±0.00	±0.09	±0.11	±0.07	±0.09	±0.86	±1.40	±0.60

Table 9: Breakdown of systematic uncertainties grouped by type for the VBFb regions after a background-only, CR+SR fit.

6.3 Model dependent upper Limits

The statistical combination of the likelihood functions for each bin in $m_{\ell\ell}$ and $|\Delta\eta(j_1, j_2)|$ is performed, for a total of 14 statistically orthogonal signals regions and two control regions. The signal regions, by design, constrain the normalization parameter attached to the signal process. By combining multiple bins, the shape information attached to the signal model is implicitly considered in this so-called "shape-fit". If μ_{sig} is not constrained (providing exclusion at the 95% level), μ_{sig} can be scanned to set an upper-limit. The results for the Wino-bino model is shown in Figure 40

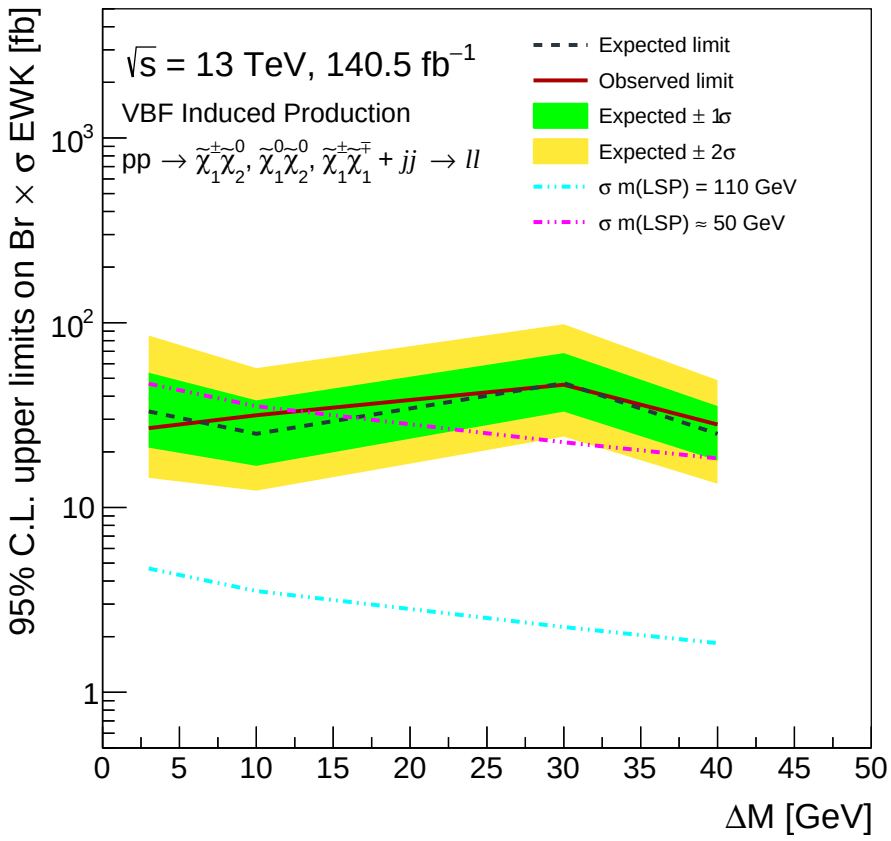

Figure 40: Upper limit on the Wino-Bino interpretation.

6.4 Model independent upper Limits

Given the observed data and SM expectation, it is also possible to set a genetic upper-limit on new physics processes. Model independent 95% CL upper limits are set on visible cross sections $\langle \epsilon\sigma \rangle^{95}_{\text{obs}}$ and expected (observed) signal events $S^{95}_{\text{exp (obs)}}$ of a process with the same final state after selection acceptance and detector efficiency.

A fit with the two control regions and one signal region with inclusive cut criteria is performed. A "Discovery Mode" signal model is used, which places one event in the inclusive bin, attached to a normalization factor (the POI) that is allowed to float. In this case, the 95% CL upper limit on this POI is the number of expected signal events that such a region can exclude. The results from a fit to each individual bin is shown in Table 10.

Signal Region	$\langle\epsilon\sigma\rangle^{95}_{\text{obs}}$ [fb]	S^{95}_{obs}	S^{95}_{exp}	$p(s=0)$ (Z)
SRSF-iMLLa-EWKino-VBFi2L	0.017	2.3	$3.2^{+2.1}_{-1.2}$	0.50
SRSF-iMLLa-EWKino-VBFb2L	0.017	2.3	$3.2^{+2.1}_{-1.1}$	0.50
SRSF-iMLLb-EWKino-VBFi2L	0.025	3.6	$4.4^{+2.4}_{-1.4}$	0.50
SRSF-iMLLb-EWKino-VBFb2L	0.017	2.4	$3.4^{+2.1}_{-1.2}$	0.50
SRSF-iMLLc-EWKino-VBFi2L	0.032	4.6	$4.8^{+2.6}_{-1.6}$	0.50
SRSF-iMLLc-EWKino-VBFb2L	0.017	2.4	$3.4^{+2.2}_{-1.2}$	0.50
SRSF-iMLLd-EWKino-VBFi2L	0.068	9	$9^{+4}_{-2.6}$	0.40
SRSF-iMLLd-EWKino-VBFb2L	0.034	4.8	$6.2^{+3.1}_{-1.8}$	0.50
SRSF-iMLLe-EWKino-VBFi2L	0.14	20	17^{+6}_{-5}	0.23
SRSF-iMLLe-EWKino-VBFb2L	0.052	7	$10^{+4}_{-3.0}$	*nan*
SRSF-iMLLf-EWKino-VBFi2L	0.19	26	21^{+8}_{-6}	0.24
SRSF-iMLLf-EWKino-VBFb2L	0.07	9	14^{+6}_{-4}	*nan*
SRSF-iMLLg-EWKino-VBFi2L	0.24	33	27^{+10}_{-8}	0.26
SRSF-iMLLg-EWKino-VBFb2L	0.09	12	17^{+7}_{-5}	0.50

Table 10: Results from discovery fits. Left to right: 95% CL upper limits on the visible cross section ($\langle\epsilon\sigma\rangle^{95}_{\text{obs}}$) and on the number of signal events (S^{95}_{obs}). The third column $\left(S^{95}_{\text{exp}}\right)$ shows the 95% CL upper limit on the number of signal events, given the expected number (and $\pm1\sigma$ deviations from the expectation) of background events. The last column indicates the discovery p-value ($p(s=0)$). Overall, good agreement between the Standard-Model prediction and observed data is noted, a discovery p-value of 0.5 corresponds to the prior of 0.5 for the alternative hypothesis (some new physics), which is not affected by the observed conditionals.

7.0 Discussion and Conclusion

The kinematic results of the important variables, $m_{\ell\ell}$, m_{jj}, R_{VBF}, and $|\Delta\eta(j_1, j_2)|$ show no excesses above the standard model expectation. These are important variables for not only this type of model, but other models like it. The performance of the ATLAS detector has been demonstrated for jets in the forward regions, and events which exhibit this unique signal saved and analyzed. This analysis is limited by low signal yields for the expected model, and this could be recified by exploring the single lepton channel, or a single tau channel with a democratic stau (the tau superpartner) mediating the neutralino decay.

A variety new questions had to be asked during the course of this analysis. The signal generation required careful treatment. It was found that the sub-leading jet will be harder, and provided a good handle to eliminate QCD-like backgrounds. The m_{jj} distribution is moderate and the $|\Delta\eta(j_1, j_2)|$ distribution not as striking (due to the t-channel character of the process), but binning in this variable (a an essential coarse-grained fit to the VBF angular variables, a new technique gaining recognition, see [44]) showed marked improvement. The RJR model was extended to the VBF-like topology to profit off the compressed signal at high m_{jj}, with good results. The fake-factor method was shown to be versatile enough to handle the hard-jet kinematics required within these regions.

There may be EFT approaches, other models, or some combination of "VBF-friendly" models which predict really soft leptons. None-the-less, this type of search will be expanded to Higgs-portal-like models in the future, to see what gains we may be able to realistically extract. This analysis also opens the doors for further VBF searches which will require similar techniques, as all of the featured studies work on the high m_{jj} tail. There is also a rich phenomenology of Higgs-portal like models, which can profit off of the well studied properties of the SM-like Higgs boson in the VBF channel. Heavy new particles, such as new Higges or bulk gravitons also have a VBF prediction while also having challenging final states. Overall, these results serve not only as an aggressive search for VBF SUSY, but as a strong baseline for future analysis of this type. No new physics were discovered this time, but perhaps the next.

Bibliography

[1] Cinzia De Melis. The CERN accelerator complex. Complexe des accélérateurs du CERN. Jan 2016. General Photo.

[2] John Paul Archambault and et.al. Artem Artamonov. Performance of the atlas liquid argon forward calorimeter in beam tests. 2013.

[3] Robert Orr. Atlas liquid argon hadronic calorimeters. 07 2004.

[4] Georges Aad et al. Observation of a new particle in the search for the Standard Model Higgs boson with the ATLAS detector at the LHC. *Phys. Lett.*, B716:1–29, 2012.

[5] Serguei Chatrchyan et al. Observation of a new boson at a mass of 125 GeV with the CMS experiment at the LHC. *Phys. Lett.*, B716:30–61, 2012.

[6] DAMPE Collaboration, G. Ambrosi, Q. An, and Asfandiyarov. Direct detection of a break in the teraelectronvolt cosmic-ray spectrum of electrons and positrons. *Nature*, 552:63 EP –, 11 2017.

[7] E. Aprile et al. The XENON1T Dark Matter Experiment. *Eur. Phys. J.*, C77(12):881, 2017.

[8] Peter W. Higgs. Broken symmetries and the masses of gauge bosons. *Phys. Rev. Lett.*, 13:508–509, Oct 1964.

[9] Stephen P. Martin. A Supersymmetry primer. pages 1–98, 1997. [Adv. Ser. Direct. High Energy Phys.18,1(1998)].

[10] Lyndon Evans and Philip Bryant. LHC machine. *Journal of Instrumentation*, 3(08):S08001–S08001, aug 2008.

[11] Oliver S. Bruning. LHC challenges and upgrade options. *J. Phys. Conf. Ser.*, 110:112002, 2008.

[12] G. Aad et al. The ATLAS Experiment at the CERN Large Hadron Collider. *JINST*, 3:S08003, 2008.

[13] ATLAS Collaboration. Luminositypublicresultsrun2. https://twiki.cern.ch/twiki/bin/view/AtlasPublic/LuminosityPublicResultsRun2. Accessed: 2019-03-25.

[14] Performance of the ATLAS Inner Detector Track and Vertex Reconstruction in the High Pile-Up LHC Environment. 2012.

[15] C Adloff et. al. The time structure of hadronic showers in highly granular calorimeters with tungsten and steel absorbers. *Journal of Instrumentation*, 9(07):P07022–P07022, jul 2014.

[16] ATLAS Collaboration. *ATLAS muon spectrometer: Technical Design Report*. Technical Design Report ATLAS. CERN, Geneva, 1997.

[17] K. Nakamura et al. PASSAGE OF PARTICLES THROUGH MATTER. 2010.

[18] Georges Aad et al. Muon reconstruction performance of the ATLAS detector in proton–proton collision data at $\sqrt{s}$ =13 TeV. *Eur. Phys. J.*, C76(5):292, 2016.

[19] M. Abolins et al. The ATLAS Data Acquisition and High Level Trigger system. *JINST*, 11(06):P06008, 2016.

[20] James Catmore, Jack Cranshaw, Thomas Gillam, Eirik Gramstad, Paul Laycock, Nurcan Ozturk, and Graeme Andrew Stewart. A new petabyte-scale data derivation framework for ATLAS. *J. Phys. Conf. Ser.*, 664(7):072007, 2015.

[21] Jovan Mitrevski. Preparing ATLAS reconstruction software for LHC's Run 2. *J. Phys. Conf. Ser.*, 664(7):072034, 2015.

[22] A. Buckley, T. Eifert, M. Elsing, D. Gillberg, K. Koeneke, A. Krasznahorkay, E. Moyse, M. Nowak, S. Snyder, and P. van Gemmeren. Implementation of the ATLAS Run 2 event data model. *J. Phys. Conf. Ser.*, 664(7):072045, 2015.

[23] Morad Aaboud et al. Search for squarks and gluinos in final states with jets and missing transverse momentum using 36 fb^{-1} of $\sqrt{s} = 13$ TeV pp collision data with the ATLAS detector. *Phys. Rev.*, D97(11):112001, 2018.

[24] Michael Hance, Joana Machado Miguens, et al. Searches for Weak Production of Compressed Supersymmetry in *pp* Collisions at $\sqrt{s} = 13$ TeV with the ATLAS Detector. Technical Report ATL-COM-PHYS-2016-1708, CERN, Geneva, Nov 2016.

[25] Jinrui Huang, Tao Liu, Lian-Tao Wang, and Felix Yu. Supersymmetric Exotic Decays of the 125 GeV Higgs Boson. *Phys. Rev. Lett.*, 112(22):221803, 2014.

[26] Alejandra Melfo, Miha Nemevsek, Fabrizio Nesti, Goran Senjanovic, and Yue Zhang. Type II Seesaw at LHC: The Roadmap. *Phys. Rev.*, D85:055018, 2012.

[27] Andrés Flórez, Alfredo Gurrola, Will Johns, Jessica Maruri, Paul Sheldon, Kuver Sinha, and Savanna Rae Starko. Anapole Dark Matter via Vector Boson Fusion Processes at the LHC. 2019.

[28] Johan Alwall, Michel Herquet, Fabio Maltoni, Olivier Mattelaer, and Tim Stelzer. MadGraph 5 : Going Beyond. *JHEP*, 06:128, 2011.

[29] Morad Aaboud et al. Electron reconstruction and identification in the ATLAS experiment using the 2015 and 2016 LHC proton-proton collision data at $\sqrt{s} = 13$ TeV. *Submitted to: Eur. Phys. J.*, 2019.

[30] Zhenyu Han, Graham D. Kribs, Adam Martin, and Arjun Menon. Hunting quasidegenerate Higgsinos. *Phys. Rev. D*, 89(7):075007, 2014.

[31] Howard Baer, Azar Mustafayev, and Xerxes Tata. Monojet plus soft dilepton signal from light higgsino pair production at LHC14. *Phys. Rev. D*, 90(11):115007, 2014.

[32] Alan Barr and James Scoville. A boost for the EW SUSY hunt: monojet-like search for compressed sleptons at LHC14 with 100 fb^{-1}. *JHEP*, 04:147, 2015.

[33] Search for new physics in the compressed mass spectra scenario using events with two soft opposite-sign leptons and missing momentum energy at 13 TeV. Technical Report CMS-PAS-SUS-16-025, CERN, Geneva, 2016.

[34] Paul Jackson and Christopher Rogan. Recursive Jigsaw Reconstruction: HEP event analysis in the presence of kinematic and combinatoric ambiguities. *Phys. Rev.*, D96(11):112007, 2017.

[35] Andreas Hocker et al. TMVA - Toolkit for Multivariate Data Analysis. 2007.

[36] Albert M Sirunyan et al. Measurement of the differential cross sections for the associated production of a W boson and jets in proton-proton collisions at $\sqrt{s} = 13$ TeV. *Phys. Rev.*, D96(7):072005, 2017.

[37] G. Aad et al. Expected Performance of the ATLAS Experiment - Detector, Trigger and Physics. 2009.

[38] Georges Aad et al. Measurements of the electron and muon inclusive cross-sections in proton-proton collisions at $\sqrt{s} = 7$ TeV with the ATLAS detector. *Phys. Lett.*, B707:438–458, 2012.

[39] Extraction of the prompt muon component in inclusive muons produced at $\sqrt{s} = 7$ TeV. 2010.

[40] Kurt Brendlinger, Joseph Reichert, Keisuke Yoshihara, Otilia Anamaria Ducu, Julien Maurer, Othmane Rifki, Christian Ohm, Martin Tripiana, Claudia Merlassino, and Yu-Ting Shen. Overview of the methods used to estimate the fake lepton background in

the SUSY group. Technical Report ATL-COM-PHYS-2017-469, CERN, Geneva, May 2017.

[41] Glen Cowan, Kyle Cranmer, Eilam Gross, and Ofer Vitells. Asymptotic formulae for likelihood-based tests of new physics. *Eur. Phys. J.*, C71:1554, 2011. [Erratum: Eur. Phys. J.C73,2501(2013)].

[42] Isaac Asimov and Don Dixon. *The winds of change–and other stories*. Ballantine Books, 1984.

[43] M. Baak, G. J. Besjes, D. Côte, A. Koutsman, J. Lorenz, and D. Short. HistFitter software framework for statistical data analysis. *Eur. Phys. J.*, C75:153, 2015.

[44] Ulrich Haisch and Giacomo Polesello. Searching for dark matter in final states with two jets and missing transverse energy. *JHEP*, 02:128, 2019.